Modelling Polarisation of Materials with Applications in Self-Assembly

Connor Williamson

Student Number: 14276386

Thesis submitted to the University of Nottingham
for the degree of Doctor of Philosophy

Supervised by Prof. Elena Besley

School of Chemistry
University of Nottingham

September 2024

Abstract

Theoretical descriptions of charged induced polarisation and dispersion forces between materials are investigated, extended or applied to study a range of natural and novel environments. Initially, a mathematical framework is established to describe many-body interactions between charged dielectric particles. This framework is then extended to include the effects of inhomogeneous surface charge distributions and externally applied electric fields. This extension is rigorously tested against classical results and then further justified for N particles by considering a novel experimentally realised system.

The framework is then applied to study the effect of surface charge density and polarisation on the interactions between like-charged particles in noctilucent clouds. Like-charge attraction is shown to promote nucleation of such particles given the possible velocities at the temperature of these environments. Volcanic ash is then investigated in a similar context at the various temperatures it would experience throughout an eruption. Aggregation of volcanic ash due to non-thermal perturbation is also investigated by considering the collisional cross sections of the clouds constituents via particle dynamics. Particle dynamics is then utilised to study the aggregation driven inefficiencies of dry powder inhalers, suggesting a possible method to alleviate this.

The electronic interaction of neutral materials at close separation is then investigated in the context of the Casimir force. After an initial bench-marking of a convenient mathematical formalism, new systems in which quantum levitation can be realised are predicted via consideration of the Casimir equilibrium.

Acknowledgements

List of Publications

1. J. Baptiste, C. Williamson, J. Fox, A. J. Stace, M. Hassan, S. Braun, B. Stamm, I. Mann, and E. Besley, "The influence of surface charge on the coalescence of ice and dust particles in the mesosphere and lower thermosphere," Atmospheric Chemistry and Physics, vol. 21, no. 11, pp. 8735–8745, 2021. [Online].
Available: https://acp.copernicus.org/articles/21/8735/2021

2. M. Hassan, C. Williamson, J. Baptiste, S. Braun, A.J. Stace, E.Besley and B. Stamm, "General electrostatic many-body framework: Manipulating interactions between dielectric particles with electric fields: A general electrostatic many-body framework", Journal of Chemical Theory and Computation, vol. 18, pp. 6281–6296, 2022.

3. C. Williamson and E. Besley, "Investigating the manipulation of equilibrium casimir forces through variation in composition, structure and medium", *in submission*

4. C.Williamson, J. Baptiste, C. Pang, M. Hamilton, D. Prime, A.J. Stace and E. Besley, "Charged particle dynamics in dry powder inhalers", *in submission to GSK IP department*

5. C. Williamson, C. Reeve, C.M. Kardeşler, A.J. Stace and E. Besley, "Dynamic investigation of like-charged attraction in volcanic ash", *in preparation*

Contents

List of Tables

List of Figures

Chapter 1

Introduction

Of the four fundamental forces in nature, (electromagnetic, gravitational, strong, weak) the electromagnetic force was understood in its entirety first, with James Clark Maxwell defining the electromagnetic interaction conclusively in 1862. [1–4] As Maxwell's equations define all electromagnetic interactions, only two of his four equations are required to describe the electro *static* interaction of charged particles interacting through the electric field. Whilst other phenomena could occur as a consequence of electrostatic interactions, the treatment of which could require other examples of Maxwell's equations to describe, in this work only the electrostatic interaction will often be considered.[1]

Two-hundred and thirty-eight years prior to this work, Coulomb first published [5] his name-bearing law stating that the force acting between two infinitesimally small charged particles (point charges) is proportional to the product of their charges $(q_1 q_2)$, and inversely proportional to the square of their separation (r), such that

$$F = \frac{q_1 q_2}{4\pi\epsilon_0 r^2} \tag{1.1}$$

where the prefactors $1/4\pi\epsilon_0$ are often substituted as K such that $K = 8.987551792 \times 10^9$ N m^2 C^{-2}, as $\epsilon_0 = 8.85418782$ C^2 s^2/kg m^3. The $1/4\pi$ presents itself in

---

[1]polarisation due to the presence of external fields and the interaction of charged particles will only consider Gauss's law, whilst dispersion forces require a more general approach.

Coulomb's law due to the radial nature of the electric field emanating from a point charge, whilst ϵ_0 is the permittivity of free space and defines the strength of all electromagnetic interactions in the universe; the permittivity of free space can be understood to control or scale the response of the electric field given a charge density at any point in space. Coulomb's law also predicts whether two point charges will attract or repel, stating that if two charges are of the same sign they will repel (undergo a positive force), whereas if they are of opposite charge they will attract (undergo a negative force). [6, 7]

Equation 1.1 can be written in a more formal mathematical setting such that F is a vector ($\mathbf{F}_1$) of the force acting on a particle (particle 1) due to the presence of another particle (particle 2); each particle is a point charge with charges q_1 and q_2 respectively. At some separation of particles 1 and 2 ($\mathbf{r}_{12}$), where $\mathbf{r}_{12} = \mathbf{r}_1 - \mathbf{r}_2$, the Coulomb's force acting on each i'th particle ($\mathbf{F}_i$) can be written as

$$\mathbf{F}_1 = \frac{q_1 q_2}{4\pi\epsilon_0} \frac{\hat{\mathbf{r}}_{12}}{|\mathbf{r}_{12}|^2}, \quad \mathbf{F}_2 = \frac{q_1 q_2}{4\pi\epsilon_0} \frac{\hat{\mathbf{r}}_{21}}{|\mathbf{r}_{21}|^2} = -\mathbf{F}_1 \qquad (1.2)$$

where $\hat{\mathbf{r}}_{12}$ is the unit vector defining the distance from charge 1 to charge 2, and similarly for $\hat{\mathbf{r}}_{21}$ which occasionally may appear as r such that $|\mathbf{r}_{12}| = |\mathbf{r}_{21}| = r$. Equation 1.2 can be seen to satisfy Newton's third law of motion such that each particle undergoes a force of the same magnitude but of opposing direction to the particle causing the force.

The interaction of the two point charges is through the electric field, such that they act as either a source ($q_i > 0$) or a sink ($q_i < 0$) of electric field lines, the order of which is historic and not of scientific implication.[7] When considering the electric field within a finite space, Gauss's law can be applied to determine the nature of the field through a closed surface. As derived by Lagrange [8], Gauss's law [9, 10] states that the flux of the electric field through an arbitrary closed surface is proportional to the electric charge enclosed by the surface, irrespective of how that charge is distributed. Mathematically,

this is stated as

$$\oiint_S \mathbf{E} \cdot d\mathbf{A} = \frac{1}{\epsilon_0} \iiint_V \rho \, dV \tag{1.3}$$

where ρ is the density of charges contained within a volume V of surface area $\mathbf{A}$, enclosed by the surface S through which there is a flux of the electric field $\mathbf{E}$. In the case of a point charge, the integral on the right-hand side (RHS) of equation 1.3 can be evaluated as the charge of the point charge (q), which for simplicity is defined as being at the centre of the spherically symmetric S, of radius r such that the field is uniform on the surface. In this case, it can be seen that as $\mathbf{E}$ and $\mathbf{A}$ are always parallel,

$$\oiint_S \mathbf{E} \cdot d\mathbf{A} = E \, 4\pi r^2 = \frac{q}{\epsilon_0} \implies E = \frac{q}{4\pi\epsilon_0 r^2} \tag{1.4}$$

where $E\hat{\mathbf{r}} = \mathbf{E}$ and $\hat{\mathbf{r}}$ is the unit vector of the radius. This is true in the case when E is uniform across the surface, such as when a point charge is in the centre of the volume, as can often be chosen for ease. Given the Lorentz equation[6, 7, 11]

$$\mathbf{F} = q(\mathbf{E} + \mathbf{v} \times \mathbf{B}) \tag{1.5}$$

in the absence of any magnetic field $\mathbf{B}$, and assuming $\mathbf{0}$ velocity ($\mathbf{v}$), it can be seen that Coulomb's law is reproduced given the electric field derived in equation 1.4.

Coulomb's law holds true not only in the case of two point charges interacting but also in the case of many point charges interacting. The evaluation of a force acting on a particle i due to the presence of M other particles, can be achieved by applying the principle of superposition (such that the sum of the individual actions is equal to the overall action) [6] to either Coulomb's force law (equation 1.2),

$$\mathbf{F}_i = \frac{1}{4\pi\epsilon_0} \sum_{j \neq i}^{M} \frac{q_i q_j}{|\mathbf{r}_{ij}|^2} \hat{\mathbf{r}}_{ij}, \tag{1.6}$$

or via the summation of the electric field each point charge in the system produces at the location of particle i, but not including particle i, where one can use equations 1.4 and 1.5 with the principle of superposition to show that if

$$\mathbf{E}(\mathbf{r}_i) = \frac{1}{4\pi\epsilon_0} \sum_{j \neq i}^{M} \frac{q_j}{|\mathbf{r}_{ij}|^2} \implies \mathbf{F}_i = \frac{q_i}{4\pi\epsilon_0} \sum_{j \neq i}^{M} \frac{q_j}{|\mathbf{r}_{ij}|^2} \hat{\mathbf{r}}_{ij} \tag{1.7}$$

Particle i is excluded in both cases as a particle does not undergo a force due to the presence of itself in the absence of external perturbation.

As a point charge would undergo a force due to its position within an electric field, the conservation of energy states that at that point in space there exists some potential energy associated with the point charge which it then loses (an amount of) upon undergoing the force. To this end, we define a scalar field $\phi(\mathbf{r}, t)$ as the electric potential, such that

$$\mathbf{E} = -\nabla\phi, \tag{1.8}$$

which is a function only of its position in space for the purpose of this work. This is also consistent with the Maxwell-Faraday [6, 7, 12] equation of Maxwell's equations, such that

$$\nabla \times \mathbf{E} + \frac{d\mathbf{B}}{dt} = 0 \tag{1.9}$$

which in the absence of a time dependent magnetic field (as assumed throughout the electrostatics discussion) becomes $\nabla \times (-\nabla\phi)$ which is zero if ϕ is *any* continuously twice differentiable function such that $\phi \in \mathbb{C}(\mathbb{R}^3)$. In the case of a point charge, given equation 1.4 and 1.8, it can be seen the electric potential due to a point charge q can be evaluated as

$$\phi = -\int_C \mathbf{E} \cdot d\mathbf{r}_i = -\frac{q}{4\pi\epsilon_0} \int_C \frac{1}{r^2} dr = \frac{q}{4\pi\epsilon_0 r} \qquad (1.10)$$

where r is the defined as the distance from the point charge. Physically, in the case of a point charge q, ϕ can be interpreted as the amount of work required to bring that point charge from infinity (where no such forces are present) to its current position, and also what can be released without a restoring force present.

1.1   Polarisation

Finite sized (charged) particles, considered as enclosed boundaries of a finite volume, in the absence of an electric field, may possess a different surface charge upon the introduction of an electric field, unlike the point charge, which emanates the same electric field, regardless of external perturbation. Given such a particle in an external electric field, the charges inside the boundary may re-orientate or redistribute to a new equilibrium configuration relative to the external field but constrained by either the boundary of the particle or the molecular forces bounding the molecules within the material.

Upon the application of an electrical field, there exist two types of materials at any given temperature: conductors and insulators (also known as dielectrics). If the internal charges of the material inside the boundary undergo translational motion in the direction of the field such that a current is produced, the material is a conductor. If no current is produced upon application of an electric field then the material is considered a dielectric.

Although no current is produced via the application of an electric field to a dielectric, the internal charges can still re-orientate themselves relative to the applied field. This can be broken down into four main types of redistribution: electronic, orientational, ionic and interfacial, which are illustrated in figure 1.1a, b, c and d, respectively. Electronic polarisation occurs when a positive
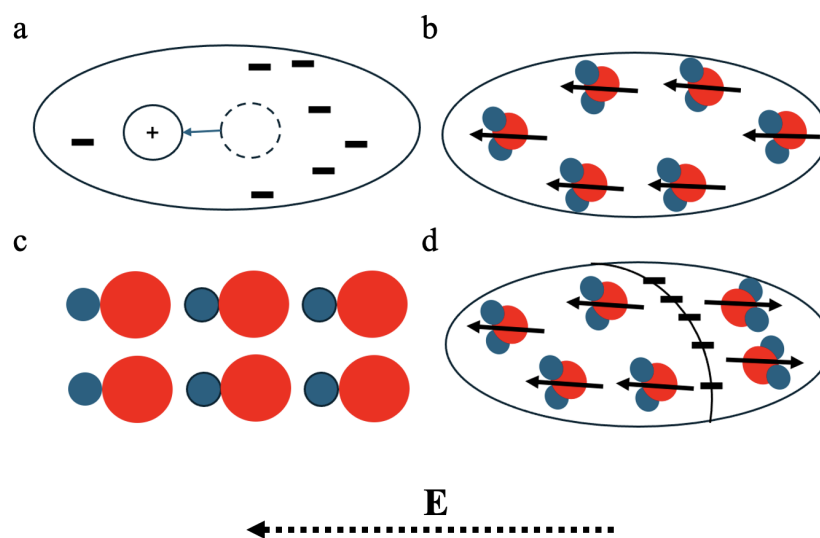
Figure 1.1: *Illustrations of different mechanisms of polarisation in a dielectric caused by the interaction with an external electric field, of a direction as shown by the dotted arrow; electronic polarisation (a), orientational polarisation (b), ionic polarisation (c) and interface polarisation (d). The blue particles represent the negative substituent, where as the red represents the positive substituent.*

atomic nucleus moves in the direction of an applied electric field, but in the opposite direction to the negative electron cloud usually surrounding it, similar to that of ionic polarisation in which positive and negative crystal constituents move in opposing directions to cause a different separation, and hence altering its surface charge distribution. Orientational polarisation occurs when molecular multipoles (often assumed to be dipoles) rotate to align with the electric field but do not undergo translation motion, and interfacial polarisation occurs due to the presence of a boundary within a material.

Such reorientation of multiple charges within a material causes the outside of the particle to appear charged with regard to the electric field they produce. The charge that appears to reside on the surface under such conditions is known as the bound charge due to its origin. This effect is illustrated in figure 1.1 such that the systems illustrated in a, b and c will adopt a dipolar surface charge in the presence of an electrical field, whereas system d, a particle composed of two different dielectric materials with an interface between them, would appear as mostly negatively charged due to opposing reorientations with the field either side of the boundary. This effect is illustrated in full for the case of electronic
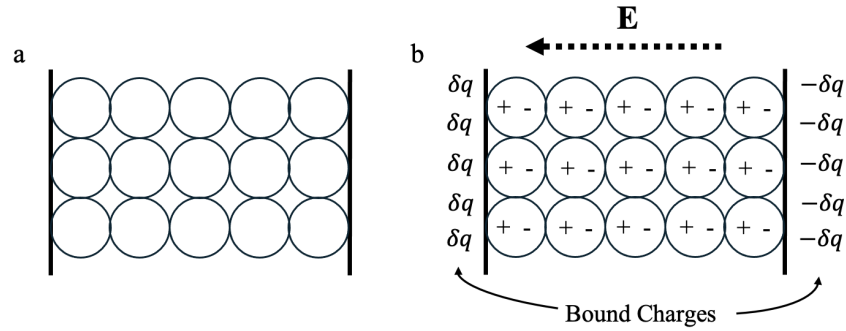
Figure 1.2: *An illustration of an otherwise neutral material (a), gaining a surface charge, of elements ∂q, due to the electronic polarisation occurring inside the dielectric material due to an electric field in the direction defined by the arrow $\boldsymbol{E}$ (b).*

polarisation in figure 1.2.

As the charges within finite-sized dielectric particles are locally constrained, the resultant surface charge of each particle in the system must be determined in the presence of an external perturbation in order to calculate the force acting on each particle in the system. Physically, the redistribution of the charge is instantaneous in comparison to the movement of physical boundaries or the applied electric field, which is an assumption made throughout this work[2].

The ability of an atom to gain a dipole, as illustrated in figure 1.1a and figure 1.2 is dependent on the polarisability, α, of the atom. The polarisability of an isotropic medium can be defined as the tendency of a charge density to be distorted from its natural shape due to the presence of an electric field and is further defined by the relationship between the dipole moment per unit volume, $\mathbf{P}$, induced by an electric field $\mathbf{E}$ as

$$\mathbf{P} = \alpha \mathbf{E} \tag{1.11}$$

where $\mathbf{P}$ is the vector describing the dipole moment for a given unit volume in a material.

As discussed earlier, the permittivity of free space controls the response of the electric field due to a charge, and as such one can write equation 1.11 as

---

[2]To remove the effects of a potential delay in the polarisation of two closely interacting particles moving past one another at some velocity.

$$\mathbf{P} = \epsilon_0 \chi_e \mathbf{E} \qquad (1.12)$$

where χ_e is the electric susceptibility of a given material. χ_e is a dimensionless quantity that acts as a constant of proportionality to indicate the degree of change between dipolar density per unit volume of a material given a permittivity of free space (a vacuum). More commonly, this is expressed in terms of the dielectric constant, κ, of the particle which is defined as

$$\kappa = \chi_e + 1. \qquad (1.13)$$

The dielectric constant of a material is inherently a bulk property that is defined as the ratio of the electric permittivity inside a material and the permittivity of free space (ϵ/ϵ_0). The field of a particle of a given free charge density (so that the particle is charged) can be described by the dielectric displacement vector $\mathbf{D}$ defined as

$$\mathbf{D} = \epsilon_0 \mathbf{E} + \mathbf{P} \qquad (1.14)$$

thus Gauss's law states in each case

$$\nabla \cdot \mathbf{E} = \frac{\rho}{\epsilon_0}, \ \nabla \cdot \mathbf{P} = -\rho_b, \ \nabla \cdot \mathbf{D} = \rho_f \qquad (1.15)$$

and given equation 1.12 the dielectric displacement field can also be defined as

$$\mathbf{D} = \epsilon_0 \mathbf{E} + \mathbf{P} = \epsilon_0(1 + \chi_e)\mathbf{E} = \epsilon_0 \kappa \mathbf{E} \qquad (1.16)$$

where ρ_f is the free charge density describing the formal charge of the particle, and ρ_b is the bound charge describing the polarisation of the material due to external perturbation. The dielectric displacement field lines always begin and end at the particle's surface, and only exist for a charged particle given equation 1.15.

1.2 Interacting Particles

Now that a formalism is in place to describe the effects an electric field has on a particle, one can begin to evaluate the effect one charged particle will have on another particle, plane or general dielectric object. Two methods are available to us to describe such interactions: image charges and multipolar expansions. The former will be considered initially in the following subsection whilst the latter will follow and describe the use of associated Legendre polynomials to describe the surface charge, which will prove essential to the entirety of the following works.

It is clear from equation 1.15, and the Lorentz equation, there is a distinct relationship between the force a polarised particle undergoes in an electric field and the volume charge density ρ that includes the effects of polarisation, ρ_b. Utilising Gauss's law once again, as in equation 1.15, it can be seen that if $\phi(\mathbf{r})$ is known, it is possible to calculate the force on a particle in the system. This follows as

$$\mathbf{E} = -\nabla\phi, \ \frac{\rho}{\epsilon_0} = \nabla \cdot \mathbf{E} = \nabla \cdot (-\nabla\phi) = -\nabla^2\phi \tag{1.17}$$

showing that charge density is a solution to the Poisson equation of the form

$$-\nabla^2\phi = \frac{\rho}{\epsilon_0} \tag{1.18}$$

It then follows that the potential at the boundary of two materials must be known to calculate the charge density. As both the bound and free charges reside on the surface of particles, the two-dimensional form is often favoured, which is of the form

$$-\nabla^2\phi = \frac{\sigma}{\epsilon_0} \tag{1.19}$$

where σ is the surface charge density. Whilst there exists an infinite number of solutions to the Poisson equation, if the boundary of two materials follows a set

of boundary conditions defining the potential on the surface of the boundary, S, then a unique solution should exist.

1.2.1   Image Charges: The Interactions of Boundaries with Charge

An image charge is a non-physical mathematical tool to evaluate the effect a charged particle in a medium has on a nearby planar boundary between two materials from within one of the media. This particular method, proposed by Lord Kelvin [13], is used to describe systems of point charges above infinite, smooth boundaries of materials.

It is clear from equations 1.18 and 1.19 that boundary conditions for ϕ are required to find the unique solution describing the interaction of a boundary with an electric field. To this end, one can employ physical boundary conditions dependent on the system being studied.[14]
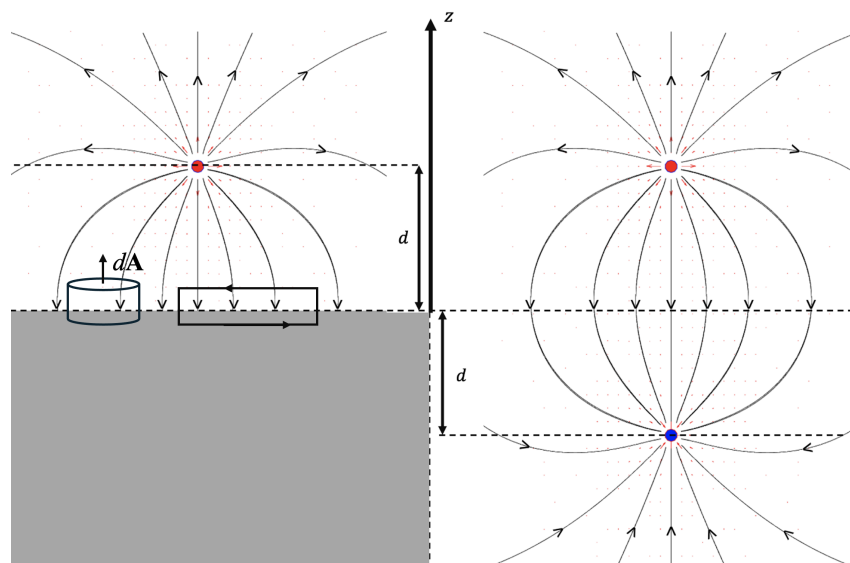
Figure 1.3: *An illustration of a point charge above a conducting surface with electric field lines emanating from the point charge and terminating at: the conducting surface (left), the image charge (right). The vectors utilised in integration's throughout this chapter are illustrated on the boundary between the plane and the conductor.*

Consider the case of a point charge above ($z\,0$) a grounded, perfectly conducting material, as illustrated in figure 1.3 such that, the z-direction is defined as perpendicular to the plane, and the point charge has coordinates $\mathbf{r}_1 = (0, 0, d)$,

where d is the plane-particle separation. The known behaviour of the conductor and the point charge can be applied to provide the following boundary conditions

- $z = 0 : \phi = 0$ as the conductor is assumed to be in electrostatic equilibrium

- $\phi \to 0$ with the distance from the point charge (source/sink)

It is clear that for the potential to be 0 at the boundary of a vacuum and a grounded conductor, and for ϕ to be continuous yet emanating from a point charge, a charge of the opposite sign placed equidistant from the surface in the opposing z-direction such that $\mathbf{r}_2 = (0, 0, -d)$ is a solution as this would act as the sink to the field emanating from a positive point charge (or converging on in the case of a negative charge).[6, 14] The non-real (unphysical) charge used to describe such an interaction is an image charge. Therefore, the potential of the system can be written as

$$\phi(\mathbf{r}_0) = \frac{1}{4\pi\epsilon_0} \left(\frac{q}{|\mathbf{r}_0 - \mathbf{r}_1|} - \frac{q}{|\mathbf{r}_0 - \mathbf{r}_2|} \right) \tag{1.20}$$

which can also be seen to satisfy the condition that the potential due to the point charge tends to 0 as d ($= (1/2)|\mathbf{r}_{21}|$) tends to infinity. Furthermore, the potential can take the more explicit form

$$\phi(\mathbf{r}_0) = \frac{1}{4\pi\epsilon_0} \left(\frac{q}{(x^2 + y^2 + d^2)^{1/2}} - \frac{q}{(x^2 + y^2 - d^2)^{1/2}} \right) \tag{1.21}$$

from which it follows that the surface charge distribution of the grounded conducting plane, due to the internal nature of the metals, can be evaluated as

$$\sigma(x, y) = -\frac{qd}{2\pi(x^2 + y^2 + d^2)^{3/2}} \tag{1.22}$$

by considering the first derivative of equation 1.21 in the (x, y) direction.

Due to the negative sign in equation 1.22, it can be seen that a grounded conductor will always attract a point charge. It is worth noting that the image charge method enables one to study the electric field and surface charge distributions of planar environments; it is not a physical representation as it assumes a constant medium, and no such image charges exists. [14]

When describing dielectric media, a similar method can be applied to find a solution to the Laplace equation. However, due to the difference in the physical nature of the interaction between a dielectric and a conductor, the boundary conditions change. The electric field inside a dielectric is altered by the presence of the dipoles with in it such that the potential is different either side of the boundary

$$\phi = \begin{cases} \phi_1(\mathbf{r}), & z > 0 \\ \phi_2(\mathbf{r}), & z < 0 \end{cases} \tag{1.23}$$

Like in the case of a conductor, and assuming the exact same physical set up only with a dielectric in place of a conductor, in the case of $z > 0$ we can model the potential as two point charges - one is the actual charge q whilst the other is the image charge q'' at the same position but placed at $z = -d$ directly beneath the actual charge as before. Unlike in the case of the conductor, one must consider inside the boundary (ϕ_1); since there are no physical charges in this region, the only image charge that can be included in the function describing the potential in this region is an image charge q'' at the location of the original charge. Whilst one could place a charge of equal magnitude this would be assuming that no screening of the field originating from the $z > 0$ domain occurs, which is not clear at this point.

As such, it can be stated that

$$\phi = \begin{cases} \frac{1}{4\pi\varepsilon_1}\left(\frac{q}{R_1} + \frac{q'}{R_2}\right), & z > 0. \\ \frac{1}{4\pi\varepsilon_2}\frac{q''}{R_1}, & z < 0. \end{cases} \tag{1.24}$$

in cylindrical coordinates ($R_1 = \sqrt{x^2 + y^2 + (d - z)^2}$, $R_2 = \sqrt{x^2 + y^2 + (d + z)^2}$).

Gauss's law in integral form for the dielectric displacement field shows that upon consideration of a cylindrical volume split between the two media, such that the top of the cylinder is one media and the bottom is in the other (this techniques is illustrated in figure 1.3), the dielectric displacement field is discontinuous such that

$$\oint_S \mathbf{D}.d\mathbf{A} = \sigma A = q \tag{1.25}$$

from which it can be seen that upon limiting the area to an infinitesimal size ($d\mathbf{A}$), it can be seen that the the dielectric displacement is discontinuous such that

$$\epsilon_1 \frac{\partial \phi_1}{\partial n_S} = \epsilon_2 \frac{\partial \phi_2}{\partial n_S} \tag{1.26}$$

which forms the first boundary condition. The second boundary condition of this system can be derived from the the curl of the electric field being zero due to equation 1.9; as such, the line integral around a closed path is also zero. Therefore, the electric field parallel to the boundary, in both media, must be equal such that

$$E_1^{\parallel} = E_2^{\parallel} \tag{1.27}$$

and the electrostatic potential is continuous across the boundary. [14]

Given the relationship between the dielectric displacement field and the electric field ($\mathbf{D} = \epsilon \mathbf{E}$), it is possible to utilise these boundary conditions to find the required values of our image charges (q' and q'') in terms of the real charge q by evaluating the potential in equation 1.24 in terms of $\mathbf{E}$ and $\mathbf{D}$. It is then possible to evaluate equations 1.26 and 1.27 with the resultant expression, from which it can be seen that

$$q - q' = q'', \ \frac{q + q'}{\varepsilon_1} = \frac{q''}{\varepsilon_2} \tag{1.28}$$

respectively. Solving this system of equations yields the result that

$$q' = \left(\frac{\varepsilon_1 - \varepsilon_2}{\varepsilon_1 + \varepsilon_2} \right) q \tag{1.29}$$

$$q'' = \left(\frac{2\varepsilon_2}{\varepsilon_1 + \varepsilon_2} \right) q \tag{1.30}$$

Allowing one to write the full form of the potential as

$$\phi = \begin{cases} \frac{1}{4\pi\varepsilon_1} \left(\frac{q}{\sqrt{s^2+(d-z)^2}} + \frac{(\varepsilon_1-\varepsilon_2)}{(\varepsilon_1+\varepsilon_2)} \frac{q}{\sqrt{x^2+y^2+(d+z)^2}} \right), & z > 0. \\ \frac{1}{4\pi\varepsilon_2} \frac{2\varepsilon_2}{(\varepsilon_1+\varepsilon_2)} \frac{q}{\sqrt{x^2+y^2+(d-z)^2}}, & z < 0. \end{cases} \tag{1.31}$$

which can be converted to Cartesian coordinates via $s^2 = x^2 + y^2$.

1.2.2 Interacting Particles of Finite Size

Whilst image charge methods provide a means to study the potential of and field surrounding boundaries between various materials due to the presence of free charges away from the boundary, in the case of interacting dielectric particles a Monte-Carlo search is required in order to solve the resultant equations for the interaction energy and forces acting on the system.[15, 16] However, it is important to provide a rigorous characterization and mathematical framework of the exact solution, which contains no discretization errors or non-physical charges. [17]

A physically well-founded approach to the interaction of two dielectric particles was considered by Bichoutskaia *et al*[18], who developed such a solution to calculate the force and interaction energy between two dielectric particles, of radius (a_i) and charge (q_i), that may be composed of different materials as defined by their dielectric constant (κ_i), as defined via equation 1.13. In this

model, the particles are considered as dielectric such that the charge carrier mobility is considered to be 0. [6, 7]

At the surface of a dielectric particle both the free and total charge density, as in equation 1.26, can be described by a set of field discontinuities as described by the boundary conditions defined in the previous section. As such, it is assumed the free charge is distributed on the surface, the lowest energy configuration of the free charge, and is immobile. As there are no volume charges present within the particle, the surface charge distribution can be decomposed such that

$$\sigma = \sigma_b + \sigma_f \tag{1.32}$$

where σ_b is the surface charge distribution due to the movement of bound charges in the system, in one of the possible ways discussed in figure 1.1, and σ_f is the surface charge distribution due to free charge in the system which is assumed to be of a specified and immobile charge distribution on the surface.

Legendre Rationale

Considering this system as one set of point charges $\{\partial q_i\}$ spherically clustered around a point Ω_1, and another set $\{\partial q_j\}$ spherically clustered around another point Ω_2, such that the spheres formed by the non-overlapping sets of point charges make up the surface of a spherical particle. For a general vector $\mathbf{r}_{XY} = \mathbf{r}_Y - \mathbf{r}_X$, this can be stated as

$$|\mathbf{R}_{\Omega_1\Omega_2}| > |\mathbf{r}_{Bj} - \mathbf{r}_{Ai}| \text{ for all } i, j. \tag{1.33}$$

where $\mathbf{R}$ is a point outside the charge distribution, and $\mathbf{r}_i$ and $\mathbf{r}_j$ are the positions of the point charges being considered. This summation can be computed, via the principle of superposition for the electric potential, such that

$$\phi_{\Omega_1\Omega_2} = \frac{1}{4\pi\epsilon_0} \sum_{i\in\Omega_1} \sum_{j\in\Omega_2} \frac{q_i q_j}{|\mathbf{r}_j - \mathbf{r}_i|}. \tag{1.34}$$

where $\frac{1}{|\mathbf{r}_j-\mathbf{r}_i|}$ can be rewritten as

$$\frac{1}{\|\mathbf{r_j} - \mathbf{r_{i'}}\|} = \frac{1}{\sqrt{r^2 + (r')^2 - 2rr'\cos\gamma}}$$

$$= \frac{1}{r\sqrt{1 + h^2 - 2h\cos\gamma}} \quad \text{with} \quad h := \frac{r'}{r}. \tag{1.35}$$

which is the generating function of the Legendre polynomials [19]

$$\frac{1}{\sqrt{1 + h^2 - 2h\cos\gamma}} = \sum_{\ell=0}^{\infty} h^\ell P_\ell(\cos\gamma) \tag{1.36}$$

Calculating the Interaction

Returning to the problem of two dielectric spheres Ω_1 and Ω_2, as depicted in figure 1.4, it is now clear that the potential at a point $\mathbf{r}_i$ ($i = 1, 2$) is dependent on a summation of the potential due to each charge ∂q_1 modelled on the surface of the respective particle. The particles geometry and composition is as defined in figure 1.4, and the interaction is assumed to occur in a vacuum ($\kappa = 1$).
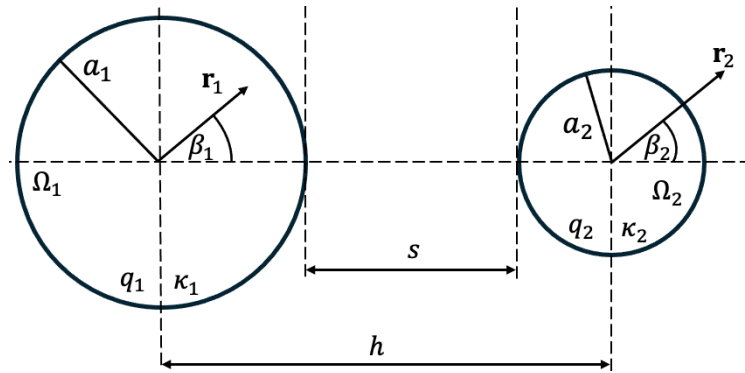
Figure 1.4: *An illustration of the geometric parameters defining two interacting, charged, spherical particles (Ω_1 and Ω_2) of radius, charge, dielectric constants, polar angle, center-to-centre separation, surface-to-surface separation denoted by a_1, a_2, q_1, q_2, κ_1, κ_2, β_1, β_2, s and h respectively.*

Given equation 1.2.2, the potential due to the total surface charge on the particles can be expressed as a finite set of Legendre polynomials in the form

of the multipole expansion, assuming convergence of the summation before $\ell = \infty$. In such an expansion the coefficients of the various contributions to the potential can be explicitly calculated as the multipole moments coefficients $(A_{i,l \vee m})$, and the dependence of each particle on the potential at a given point is explicit.

As such, the general solution to the Poisson equation describing a system of two charged dielectric particles (Ω_1 and Ω_2) could take the form

$$\Phi(\mathbf{r}_1) = \sum_{l=0}^{\infty} A_{1,l} \frac{r_1^l}{a_1^{2l+1}} P_l(\cos \beta_1) +$$
$$\sum_{l=0}^{\infty} \sum_{m=0}^{\infty} A_{2,m} \frac{(l+m)!}{l!m!} \frac{r_1^l}{h^{l+m+1}} P_l(\cos \beta_1) \quad \text{for } r_1 < a_1, \quad (1.37)$$

$$\Phi(\mathbf{r}_1) = \sum_{l=0}^{\infty} A_{1,l} \frac{1}{r_1^{l+1}} P_l(\cos \beta_1)$$
$$+ \sum_{l=0}^{\infty} \sum_{m=0}^{\infty} A_{2,m} \frac{(l+m)!}{l!m!} \frac{r_1^l}{h^{l+m+1}} P_l(\cos \beta_1) \quad \text{for } r_1 > a_1, \quad (1.38)$$

$$\Phi(\mathbf{r}_2) = \sum_{l=0}^{\infty} A_{2,l} \frac{r_2^l}{a_2^{2l+1}} P_l(\cos \beta_2)$$
$$+ \sum_{l=0}^{\infty} \sum_{m=0}^{\infty} A_{1,m} \frac{(l+m)!}{l!m!} \frac{r_1^l}{h^{l+m+1}} P_l(\cos \beta_2) \quad \text{for } r_2 < a_2, \quad (1.39)$$

$$\Phi(\mathbf{r}_2) = \sum_{l=0}^{\infty} A_{2,l} \frac{1}{r_2^{l+1}} P_l(\cos \beta_2)$$
$$+ \sum_{l=0}^{\infty} \sum_{m=0}^{\infty} A_{1,m} \frac{(l+m)!}{l!m!} \frac{r_2^l}{h^{l+m+1}} P_l(\cos \beta_2) \quad \text{for } r_2 > a_2. \quad (1.40)$$

where P_ℓ are the Legendre polynomials to the order l, h is the centre-to-centre

separation of the particles and β is the polar angle associated with the point at which the potential is being calculated.[20] The potential is defined inside and outside Ω_1 and Ω_2, centred at Ω_1 and Ω_2's centres respectively, where the interacting particles are as defined in figure 1.4. [18]

However, such a system of equations does not form the unique solution to the Poisson equation that would describe the proposed system. To this end, the following three boundary conditions are imposed on the system, such that

- Since **E** must be continuous tangentially to the particle (in the β direction),

$$\frac{1}{r_i}\frac{\partial \phi}{\partial \beta}\bigg|_{r_i=a_i^+} - \frac{1}{r_i}\frac{\partial \phi}{\partial \beta}\bigg|_{r_i=a_i^-} = 0 \tag{1.41}$$

- The normal component of the electric field **E** is discontinuous across the surface of the particle due to the presence of a net charge on the particle

$$\frac{1}{r_i}\frac{\partial \phi}{\partial r_i}\bigg|_{r_i=a_i^+} - \frac{1}{r_i}\frac{\partial \phi}{\partial r_j}\bigg|_{r_i=a_i^-} = 4\pi K \sigma_i \tag{1.42}$$

- As the free charge causes the discontinuity in the electric field, the displacement field **D** is also discontinuous across the boundary such that

$$\frac{1}{r_i}\frac{\partial \phi}{\partial r_i}\bigg|_{r_i=a_i^+} - \kappa_i \frac{1}{r_i}\frac{\partial \phi}{\partial r_j}\bigg|_{r_i=a_i^-} = 4\pi K \sigma_{i,f} \tag{1.43}$$

where a_i^+ and a_i^- denote outside ($a_i < r_i$, $\kappa = 1$) and inside ($a_i > r_i$, $\kappa = \kappa_i$) the particle. Hence, it is possible to evaluate the surface charge distribution on each particle as

$$\sigma_i(\beta) = \frac{1}{4\pi K}\sum_{l=0}^{\infty} A_{i,l}\frac{2l+1}{a_i^{l+2}}P_l(\cos\beta_i) \quad \text{for} \quad i = 1,2; \tag{1.44}$$

with multipolar coefficients dictated by

$$4\pi K a_1 \sigma_{f,1}\delta_{l,0} = \frac{A_{1,l}}{a_1^{l+1}} + \frac{(k_1-1)l}{(k_1+1)l+1}\sum_{m=0}^{\infty}\frac{A_{2,m}}{l!m!}(l+m)!\frac{a_1^l}{h^{l+m+1}} \tag{1.45}$$

$$4\pi K a_2 \sigma_{f,2} \delta_{l,0} = \frac{A_{2,l}}{a_2^{l+1}} + \frac{(k_2 - 1)l}{(k_2 + 1)l + 1} \sum_{m=0}^{\infty} \frac{A_{1,m}}{l!m!}(l+m)! \frac{a_2^l}{h^{l+m+1}} \qquad (1.46)$$

which describe the mutual polarisation each particle undergoes upon interaction.

Utilising a generalized form of the Coulomb equation can be formed to account for the interaction of such spheres of charges (dielectric spheres where the charges are considered the elements dq and dq')

$$\mathbf{F}_{12} = K \int dq_1(\mathbf{r}_1) \int dq_2(\mathbf{r}_2) \frac{\mathbf{r}_1 - \mathbf{r}_2}{|\mathbf{r}_1 - \mathbf{r}_2|^3}, \qquad (1.47)$$

enables one to calculate the force on each particle, which following the rationale utilized to derive equations 1.37—1.40, can be evaluated as

$$F_{12} = -\frac{1}{K} \sum_{l=0}^{\infty} A_{1,l} A_{1,l+1} \frac{(k_1 + 1)(l+1) + 1}{(k_1 - 1)a_1^{2l+3}}, \qquad (1.48)$$

which upon consideration of σ_f's role in the third boundary condition (equation 1.43), as deduced in Bichoutskaia *et al*, can be explicitly written in the form of

$$
\begin{aligned}
F_{12} = K\frac{q_1 q_2}{h^2} &- q_1 \sum_{m=1}^{\infty} \sum_{l=0}^{\infty} A_{1,l} \frac{(k_2 - 1)m(m+1)}{(k_2 + 1)m + 1} \\
&\times \frac{(l+m)!}{l!m!} \frac{a_2^{2m+1}}{h^{2m+l+3}} - \frac{1}{K} \sum_{l=1}^{\infty} A_{1,l} A_{1,l+1} \frac{(k_1 + 1)(l+1) + 1}{(k_1 - 1)a_1^{2l+3}} \qquad (1.49)
\end{aligned}
$$

which is an analytical expression for the force acting between two dielectric charged spheres. A convergent regime ($\ell \to \infty$) can be found for this expression which is controlled by the highest degree of the Legendre polynomials utilised. The first term in equation 1.49 corresponds to the Coulomb force acting between point charges at the centre of each particle. The second and third term on the other hand, account for the contribution of the mutual polarisation of the two particles. As no material is less polarisable than the vacuum, the second and third terms are always negative and hence cause an attrac-

tive interaction between the particles. In the case of non-polarisable particles, ($\kappa_1 = \kappa_2 \rightarrow 1$ in a vacuum) the polarisation terms tend to zero and the solution converges upon the point charge. It can be seen that given equation 1.49, like charged particles may attract if the second and third term grow bigger than the first - this is discussed in more detail further in the text.

Since the publication of Bichoutskaia *et al*'s work[18], it has been expanded upon [17, 21–24] and utilised on a number of occasions in order to describe interactions between more complex charged objects, in both naturally occurring and novel systems both statistically and dynamically.[25–28]

1.3   Polarisabilities and the Casimir Force

Polarisation can occur in a plethora of environments, and, up to now, only charge induced polarisation of classical particles has been considered. Polarisation between neutral bodies can also be seen to occur on both the molecular level at angstrom separations (Å), and between macroscopic particles at nanometre (nm) separations. One example of a polarisation dependent interaction is the instantaneous, and spontaneous, dipoles formed within a molecule inducing/effecting instantaneous polarisation on a nearby molecule - the van der Waals interaction. A generalisation of this for bulk macroscopic systems was proposed by Lifshitz[29, 30], based on earlier work by Hendrik Casimir [31, 32].

Casimir and Polder initially illustrated that quantum mechanics predicts an interaction between a neutral atom and a perfectly conducting plane (zero resistivity) as a generalization of the van der Waals interaction. Casimir then derived the same expression by considering the allowed vacuum fluctuations occurring in such a system; he later generalized this to the case of two perfectly conducting infinite plates.[31, 32]

Casimir's original derivation considered a cubic volume of side L, with the top side of the cube missing, and all remaining sides composed of ideally conducting

plates; he then introduced another square piece of ideal conductor, of side L, placed at some distance a from the bottom internal face of the box (xy-plane). The equations dictating the allowed wavelengths of standing waves between the xy-plane and the perfect conductor (the cavity) are

$$0 \leq \lambda_x \leq L,\ 0 \leq \lambda_y \leq L,\ 0 \leq \lambda_z \leq a \qquad (1.50)$$

the wavelengths of which correspond to quantised frequencies/wave numbers described by

$$k_x = \pi n_x / L,\ k_y = \pi n_y / L,\ k_z = \pi n_z / a,\ n = 1, 2, 3...n \qquad (1.51)$$

The expectation value for the energy (the expected measurement of an experiment) of the standing waves within such a cavity can be found via a summation over all the standing waves formed in the cavity where there are n standing waves, and therefore energies (E_n), present

$$\langle E \rangle = \frac{1}{2} \sum_{n=0}^{\infty} E_n, \qquad (1.52)$$

where the factor of a half is present due to the zero-point energy of each n'th mode. Whilst this sum is divergent in nature, it can be used to calculate finite expressions. Assuming the size of the plates is extremely large, k_x and k_y can be treated as continuous variables, which utilising $E_n = \hbar \omega_n$ and periodic boundary conditions enables one to write the summation of equation 1.52 as an integral of the form

$$\frac{1}{2} \sum \hbar \omega_n =$$
$$\hbar c \frac{L^2}{\pi^2} \int_0^\infty \int_0^\infty \left[\frac{1}{2} \sqrt{k_x^2 + k_y^2} + \sum_{n=1}^{\infty} \sqrt{n^2 \frac{\pi^2}{a^2} + k_x^2 + k_y^2} \right] dk_x\, dk_y \quad (1.53)$$

where the first integral is due to standing waves across the width of the box, and the second is in the z-direction. Considering polar coordinates in the $k_x k_y$

plane, gives

$$\frac{1}{2}\sum \hbar\omega = \hbar c \cdot \frac{L^2}{\pi^2} \cdot \frac{\pi}{2} \sideset{}{'}\sum_0^\infty \int_0^\infty \left(\sqrt{n^2\frac{\pi^2}{a^2} + \varkappa^2}\right) \varkappa d\varkappa \tag{1.54}$$

where $\varkappa^2 = k_x^2 + k_y^2$, and the prime denotes the division of the first term by two. If the inserted plate is far from the xy plane at the bottom of the box, such that k_x can be considered a continuous variable, the sum of the surface modes can be computed as an integral as

$$\frac{1}{2}\sum \hbar\omega = \int_0^\infty \int_0^\infty \left(\sqrt{k_z^2 + \varkappa^2}\, \varkappa\, d\varkappa\right)\left(\frac{a}{\pi}dk_z\right). \tag{1.55}$$

Therefore the difference in the energy between the two separations can be seen as an interaction energy ΔE which is equal to

$$\Delta E = \hbar c \cdot \frac{L^2}{\pi^2} \cdot \frac{\pi}{2} \sideset{}{'}\sum_0^\infty \int_0^\infty \left(\sqrt{n^2\frac{\pi^2}{a^2} + \varkappa^2}\right) \varkappa d\varkappa$$
$$- \int_0^\infty \int_0^\infty \left(\sqrt{k_z^2 + \varkappa^2}\, \varkappa\, d\varkappa\right)\left(\frac{a}{\pi}dk_z\right) \tag{1.56}$$

Although this expression is not finite, it is not devoid of physical meaning as if ΔE is non-zero, a force will be present in the system. By use of a regulatory function by multiplication, one can then apply the Euler-Maclaurin formula to the expression, obtaining

$$\frac{\Delta E}{L^2} = \frac{\Delta E}{A} = -\frac{\hbar c \pi^2}{720}\frac{1}{a^3} \tag{1.57}$$

for the interaction energy per unit area, and

$$\frac{F}{A} = -\frac{\hbar c \pi^2}{240}\frac{1}{a^4} \tag{1.58}$$

for the force per unit area acting on the plate. [31]

With this formalism, Casimir illustrated the purely quantum mechanical interaction of the Casimir force that occurs between two neutral, ideally conducting

plates due to the in-equivalence of vacuum states inside and outside the cavity. Physically, this can be justified as the cavity causing an increase in the number of virtual photons interacting between the two plates as certain states become inaccessible as the cavity tends to zero volume.

Lifshitz extended this formalism in 1961 by considering the eigenvalues of the Hamiltonian describing a system of two real solids separated by some distance. In their work, Dzyaloshinskii, Lifshitz and Pitaevskii decomposed the Hamiltonian describing the electromagnetic waves in the system into those of a similar wavelength to atomic distances, and those larger - considering those larger as a perturbation to the system.[30] This formalism utilised the Matsuabra technique[33] to evaluate the perturbative Hamiltonian as Green's functions in the fictitious 'imaginary time' regime. This can be seen to result in the free energy of the system $G(l, i\xi_n)$ being described by

$$G(\ell, i\xi_n) = \frac{k_B T}{2\pi c^2} \sum_{n=0}^{\infty} \epsilon_m(i\xi_n)\xi_n^2 \int_1^{\infty} p \ln[D(\ell, i\xi_n)]dp \qquad (1.59)$$

where k_B is the Boltzmann constant, T is the temperature and c is the speed of light.[34] The dielectric function of a material, $\epsilon(i\xi_n)$, is defined at the relevant Matsubara frequencies

$$\xi_n = \frac{2\pi n k_B T}{\hbar},$$

where $\hbar$ is the reduced Planck constant.

The function $D(\ell, i\xi_n)$ includes the dielectric properties of the boundaries of the cavity (Am and Bm, where A and B are the boundaries and m is the medium) as

$$D(\ell, i\xi_n) = (1 - \Delta_{Am}(i\xi_n)\Delta_{Bm}(i\xi_n)e^{-2\rho_m\ell}), \tag{1.60}$$

$$\rho_m = \frac{\sqrt{\epsilon_m(i\xi_n)}\xi_n}{c}p$$

where $1 \le p < \infty$; $\Delta(i\xi_n)$ varies depending on the geometry of the problem and, in the simplest case of a single composition half-space, such as the planar boundaries shown earlier in figure 1.3, it takes the following form for the surface A

$$\Delta_{Am} = \frac{s_A\epsilon_m - s_m\epsilon_A}{s_A\epsilon_m + s_m\epsilon_A}, \tag{1.61}$$

$$s_A = (p^2 - 1 + (\epsilon_A/\epsilon_m))^{1/2}, \quad s_m = p$$

where $\epsilon_A = \epsilon_A(i\xi_n)$ is the dielectric function of the surface A at a given complex frequency $i\xi_n$ and s_A is the corresponding component of the radial wave vector at the same frequency. A separate expression for Δ_{Bm} is derived by replacing A for B in equation (1.61). [34]

Whilst imaginary frequencies as shown in equation (1.60) may appear unphysical in nature, they can be well justified here by their use as the argument of the materials dielectric permittivity, which is a function of frequency and can take complex values[29, 30], such that

$$\epsilon(\omega) = \epsilon'(\omega) + i\epsilon''(\omega) \tag{1.62}$$

where ϵ'' is always positive and determines the dissipation of the energy of an electromagnetic wave propagating in the medium to which it corresponds. Given the Kramers-Kronig relation [35], it can be seen that for complex arguments, $\epsilon(i\omega)$, evaluated at the relevant Matsubara frequencies, ξ_n

$$\epsilon(i\xi) = 1 + \frac{2}{\pi} \int_0^\infty \frac{\omega\, \epsilon''(\omega)}{\omega^2 + \xi^2}\, d\omega \qquad (1.63)$$

has real positive values.

Given Lifshitz presented formalism, it can be shown that it is possible to extend this formalism to account for inhomogeneous boundaries. Given the nature of his derivation, its of no surprise that this formalism has proven to model experiments incredibly accurately, given a suitable choice of $\epsilon(\omega)$.[36, 37]

1.4 Conclusion

Electrostatic and electrodynamics interactions occur readily between various materials, many of which fundamentally rely on the polarisation of the media present. This can be seen to be the case for all the interactions studied thus far, including but not limited to a point charge polarising a plane, two particles polarising each other, or the attraction of two neutral plates via the Casimir effect.

By correctly adapting and adopting the various formalisms presented throughout this (brief) introduction, it is possible to extend and apply such ideas to both natural and novel environments for technological application and scientific discovery. This can be seen by the varied and numerous extensions and applications to Bichoutskaia *et al*'s two particle formalism[17, 21–28], and the abundance of recent research into the Casimir interaction.[38–46]

Chapter 2

Modelling Charge Induced, Many-Body Interactions

2.1   Introduction

Charge induced many-body interactions occur in a plethora of natural and novel environments [26, 47–49], but are rarely accounted for due to their complexity and computational cost. Lindgren *et al*[49] developed an efficient implementation of a numerical method to determine the interaction between N dielectric particles. This framework employed a Galerkin approximation of an integral equation formulation that generally describes the boundary conditions of the surface charge of dielectric particles. In particular, this formalism [49] is able to account for interactions in any continuous, non-electrolyte, solution to accurately predict the behaviour of many-body systems embedded within various media. All the particles within this formalism are assumed to be spherical, and are described by their radii, relative dielectric permittivity and surface charge.

The algorithmic complexity of such a system is high and as such a method to increase the computational efficiency of such a solution was required. To this end, Lindgren *et al*[49] employed an adaptation of the fast multipole method (FMM) to increase the efficiency of the evaluation of such a framework, the use

of which causes the method to scale linearly with N, and to third power with respect to the number of spherical harmonics; this is in contrast to the fourth order cost without FMM. This is possible due to the equivalence between a surface charge represented by a truncated series of spherical harmonics, and a corresponding multipole located at the centre of each particle. This method shows exponential convergence to achieve a smooth solution of the surface charge, and, hence, a numerically stable interaction energy as is required upon evaluation of charged particle interactions. There is no inherent error associated with the geometry of the system since no meshing is required. If azimuthal symmetry is present, as is common in two-body interactions, the scaling can be reduced to quadratic with respect to the number of spherical harmonics required due to the symmetric nature of the polarization.

This solution was shown [48, 49] to provide an accurate quantitative description of the interaction of N charged dielectric particles, whilst maintaining its computational efficiency. Also, as this particular solution converges up to the point where the particles touch, it can be employed as a force field in particle dynamics as shown in the literature [49] and throughout this work.

The framework developed by Lindgren *et al*, although efficient, is only applicable to interactions between particles with homogeneous (uniform) surface charge distributions, in the absence of externally applied electric fields. This is a consequence of the nature of the boundary conditions defined by Lindgren *et al* as the inclusion of such features changes the boundary conditions describing the potential, and hence the surface charge, of a polarisable dielectric particle in the presence of other particles.

Many particulates, especially within the nanometre size range, can possess an inhomogenous surface charge distribution which is often analogous to that of a single point charge localized on the surface of an otherwise neutral dielectric particle. This can occur due to small molecule termination of nanoparticles at a single site, or via ionisation events that could cause immobile charges/defects on the surface of a particle.[50, 51] Such systems are extremely orientation

dependent, and as such require formalisms such as those proposed by Lindgren *et al* to be modified in order to be utilised to calculate the interactions within populations of such particles.[49]

The effect of external electric fields on the surface charge distribution of dielectric particles has been well studied throughout the literature[52–54], however, the interaction between such particles is often approximated as the interaction between dipoles or multipoles which are inherently different from a polarisable, spherical, charged particle.

2.1.1 Aims and Objectives

To develop an extension to a current many-body formalism [49], and extensively test the new formalism to show that it is an accurate description of charge induced polarisation of particles with various surface charges, in the presence of external electric fields. This methodology will then be used to describe the electric field induced destabilisation of highly charged colloidal crystals, with experimental comparison. This work was published in [17] in collaboration with Prof. Benjamin Stamm, Dr Mohammad Hassan and Dr Stefanie Braun, formerly of RWTH Aachen in conjunction with Prof. Elena Besley, Dr Joshua Baptiste. The derivation of this formalism is reproduced here for completeness and understanding, and the finer mathematical details can be found in appendix A.1 and A.2.

2.2   Formulation of the electrostatic many-body framework

A physical system of N non-overlapping dielectric spherical particles is defined herein by their radii $\{r_i\}_{i=1}^{N}$, centres $\{\mathbf{x}_i\}_{i=1}^{N}$, and dielectric constants $\{\kappa_i\}_{i=1}^{N}$, immersed in a background medium (solvent) which has dielectric constant $\kappa_0 > 0$. The many-body system is considered at rest. The spherical particles are described as open balls denoted by $\{\Omega_i\}_{i=1}^{N}$ with surfaces $\{\partial\Omega_i\}_{i=1}^{N}$. The surfaces of the dielectric particles represent the boundary $\partial\Omega$ between the interior Ω^- and the exterior Ω^+ of the particles. We assume that this surface $\partial\Omega$ carries a given free charge distribution σ_f and that there is no charge in the interior of the particles, i.e., in Ω^- (See appendix A.1 for a precise mathematical description of these quantities). To account for the point-charge contribution to the surface free charge, the free charge σ_f is split into two contributions

$$\sigma_f = \sigma_s + \sigma_p. \tag{2.1}$$

Here, $\sigma_s \in L^2(\Omega)$ corresponds to the square-integrable part of the surface charge, whereas σ_p is defined as the point-charge contribution to the free charge represented by a linear combination of one or several Dirac delta distributions per particle, dependent on the system under investigation:

$$\sigma_p := \sum_{j=1}^{N}\sum_{k=1}^{N_{\mathrm{p}}^{j}} q_{j,k}\delta_{\mathbf{z}_{j,k}}, \quad \text{where} \quad q_{j,k} \in \mathbb{R}, \quad \mathbf{z}_{j,k} \in \partial\Omega_j \tag{2.2}$$

and for all $j = 1,\ldots,N$ $k = 1,...,N$.

The *external* potential, due to the presence of an external electric field, is defined as Φ_{ext} with associated *external* electric field $\mathbf{E}_{\mathrm{ext}} := -\nabla\Phi_{\mathrm{ext}}$, which

is not limited by the constraint that Φ_{ext} tends to zero at infinity. Here, the external potential is considered to be harmonic, i.e., $\Delta\Phi_{\text{ext}} = 0$, so that the charges creating the external field are not considered within the system. Furthermore, the electric field $\mathbf{E}_{\text{ext}}$ is not restricted to be *uniform*. Finally, it is assumed that the system of dielectric particles does not affect the external field $\mathbf{E}_{\text{ext}}$, for instance, through polarisation, which justifies the use of our terminology *external*.

To this extent, the aim is to determine the total surface charge on each dielectric particle after taking into account both the free charge σ_f, and the bound charges resulting from polarisation effects due to the presence of charged neighbouring particles, and the effects of an external electric field. Using the total surface charge, it is possible to deduce other physical quantities of interest such as the electrostatic forces and energy resulting from the interaction of N charged dielectric spheres both with each other and with an external electric field.

In order to determine the total surface charge, one must first derive equations governing the *total electrostatic potential*. It is shown here, as in [17], that the total electrostatic potential can be used to deduce the required total surface charge as well as the subsequent physical quantities of interest. The main challenges in achieving such evaluations lie in the singular nature of the point-charges σ_p and the external potential Φ_{ext}, which does not decay to zero at infinity.

2.2.1   Formulation based on partial differential equations

The problem of the electrostatic interaction between N charged dielectric spheres can be described by a partial differential equation (PDE)- based transmission problem. Defining the *total* potential $\Phi_{\text{tot}} := \Phi_{\text{ext}} + \Phi$, gives that the corresponding *total* electric field is $\mathbf{E}_{\text{tot}} := \mathbf{E}_{\text{ext}} + \mathbf{E}$, where $\mathbf{E}$ is the *perturbation* of $\mathbf{E}_{\text{ext}}$ due to the presence of dielectric charged particles, and Φ is the corre-

sponding perturbation potential so that $\mathbf{E} = -\nabla\Phi$. Standard arguments from the theory of electrostatics in dielectric media imply that the total potential Φ_{tot} satisfies the following transmission problem:

$$-\Delta\Phi_{\text{tot}} = 0 \qquad \text{in } \Omega^- \cup \Omega^+,$$
$$[\![\Phi_{\text{tot}}]\!] = 0 \qquad \text{on } \partial\Omega, \tag{2.3}$$
$$[\![\kappa\nabla\Phi_{\text{tot}}]\!] = \sigma_{\text{f}} \qquad \text{on } \partial\Omega.$$

Here, κ is the dielectric function which takes the value of κ_i on the spherical particle Ω_i and κ_0 on Ω^+ (medium), and $[\![\Phi_{\text{tot}}]\!]$ and $[\![\kappa\nabla\Phi_{\text{tot}}]\!]$ are jump discontinuities defined by

$$[\![\Phi_{\text{tot}}]\!](\mathbf{x}) := \Phi_{\text{tot}}(\mathbf{x})|_{\Omega_i} - \Phi_{\text{tot}}(\mathbf{x})|_{\Omega^+}, \qquad\qquad \text{for } \mathbf{x} \in \partial\Omega_i$$
$$[\![\kappa\nabla\Phi_{\text{tot}}]\!](\mathbf{x}) := \kappa_i\nabla\Phi_{\text{tot}}(\mathbf{x})|_{\Omega_i} \cdot \eta(\mathbf{x}) - \kappa_0\nabla\Phi_{\text{tot}}(\mathbf{x})|_{\Omega^+} \cdot \eta(\mathbf{x}) \quad \text{for } \mathbf{x} \in \partial\Omega_i,$$

where $\eta(\mathbf{x})$ is the normal unit vector at $\mathbf{x} \in \partial\Omega$ pointing towards the exterior of the particles.

In general, Equation (2.3) is ill-posed as can be seen, for instance, by observing that if $\sigma_f \equiv 0$, then any constant function Φ_{tot} will satisfy this equation. In order to obtain the correct total potential Φ_{tot}, the relation $\Phi_{\text{tot}} = \Phi_{\text{ext}} + \Phi$ can be employed to first derive a well-posed equation for the *perturbed* electrostatic potential Φ. Using decomposition (2.1), elementary algebra shows that Φ satisfies the following transmission problem

$$-\Delta\Phi = 0 \qquad\qquad\qquad \text{in } \Omega^- \cup \Omega^+,$$
$$[\![\Phi]\!] = 0 \qquad\qquad\qquad \text{on } \partial\Omega,$$
$$[\![\kappa\nabla\Phi]\!] = \sigma_s + \sigma_p - (\kappa - \kappa_0)\partial_n\Phi_{\text{ext}} \qquad \text{on } \partial\Omega, \tag{2.4}$$
$$|\Phi| \to 0 \qquad\qquad\qquad \text{as } |\mathbf{x}| \to \infty,$$

where $\partial_n\Phi_{\text{ext}}$ denotes the normal derivative of Φ_{ext} on the boundary $\partial\Omega$.

PDEs similar to the transmission problem (2.4) have previously been consid-

ered in the literature (see, e.g., [49, 55]), but the key novelty of Equation
(2.4) is the addition of contributions due to an external electric field and the
presence of point-charges on the surface of dielectric particles. These addi-
tional terms require significant modifications to earlier definitions [55–57] of
the electrostatic force and interaction energy for the N-body charged dielec-
tric spheres, and they present additional challenges in the efficient numerical
implementation.

In addition to the presence of the highly non-regular point-charge term σ_p, an-
other difficulty in solving the transmission problem described in equation (2.4)
is the fact that the equation is posed on the entire space $\mathbb{R}^3$. Indeed, since the
potential Φ *a priori* decays only as $|\mathbf{x}|^{-1}$, a naive truncation of the computa-
tional domain in an effort to use classical algorithms, such as the finite element
method, leads to significant errors. The usual approach to circumventing this
problem is to appeal to the theory of integral equations and reformulate the
transmission problem (2.4) as a so-called boundary integral equation (BIE)
posed on the interface $\partial\Omega$. This is the subject of the next subsection.

2.2.2   Formulation based on boundary integral equations

In order to describe fully the integral equation-based approach to the problem
of electrostatic interaction between charged dielectric spheres, additional no-
tions are required. First, the single layer potential of some density ν, denoted
$\mathcal{S}\nu$, is defined as a mapping with the property that

$$(\mathcal{S}\nu)(\mathbf{x}) := \int_{\partial\Omega} \frac{\nu(\mathbf{y})}{4\pi|\mathbf{x} - \mathbf{y}|} \, d\mathbf{y}, \qquad \forall \mathbf{x} \in \Omega^- \cup \Omega^+. \tag{2.5}$$

It can be shown that for any density ν, $\mathcal{S}\nu$ is a harmonic function in $\Omega^- \cup \Omega^+$,
which additionally satisfies the following jump conditions

$$[\![\mathcal{S}\nu]\!] = 0; \qquad [\![\nabla\mathcal{S}\nu]\!] = \nu.$$

As a consequence, it is possible to consider a restriction of the single layer potential defined through Equation (2.5) on the boundary $\partial\Omega$ and thereby define the so-called *single layer boundary* operator, denoted $\mathcal{V}$ as the improper integral

$$(\mathcal{V}\sigma)(\mathbf{x}) := \int_{\partial\Omega} \frac{\nu(\mathbf{y})}{4\pi|\mathbf{x}-\mathbf{y}|}\, d\mathbf{y}, \qquad \forall \mathbf{x} \in \partial\Omega.$$

Note, that occasionally it will be necessary to consider the "local" single layer potential and boundary operators defined on an individual sphere $i \in \{1, \dots, N\}$. These will be denoted as $\mathcal{S}_i$ and $\mathcal{V}_i$ respectively. One should also note that $\mathcal{V}$ is an invertible operator.

The surface electrostatic potential $\lambda := \Phi|_{\partial\Omega}$ is now described by the following BIE:

$$\lambda - \mathcal{V}\left(\frac{\kappa_0 - \kappa}{\kappa_0}\mathrm{DtN}\lambda\right) = \frac{1}{\kappa_0}\mathcal{V}(\sigma_s + \sigma_p) + \frac{\kappa_0 - \kappa}{\kappa_0}\mathcal{V}(\partial_n\Phi_{\mathsf{ext}}). \qquad (2.6)$$

Here, the notation DtN is used to denote the local Dirichlet-to-Neumann (DtN) map on the surface $\partial\Omega$ (see Appendix A for further details).

An equivalent reformulation of the BIE (2.6) for the induced surface charge can be achieved by applying $\mathcal{V}^{-1}$ to both sides of the equation, and defining $\nu := \mathcal{V}^{-1}\lambda$ which yields the following BIE

$$\nu - \frac{\kappa_0 - \kappa}{\kappa_0}\mathrm{DtN}\mathcal{V}\nu = \frac{1}{\kappa_0}(\sigma_s + \sigma_p) + \frac{\kappa_0 - \kappa}{\kappa_0}(\partial_n\Phi_{\mathsf{ext}}). \qquad (2.7)$$

In Equation (2.7), the quantity of interest ν, i.e. *induced surface charge*, represents (up to a scaling factor) the total surface charge on each dielectric particle after taking into account both the free charge σ_f and the bound charge resulting from polarisation effects due to the presence of any remaining charged particles and the effect of an external electric field. More precisely,

- σ_f represents the free charge on each particle;

- $\sigma_b := (\kappa_0 - \kappa)\big(\mathrm{DtN}\mathcal{V}\nu + \partial_n\Phi_{\mathsf{ext}}\big)$ represents the bound charge on each particle;

- $\kappa_0\nu = \sigma_f + \sigma_b$ represents the total surface charge on each particle.

A simple manipulation of Equation (2.7) yields the following relation between the surface charge ν and the surface electrostatic potential λ:

$$\nu = \frac{\kappa_0 - \kappa}{\kappa_0}\mathrm{DtN}\lambda + \frac{1}{\kappa_0}\big(\sigma_s + \sigma_p\big) + \frac{\kappa_0 - \kappa}{\kappa_0}(\partial_n\Phi_{\mathsf{ext}}). \qquad (2.8)$$

Equation (2.8) implies that once λ is known, the charge distribution ν can be computed using the purely local DtN map. It should also be noted here that the relation between the PDE (2.4) and the BIE (2.6) representations of the electrostatic potential can be clearly established since λ is simply the restriction (more precisely the Dirichlet trace) of the electrostatic potential Φ on the boundary $\partial\Omega$. Thus, for any point $\mathbf{x} \in \Omega^- \cup \Omega^+$, we have $\Phi(\mathbf{x}) = \big(\mathcal{S}\mathcal{V}^{-1}\lambda\big)(\mathbf{x}) = (\mathcal{S}\nu)(\mathbf{x})$, and therefore $\Phi_{\mathsf{tot}}(\mathbf{x}) = \Phi_{\mathsf{ext}}(\mathbf{x}) + (\mathcal{S}\nu)(\mathbf{x})$.

As emphasised above, an important technical difficulty in the analysis of Equation (2.6) is the presence of the low-regularity point-charge term σ_p, which requires special treatment in the design of efficient numerical methods. The BIE (2.6) has previously been the subject of extensive analysis in a simpler case when surface point-charges and the external field are absent, i.e., when $\sigma_p \equiv 0$ and $\Phi_{\mathsf{ext}} \equiv 0$. Firstly, this methodology is briefly summarised, before explaining how the BIE (2.6) can be solved in this simple case before considering (in Section 2.3) the more complex problem of describing surface point-charges and an external electric field.

2.2.3 Methodology in the absence of surface point-charge and external field

In the absence of both the point-charge contribution to the surface free charge and an external electric field, the boundary integral equation (2.6) reads as

$$\widetilde{\lambda} - \mathcal{V}\left(\frac{\kappa_0 - \kappa}{\kappa_0}\mathrm{DtN}\widetilde{\lambda}\right) = \frac{1}{\kappa_0}\mathcal{V}\sigma_s. \tag{2.9}$$

Equation (2.9) is solved using a Galerkin discretisation with an approximation space constructed from the span of finite linear combinations of local spherical harmonics on each sphere $\partial\Omega_i$ (exact definitions of the spherical harmonics and the approximation space $W^{\ell_{\max}}$ can be found appendix A.1), as in [49]. More precisely, the Galerkin discretisation of the BIE (2.9) reads as follows: let $\ell_{\max}$ be a fixed discretisation parameter, we seek the Galerkin solution $\widetilde{\lambda}_{\ell_{\max}} \in W^{\ell_{\max}}$ which satisfies for all test functions $\psi_{\ell_{\max}} \in W^{\ell_{\max}}$ the equation

$$\left(\left(\widetilde{\lambda}_{\ell_{\max}} - \mathcal{V}\left(\frac{\kappa_0 - \kappa}{\kappa_0}\mathrm{DtN}\widetilde{\lambda}_{\ell_{\max}}\right)\right), \psi_{\ell_{\max}}\right)_{L^2(\partial\Omega)} = \frac{1}{\kappa_0}\left(\mathcal{V}\sigma_s, \psi_{\ell_{\max}}\right)_{L^2(\partial\Omega)}. \tag{2.10}$$

The Galerkin solution $\widetilde{\lambda}_{\ell_{\max}}$ and the test function $\psi_{\ell_{\max}}$ can be expanded as a finite linear combination of basis functions. This *ansatz* allows us to reduce the Galerkin discretisation (2.10) to a linear system of equations for the unknown expansion coefficients of $\widetilde{\lambda}_{\ell_{\max}}$. Equation (2.10) thus yields the linear system

$$\boldsymbol{A}\widetilde{\boldsymbol{\lambda}} = \widetilde{\boldsymbol{F}}, \tag{2.11}$$

where the solution matrix $\boldsymbol{A}$ and the vector $\widetilde{\boldsymbol{F}}$ are defined as

$$[\boldsymbol{A}_{ij}]_{\ell\ell'}^{mm'} := \left(\mathcal{Y}_{\ell'm'}^j - \mathcal{V}\left(\frac{\kappa_0 - \kappa}{\kappa_0}\mathrm{DtN}\mathcal{Y}_{\ell'm'}^j\right), \mathcal{Y}_{\ell m}^i\right)_{L^2(\partial\Omega_i)},$$
$$[\widetilde{\boldsymbol{F}}_i]_\ell^m := \frac{1}{\kappa_0}\left(\mathcal{V}\sigma_s, \mathcal{Y}_{\ell m}^i\right)_{L^2(\partial\Omega_i)}, \tag{2.12}$$

where $\mathcal{Y}_{\ell m}^i$ denotes the spherical harmonic of degree ℓ and order m on the

sphere $\partial\Omega_i$ and the indices $i, j \in \{1, \ldots, N\}$, $\ell, \ell' \in \{0, \ldots, \ell_{\max}\}$ and $|m| \leq \ell$, $|m'| \leq \ell'$. A more detailed definition of $\mathcal{Y}_{\ell m}^i$ can be found in appendix A.1, and a detailed explanation of how to compute the entries in the solution matrix $\boldsymbol{A}$ and vector $\widetilde{\boldsymbol{F}}$ can be found in Lindgren *et al.* [49] Here, it is simply remarked that apart from the diagonal terms ($i = j$), computing the entries of the solution matrix and vector $\widetilde{\boldsymbol{F}}$ requires evaluating a double integral on the unit sphere. This typically requires the use of numerical quadrature, for which purpose Lebedev grid points are used.

Due to the form of (2.12), it is also possible to use a modification of the classical FMM to speed up computation of the vector $\widetilde{\boldsymbol{F}}$ and matrix-vector products involving the dense solution matrix $\boldsymbol{A}$. The FMM allows computing the action of the single layer boundary operator $\mathcal{V}$ on an arbitrary element of the approximation space with linear scaling computational cost (with respect to N). Since the DtN map is a purely local operator (diagonal in the basis of local spherical harmonics), the solution matrix $\boldsymbol{A}$ does not need to be explicitly computed and stored, and its action on an arbitrary vector can be calculated with linear scaling cost. Further details on the FMM implementation can be found in Lindgren *et al.* [49]

Once the vector $\widetilde{\boldsymbol{F}}$ has been computed and the procedure for applying the solution matrix $\boldsymbol{A}$ to an arbitrary vector in the approximation space is set up, the linear system (2.11) can be solved using a Krylov subspace solver such as GMRES (see Bramas *et al* [56] for a detailed convergence analysis of GMRES as applied to this linear system).

The approximate electrostatic interaction energy of a dielectric N-body system is given by

$$\widetilde{\mathcal{E}}_{\text{int}}^{\ell_{\max}} := \frac{1}{2}\left(\sigma_s, \widetilde{\lambda}_{\ell_{\max}}\right)_{L^2(\partial\Omega)} - \frac{1}{2}\sum_{j=1}^{N}\left(\sigma_{s,j}, \widetilde{\lambda}_{\ell_{\max}}^{jj}\right)_{L^2(\partial\Omega_j)}, \qquad (2.13)$$

where $\sigma_{s,j} = \sigma_s|_{\partial\Omega_j}$ and $\widetilde{\lambda}_{\ell_{\max}}^{jj} \in W^{\ell_{\max}}(\partial\Omega_j)$ is the approximate self-potential

generated by the free charge $\sigma_{s,j}$ on sphere $\partial\Omega_j$ in the absence of other spheres. More precisely, it is defined as the solution to the local Galerkin discretisation

$$\left(\widetilde{\lambda}_{\ell_{\max}}^{jj} - \mathcal{V}_j \text{DtN}_j\left(\frac{\kappa_0 - \kappa_j}{\kappa_0}\widetilde{\lambda}_{\ell_{\max}}^{jj}\right), \psi_{\ell_{\max}}^{jj}\right)_{L^2(\partial\Omega_j)} = \left(\frac{1}{\kappa_0}\mathcal{V}_j\sigma_{s,j}, \psi_{\ell_{\max}}^{jj}\right)_{L^2(\partial\Omega_j)}.$$

In definition (2.13) of the electrostatic interaction energy, the first term can be interpreted as the *total* electrostatic energy of the system whilst the second term, involving the summation, can be seen as the *self* energy.

Next, an expression for the approximate electrostatic forces is derived; as a first step, if $\widetilde{\lambda}_{\ell_{\max}}$ denotes a solution to the Galerkin discretisation (2.10) for a given free charge σ_s, then we define the approximate induced surface charge $\widetilde{\nu}_{\ell_{\max}}$ as the unique element of the approximation space $W^{\ell_{\max}}$ (defined in appendix A.1) that satisfies

$$\left(\mathcal{V}\widetilde{\nu}_{\ell_{\max}}, \psi_{\ell_{\max}}\right)_{L^2(\partial\Omega)} = \left(\widetilde{\lambda}_{\ell_{\max}}, \psi_{\ell_{\max}}\right)_{L^2(\partial\Omega)}. \tag{2.14}$$

This shows that, $\widetilde{\nu}_{\ell_{\max}}$ is simply an approximation of the exact induced surface charge ν, which physically represents the total surface charge on the dielectric spheres that includes polarisation effects. As such, $\widetilde{\nu}_{\ell_{\max}}$ is utilised to derive an expression for the approximate electrostatic force acting on the dielectric particles.

In practice, $\widetilde{\nu}_{\ell_{\max}}$ is *not* determined using Equation (2.14), which requires the computationally expensive inversion of the single layer boundary operator $\mathcal{V}$. Instead, a careful examination of the Galerkin discretisation (2.10) reveals that $\widetilde{\nu}_{\ell_{\max}}$ satisfies the relation (c.f., Equation (2.8))

$$\widetilde{\nu}_{\ell_{\max}} = \frac{\kappa_0 - \kappa}{\kappa_0}\text{DtN}\widetilde{\lambda}_{\ell_{\max}} + \frac{1}{\kappa_0}\sigma_s^{\ell_{\max}}, \tag{2.15}$$

where $\sigma_s^{\ell_{\max}}$ is the best approximation of σ_s in the approximation space $W^{\ell_{\max}}$. Consequently, once the linear system (2.11) has been solved, only purely local operations involving the Dirichlet-to-Neumann operator are required to obtain

$\widetilde{\nu}_{\ell_{\max}}$.

The approximate electrostatic force acting on the dielectric particle is now given by

$$\widetilde{\mathcal{F}}_i^{\ell_{\max}} := \kappa_0 \big(\widetilde{\nu}_{\ell_{\max}}, \mathbf{E}_{\mathsf{exc}}^i\big)_{L^2(\partial\Omega_i)}. \tag{2.16}$$

$\mathbf{E}_{\mathsf{exc}}^i$ is the i-excluded electric field generated by the approximate induced surface charge $\widetilde{\nu}_{\ell_{\max}}$, i.e., the vector field given by

$$\mathbf{E}_{\mathsf{exc}}^i(\mathbf{x}) = -\nabla \big(\mathcal{S}\widetilde{\nu}_{\ell_{\max}} - \mathcal{S}_i\widetilde{\nu}_{i,\ell_{\max}}\big)(\mathbf{x}), \tag{2.17}$$

where $\widetilde{\nu}_{i,\ell_{\max}} := \widetilde{\nu}_{\ell_{\max}}|_{\partial\Omega_i}$, and ∇ denotes the usual gradient taken with respect to Cartesian coordinates. The i-excluded electric field $\mathbf{E}_{\mathsf{exc}}^i$ is the part of the total electric field generated by the approximate induced charge $\widetilde{\nu}_{\ell_{\max}}$ that interacts with (i.e., exerts a net electrostatic force on) the dielectric particle Ω_i. A description of how to practically compute $\mathbf{E}_{\mathsf{exc}}^i$ in the current boundary integral framework can be found in [57].

Considering definitions (2.13) and (2.16) of the approximate electrostatic interaction energy and force, respectively, a key result [57] establishes that these are related by the identity

$$-\nabla_{\mathbf{x}_i}\widetilde{\mathcal{E}}_{\mathsf{int}}^{\ell_{\max}} = \widetilde{\mathcal{F}}_i^{\ell_{\max}},$$

where $\nabla_{\mathbf{x}_i}$ denotes the gradient taken with respect to the location of the centre $\mathbf{x}_i$ of the sphere $\partial\Omega_i$.

The Galerkin nature of the method presented here allows for a precise mathematical analysis in terms of accuracy with respect to $\ell_{\max}$ and complexity with respect to N, which was previously discussed in Hassan *et al* [55–57] and also included the detailed description of the linear scaling of the method and the accuracy of predictions for the electrostatic energy and forces.[57] However, the model is limited to the assumptions made at the beginning of Section 2.2.3,

namely, it does not account for the presence of surface point-charge and the effect of an external electric field. This extension and generalisation is the subject of the following section.

2.2.4   Extension to include an external electric field and surface point-charges

The external charge is defined as $\sigma_{\text{ext}} := -(\kappa - \kappa_0)\partial_n \Phi_{\text{ext}}$, which is simply the external electric field contribution to the right-hand side of the boundary integral equation (2.6). The Galerkin discretisation of the BIE (2.6) can be written as

$$\left(\lambda_{\ell_{\max}} - \mathcal{V}\left(\frac{\kappa_0 - \kappa}{\kappa_0} \text{DtN}\lambda_{\ell_{\max}} \right), \psi_{\ell_{\max}} \right)_{L^2(\partial\Omega)} =$$
$$\frac{1}{\kappa_0}\left(\mathcal{V}(\sigma_s + \sigma_{\text{ext}} + \sigma_p), \psi_{\ell_{\max}} \right)_{L^2(\partial\Omega)}. \quad (2.18)$$

As before, this Galerkin discretisation (2.18) yields a linear system of equations for the unknown local spherical harmonics expansion coefficients of $\lambda_{\ell_{\max}}$ of the form

$$\boldsymbol{A\lambda} = \boldsymbol{F}, \quad (2.19)$$

where the solution matrix $\boldsymbol{A}$ is defined precisely as before through Equation (2.12) and

$$[\boldsymbol{\lambda}_i]_\ell^m := \left(\lambda_{\ell_{\max}}, \mathcal{Y}_{\ell m}^i \right)_{L^2(\partial\Omega_i)}, \quad (2.20)$$

for $i \in \{1, \ldots, N\}$, $\ell \in \{0, \ldots, \ell_{\max}\}$ and $|m| \leq \ell$. Determining the new vector $\boldsymbol{F}$ requires some additional work due to the presence of the point-charge term σ_p. To this end, let $\mathbf{z}_j \in \partial\Omega_j \subset \partial\Omega$. The definition of the single layer boundary operator $\mathcal{V}$ implies that for any $q \in \mathbb{R}$ and all $\mathbf{x}$ in $\partial\Omega$ with $\mathbf{x} \neq \mathbf{z}_j$

we have

$$\mathcal{V}(q\delta_{\mathbf{z}_j})(\mathbf{x}) = \int_{\partial\Omega_j} \frac{q\delta_{\mathbf{z}_j}(\mathbf{y})}{|\mathbf{x} - \mathbf{y}|}\, d\mathbf{y} = \frac{q}{|\mathbf{x} - \mathbf{z}_j|}.$$

Hence,

$$\mathcal{V}(\sigma_p)(\mathbf{x}) = \sum_{j=1}^{N}\sum_{k=1}^{N_{\mathrm{p}}^{j}} \frac{q_{j,k}}{|\mathbf{x} - \mathbf{z}_{j,k}|},$$

and therefore the vector $\boldsymbol{F}$ in Equation (2.19) can be defined as

$$[\boldsymbol{F}_i]_\ell^m := \frac{1}{\kappa_0}\left(\mathcal{V}\big(\sigma_s + \sigma_{\mathsf{ext}}\big) + \mathcal{V}(\sigma_p)\,,\ \mathcal{Y}_{\ell m}^i\right)_{L^2(\partial\Omega_i)}. \tag{2.21}$$

Since the solution matrix $\boldsymbol{A}$ is exactly as before (see Section 2.2.3), one can use the same linear solver routine to approximate the solution to Equation (2.19). Having solved the underlying linear system, we can now compute further (approximate) physical quantities of interest.

In computing the approximate electrostatic forces, if $\lambda_{\ell_{\max}}$ denotes a solution to the Galerkin discretisation (2.18) for a given free charge $\sigma_f = \sigma_s + \sigma_p$ and external electric field $\mathbf{E}_{\mathsf{ext}}$ then the approximate induced surface charge $\nu_{\ell_{\max}}$ can be defined, as in Equation (2.14), which generates the surface electrostatic potential $\lambda_{\ell_{\max}}$ as the solution to

$$\big(\mathcal{V}\nu_{\ell_{\max}}, \psi_{\ell_{\max}}\big)_{L^2(\partial\Omega)} = \big(\lambda_{\ell_{\max}}, \psi_{\ell_{\max}}\big)_{L^2(\partial\Omega)}. \tag{2.22}$$

In practice, $\nu_{\ell_{\max}}$ can be determined again using the following relation (c.f., Equation (2.15)), which can be deduced from the Galerkin discretisation (2.18):

$$\nu_{\ell_{\max}} = \frac{\kappa_0 - \kappa}{\kappa_0}\mathrm{DtN}\lambda_{\ell_{\max}} + \frac{1}{\kappa_0}\left(\sigma_s^{\ell_{\max}} + \sigma_p^{\ell_{\max}} + \sigma_{\mathsf{ext}}^{\ell_{\max}}\right), \tag{2.23}$$

where $\sigma_s^{\ell_{\max}}, \sigma_p^{\ell_{\max}}$, and $\sigma_{\mathsf{ext}}^{\ell_{\max}}$ are the best approximations or projections (in the L^2-sense) of σ_s, σ_p, and σ_{ext} in the approximation space $W^{\ell_{\max}}$ defined in

appendix A.1. The approximate net electrostatic force acting on the dielectric particle described by the open ball Ω_i, $i \in \{1, \ldots, N\}$ is now given by

$$\mathcal{F}_i^{\ell_{\max}} := \kappa_0 \big(\nu_{\ell_{\max}}, \mathbf{E}_{\mathsf{exc}}^i + \mathbf{E}_{\mathsf{ext}} \big)_{L^2(\partial\Omega_i)}, \tag{2.24}$$

where $\mathbf{E}_{\mathsf{exc}}^i$ is the i-excluded electric field, which is defined analogously to Equation (2.17). Here $\mathbf{E}_{\mathsf{exc}}^i$ can practically be computed by adapting the procedure stated in [57] to the current setting of surface point charges and external electric field.

In contrast to the definition of the electrostatic forces, the definition of the *electrotatic interaction energy* is not straightforward in the current setting. On the other hand, in the chemical literature, the net force acting on a given dielectric particle is frequently defined as the negative-sphere centred gradient of the interaction energy. Keeping this relation in mind, the approximate electrostatic interaction energy of the system that corresponds to the approximate electrostatic force (2.24) is given by

$$\begin{aligned}
\mathcal{E}_{\mathsf{int}}^{\ell_{\max}} := &\frac{1}{2} \big(\sigma_s + \sigma_p + \sigma_{\mathsf{ext}}, \ \lambda_{\ell_{\max}} \big)_{L^2(\partial\Omega)} + \big(\sigma_s + \sigma_p, \ \lambda_{\mathsf{ext}}^{\ell_{\max}} \big)_{L^2(\partial\Omega)} \\
&+ \frac{1}{2} \big(\sigma_{\mathsf{ext}}, \ \lambda_{\mathsf{ext}}^{\ell_{\max}} \big)_{L^2(\partial\Omega)} - \frac{1}{2} \sum_{j=1}^{N} \big(\sigma_{s,j} + \sigma_{p,j}, \lambda_{\ell_{\max}}^{jj} \big)_{L^2(\partial\Omega_j)},
\end{aligned} \tag{2.25}$$

where $\sigma_{s,j} = \sigma_s|_{\partial\Omega_j}$, $\sigma_{p,j} := \sigma_p|_{\partial\Omega_j}$ and where $\lambda_{\mathsf{ext}}^{\ell_{\max}}$ is the best approximation of $\lambda_{\mathsf{ext}} := \Phi_{\mathsf{ext}}|_{\partial\Omega}$ and $\lambda_{\ell_{\max}}^{jj} \in W^{\ell_{\max}}(\partial\Omega_j)$ for the approximate self-potential on sphere $\partial\Omega_j$ in the absence of the external field $\mathbf{E}_{\mathsf{ext}}$ and all other spheres. The latter quantity is formally defined as the solution to the local Galerkin discretisation

$$\left(\lambda_{\ell_{\max}}^{jj} - \mathcal{V}_j \mathrm{DtN}_j \left(\frac{\kappa_0 - \kappa_j}{\kappa_0} \lambda_{\ell_{\max}}^{jj} \right), \psi_{\ell_{\max}}^{jj} \right)_{L^2(\partial\Omega_j)} = \left(\frac{1}{\kappa_0} \mathcal{V}_j (\sigma_{s,j} + \sigma_{p,j}), \psi_{\ell_{\max}}^{jj} \right)_{L^2(\partial\Omega_j)}.$$

With definitions (2.24) and (2.25) of the approximate electrostatic interaction force and energy, respectively, one can demonstrate that the electrostatic forces

are indeed realised as the negative sphere-centred gradients of the interaction energy.

Theorem 2.2.1 *Let $\mathcal{E}_{\text{int}}^{\ell_{\max}}$ denote the approximate interaction energy and $\mathcal{F}_i^{\ell_{\max}}$, denote the approximate electrostatic force acting on the dielectric particle Ω_i as given by Definitions (2.27) and (2.24) respectively. Then it holds that*

$$-\nabla_{\mathbf{x}_i} \mathcal{E}_{\text{int}}^{\ell_{\max}} = \mathcal{F}_i^{\ell_{\max}}, \tag{2.26}$$

where $\nabla_{\mathbf{x}_i}$ denotes the gradient taken with respect to the location of the centre $\mathbf{x}_i$ of the sphere $\partial\Omega_i$.

The proof of Theorem 2.2.1 can be found in appendix A.2. It is important to emphasise that in this form

$$\mathcal{E}_{\text{int}}^{\ell_{\max}} := \frac{1}{2} \sum_{j=1}^{N} \left(\sigma_{s,j} + \sigma_{p,j}, \lambda_{\ell_{\max}} - \lambda_{\ell_{\max}}^{jj} \right)_{L^2(\partial\Omega_j)} + \frac{1}{2} \left(\sigma_{\text{ext}}, \lambda_{\ell_{\max}} \right)_{L^2(\partial\Omega)}$$
$$+ \left(\sigma_s + \sigma_p, \lambda_{\text{ext}}^{\ell_{\max}} \right)_{L^2(\partial\Omega)} + \frac{1}{2} \left(\sigma_{\text{ext}}, \lambda_{\text{ext}}^{\ell_{\max}} \right)_{L^2(\partial\Omega)}, \tag{2.27}$$

$\mathcal{E}_{\text{int}}^{\ell_{\max}}$ includes both the energy due to the interaction between the dielectric particles themselves as well as the energy arising from the interaction of particles with the external electric field.

Also, equation (2.27) has an interpretation in terms of the *total* and *self* electrostatic energies. The combination of the first three terms in equation (2.27) can be interpreted as the *total* electrostatic energy of the system whilst the fourth term can be seen as the *self* electrostatic energy of the system. It should be emphasised that, due to the presence of the point-charge contribution σ_p, both the total energy and the self-energies are infinite as in the case of fixed Coulomb point-charges. However, when writing the interaction energy as in equation (2.27) each of the terms is finite and thus the interaction energy is a well-defined quantity.

Finally, it is possible to re-write Equation (2.27) for the electrostatic interaction energy in a more physically intuitive form in terms of the electric fields that appear in the PDE formulations (2.3) and (2.4) leading to the following theorem.

Theorem 2.2.2 *Let λ_{ext} denote the restriction of Φ_{ext} to $\partial\Omega$, and let λ denote the solution to the boundary integral equation (2.6) for a given free charge $\sigma_f = \sigma_s + \sigma_p$ and external electric field $\mathbf{E}_{\text{ext}}$. Then for any open ball $\mathbb{B}_r$ of radius $r > 0$ which is large enough to contain Ω^-, the exact electrostatic interaction energy of the system, denoted $\mathcal{E}_{\text{int}}$, satisfies the relation*

$$\mathcal{E}_{\text{int}} := \frac{1}{2}\big(\sigma_s + \sigma_p + \sigma_{\text{ext}},\ \lambda\big)_{L^2(\partial\Omega)} + \big(\sigma_s + \sigma_p,\ \lambda_{\text{ext}}\big)_{L^2(\partial\Omega)}$$

$$+ \frac{1}{2}\big(\sigma_{\text{ext}},\ \lambda_{\text{ext}}\big)_{L^2(\partial\Omega)} - \frac{1}{2}\sum_{j=1}^{N}\big(\sigma_{s,j} + \sigma_{p,j}, \lambda^{jj}\big)_{L^2(\partial\Omega_j)}$$

$$(2.28)$$

$$= \frac{1}{2}\int_{\mathbb{B}_r}\kappa(\mathbf{x})\mathbf{E}_{\text{tot}}(\mathbf{x})\cdot\mathbf{E}_{\text{tot}}(\mathbf{x})\,d\mathbf{x} - \frac{1}{2}\sum_{j=1}^{N}\int_{\mathbb{B}_r}\kappa(\mathbf{x})\mathbf{E}^{jj}(\mathbf{x})\cdot\mathbf{E}^{jj}(\mathbf{x})\,d\mathbf{x}$$

$$- \frac{1}{2}\int_{\mathbb{B}_r}\kappa_0\mathbf{E}_{\text{ext}}(\mathbf{x})\cdot\mathbf{E}_{\text{ext}}(\mathbf{x})\,d\mathbf{x} + \frac{1}{2}\int_{\partial\mathbb{B}_r}\kappa_0\left(\mathbf{E}(\mathbf{x})\cdot\eta(\mathbf{x})\,\Phi(\mathbf{x})\right)$$

$$- \sum_{j=1}^{N}\mathbf{E}^{jj}(\mathbf{x})\cdot\eta(\mathbf{x})\,\Phi^{jj}(\mathbf{x})\big)\,d\mathbf{x} + \int_{\partial\mathbb{B}_r}\kappa_0\mathbf{E}(\mathbf{x})\cdot\eta(\mathbf{x})\,\Phi_{\text{ext}}(\mathbf{x})\,d\mathbf{x}. \quad (2.29)$$

Here, λ^{jj} is the exact self-potential only on sphere $\partial\Omega_j$ in the absence of an external field $\mathbf{E}_{\text{ext}}$ and all other spheres, and it is defined as the solution to the local BIE

$$\lambda^{jj} - \mathcal{V}_j\text{DtN}_j\left(\frac{\kappa_0 - \kappa_j}{\kappa_0}\lambda^{jj}\right) = \frac{1}{\kappa_0}\mathcal{V}_j\big(\sigma_{s,j} + \sigma_{p,j}\big).$$

Moreover, $\mathbf{E}^{jj}$ and Φ^{jj} are the "self electric field" and "self electrostatic potential" respectively of the j-th dielectric particle, i.e., the electric field and potential respectively produced only due to sphere $\partial\Omega_j$ in the absence of both

the external field $\mathbf{E}_{\text{ext}}$ as well as the other spheres. The proof of Theorem 2.2.2 can be found in appendix A.2.

The five terms in Equation (2.29) which constitute $\mathcal{E}_{\text{int}}$ all have physical interpretations. The first integral can be understood as the total electrostatic energy associated with an electric field $\mathbf{E}_{\text{tot}}$. The second integral can be interpreted as the self-energy associated with the free charge $\sigma_f = \sigma_s + \sigma_p$ on the particle surface, whilst the third term is the self energy of the external electric field $\mathbf{E}_{\text{ext}}$. Finally, the last two terms can be interpreted as the boundary terms that, in general, may not vanish at infinity but yield an expression independent of the positions of the particles. Theorem 2.2.2 establishes that in the exact case, i.e. when the discretisation parameter $\ell_{\max} \to \infty$, the definition of the interaction energy, derived from the integral equation formalism and given by Equation (2.27), coincides with the definition of the interaction energy (up to some additional boundary terms) in any open ball $\mathbb{B}_r$ that is large enough to contain Ω^- as derived from the PDE picture and given through Equation (2.29).

Considering once again Equation (2.24) that defines the net electrostatic force acting on dielectric particle Ω_i, it is possible that one could be interested only in a portion of this electrostatic force *without* the so-called 'self-force'. The 'self-force' is the force that acts on the dielectric particle Ω_i in the absence of all other interacting particles but *still* in the presence of the external field $\mathbf{E}_{\text{ext}}$, i.e., the force that would act on the particle if it were the only one exposed to the external field. Mathematically, this new approximate net electrostatic force acting on the dielectric particle Ω_i, $i \in \{1, \ldots, N\}$ is given by

$$\widehat{\mathcal{F}}_i^{\ell_{\max}} := \kappa_0 \left(\nu_{\ell_{\max}}, \mathbf{E}_{\text{exc}}^i + \mathbf{E}_{\text{ext}} \right)_{L^2(\partial\Omega_i)} - \kappa_0 \left(\widehat{\nu}_{\ell_{\max}}^{ii}, \mathbf{E}_{\text{ext}} \right)_{L^2(\partial\Omega_i)}, \qquad (2.30)$$

where $\widehat{\nu}_{\ell_{\max}}^{ii}$ is the total surface charge (including polarisation effects) on $\partial\Omega_i$ in the absence of all other interacting particles but in the presence of the external

electric field. Mathematically (c.f., Equation (2.23)),

$$\widehat{\nu}_{\ell_{\max}}^{ii} = \frac{\kappa_0 - \kappa}{\kappa_0} \mathrm{DtN}_i \widehat{\lambda}_{\ell_{\max}}^{ii} + \frac{1}{\kappa_0} \left(\sigma_{s,i}^{\ell_{\max}} + \sigma_{p,i}^{\ell_{\max}} + \sigma_{\mathsf{ext},i}^{\ell_{\max}} \right),$$

where $\widehat{\lambda}_{\ell_{\max}}^{ii}$ is the solution to the local Galerkin discretisation

$$\left(\widehat{\lambda}_{\ell_{\max}}^{ii} - \mathcal{V}_i \mathrm{DtN}_i \left(\frac{\kappa_0 - \kappa}{\kappa_0} \widehat{\lambda}_{\ell_{\max}}^{ii} \right), \psi_{\ell_{\max}}^{ii} \right)_{L^2(\partial\Omega_i)}$$

$$= \left(\frac{1}{\kappa_0} \mathcal{V}_i \left(\sigma_{s,i} + \sigma_{p,i} + \sigma_{\mathsf{ext},i} \right), \psi_{\ell_{\max}}^{ii} \right)_{L^2(\partial\Omega_i)}.$$

Corresponding to the approximate net electrostatic force given by Equation (2.30), we have the following approximate interaction energy

$$\widehat{\mathcal{E}}_{\mathsf{int}}^{\ell_{\max}} := \frac{1}{2} \left(\sigma_s + \sigma_p + \sigma_{\mathsf{ext}}, \ \lambda_{\ell_{\max}} \right)_{L^2(\partial\Omega)} - \frac{1}{2} \sum_{j=1}^{N} \left(\sigma_{s,j} + \sigma_{p,j} + \sigma_{\mathsf{ext},j}, \widehat{\lambda}_{\ell_{\max}}^{jj} \right)_{L^2(\partial\Omega_j)}.$$

$$(2.31)$$

The force (2.30) subtracts the force that each single particle would be exposed to due to the external field in absence of the other particles, from the net force on the particle. The corresponding energy expression (2.31) is then such that the force (2.30) equals minus the sphere-centreed gradients of the energy (2.31) following similar arguments as used in the proof of Theorem 2.2.1.

2.3 Physical Applicability of the Framework

A bench-marking of the methodology developed in section 2.2 is required in order to justify the framework's physical applicability. Initially, the effects of an external electric field acting on a single particle will be tested, before increasing the complexity to two and three particles sequentially.

2.3.1 Single Particle Physical Applicability

A charged, smooth, spherical, dielectric particle possesses equal surface charge density (uniformly spread) over its surface in the absence of any external perturbations as a result of Gauss's law. Given the decomposition of the surface charge shown in equation 2.1, the polarisation of a dielectric particle due to an external electric field is bench-marked for a neutral particle exposed to increasing external electric fields by comparison to classical methodologies describing isolated particles in such environments.

Stone [52] shows that under the presence of an external electric field, a neutral particle will gain a dipole of the form

$$\mathbf{p} := 4\pi\epsilon_0 \frac{\epsilon - 1}{\epsilon + 2} r^3 \mathbf{E}_{\text{ext}}, \tag{2.32}$$

where r is the particle radius, ϵ_0 is the permittivity of free space, and ϵ is the relative dielectric permittivity of the particle with respect to the medium ($\epsilon = \kappa/\kappa_0$). The dipole (as in equation 2.32) can be represented by the surface charge distribution as

$$\sigma_{\text{ext}} = 3\epsilon_0 \frac{\epsilon - 1}{\epsilon + 2} \cos(\alpha) \mathbf{E_{ext}} \tag{2.33}$$

where α is the angle as defined in figure 2.1. A charged particle would also experience a force acting in the direction of the applied field, [52] and, in the case of an inhomogeneous distribution of free surface charge, the particle will rotate to minimise the interaction energy with the field.[10]

Due to the opposing force acting on positive and negative charges in the presence of an electric field, a neutral particle as shown in figure 2.1a would gain a sinusoidal surface charge as predicted by Stone [52] via equation 2.33, whilst not undergoing a net force. The calculations presented in figure 2.1b are in complete agreement with Stone in the convergent regime for an isolated par-
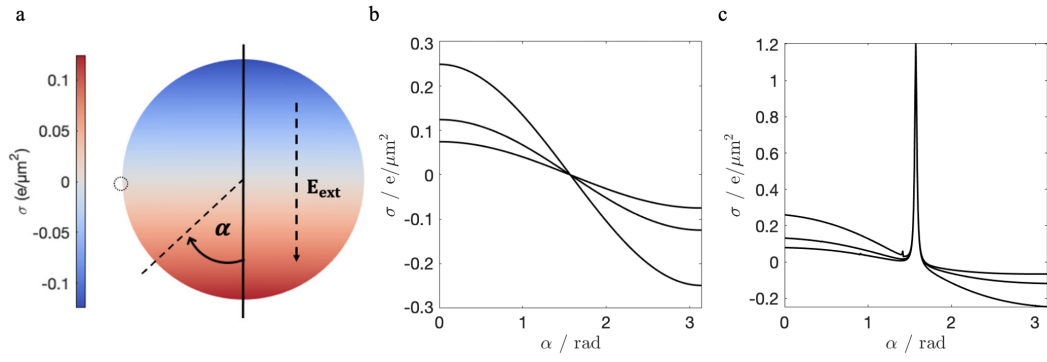
Figure 2.1: *a) Surface charge density on a neutral dielectric particle ($\kappa = 10, r = 5\mu m$) placed in an external electrical field of $|\mathbf{E_{ext}}| = 1000$ V/m; b) Surface charge density on the neutral particle (a) calculated at different external electrical field strengths: $|\mathbf{E_{ext}}| = 600$ V/m, 1000 V/m, and 2000 V/m; c) Surface charge density on the particle (a) with a model surface point charge of 0.2e placed at $\alpha = \pi/2$, as indicated by a small dotted circle.*

ticle.

Upon the introduction of a point charge to the surface of the neutral particle, as discussed previously, the direction of the electric field relative to the point charge on the sphere has to be carefully considered. Here, we consider the case of a point charge placed at $\alpha = \pi/2$, as shown in figure 2.1a by the dotted circle. Although this configuration could be considered the most unstable due to the fact it would have maximal rotational force and equal translation forces compared to other configurations of the surface charge in an external field, in the presence of an external field the cost of calculating the surface charge distribution in this case is much lower due to the absence of charge on the equator of the particle in figure 2.1a. As such, this is the case primarily discussed throughout this text.

As expected, the surface charge distribution of a particle with a point charge on the surface perpendicularly to the field (geometry illustrated in figure 2.1a and surface charge distribution shown in figure 2.1c) is analogous to the surface charge distribution shown in figure 2.1b, when $\alpha \neq \pi/2$. However, when $\alpha \to \pi/2$ the surface charge density reaches a maximum in a fashion similar to that of the dirac-delta function. This is due to the sinusoidal nature of the polarisation of a neutral sphere via a uniform external field (shown in equation

2.33) as $\cos\alpha = 0$ at $\alpha = \pi/2$. At critically low values of external electric field size or dielectric permittivity, some competition may occur between the self-polarization of the particle due to the point charge and the nodal behaviour of the external field polarization, but we observe no such competition given the field's strength considered in figure 2.1.

Although the width of the maxima at $\alpha = \pi/2$ should ideally be infinitesimally small to accurately describe a point charge (or at least (sub-)atomic in size), it does not appear as such in figure 2.1. This is due to the truncation of ℓ_{max} to a finite value in the second term of equation 2.29 given the overall dependence of equation 2.13 on ℓ_{max}. Therefore, the width of the maximum narrows and grows larger in amplitude as ℓ_{max} increases.

2.3.2   Two-Body Physical Applicability

As a neutral, isolated, dielectric particle will gain a dipolar surface charge that is independent of the particles' location (due to the uniform nature of the field), two interacting particles in a uniform external electric field can be treated as two interacting dipoles ($\mathbf{p_1}$ and $\mathbf{p_2}$) at some centre-to-centre separation R, the interaction energy of which is defined as

$$\mathcal{E}_{\text{int}}(\mathbf{p_1}, \mathbf{p_2}) = \frac{R^2(\mathbf{p_1} \cdot \mathbf{p_2}) - 3(\mathbf{p_1} \cdot \mathbf{R})(\mathbf{p_2} \cdot \mathbf{R})}{4\pi\epsilon_0\kappa_0 R^5}, \tag{2.34}$$

However, it is convenient to express the direction of the dipoles $\mathbf{p_1}$ and $\mathbf{p_2}$ with respect to the vector $\mathbf{R}$ using polar coordinates such that

$$\mathbf{p_i} \cdot \mathbf{R} = p_i R \cos(\theta_i) \tag{2.35}$$

and

$$\mathbf{p_1} \cdot \mathbf{p_2} = p_1 p_2 (\cos\theta_1 \cos\theta_2 + \sin\theta_1 \sin\theta_2 \cos(\varphi_2 - \varphi_1)). \tag{2.36}$$

from which, $\mathcal{E}_{\text{int}}$ can be rewritten as

$$\mathcal{E}_{\text{int}}(\mathbf{p_1}, \mathbf{p_2}) = -\frac{p_1 p_2}{4\pi\epsilon_0\kappa_0 R^3}(2\cos\theta_1\cos\theta_2 - \sin\theta_1\sin\theta_2\cos(\varphi_2 - \varphi_1)) \quad (2.37)$$

where θ_i is the angle of the dipole with respect to the axis $\mathbf{R}$, whilst φ is the angle the dipole is rotated about the axis $\mathbf{R}$.

This classical result shows the dependence of the interaction energy on the direction of the induced dipoles, and as such shows the interaction energy's dependence on the direction of the external (uniform) electric field. If the particles are aligned along the direction of the electric field (such that the vectors $\mathbf{R}$ and $\mathbf{E_{ext}}$ are parallel), then $\sin\theta_1 = \sin\theta_2 = 0$ and $\cos\theta_1 = \cos\theta_2 = 1$ (or -1), the interaction energy ($\mathcal{E}_{\text{int}}^{\|}$) is negative, and the interaction is attractive. However, in the opposing case when the particles are aligned perpendicularly to the field, i.e. when $\mathbf{R}$ and $\mathbf{E_{ext}}$ are orthogonal, the interaction energy ($\mathcal{E}_{\text{int}}^{\perp}$) is positive and indicative of a repulsive interaction. As such,

$$\mathcal{E}_{\text{int}}^{\|}(\mathbf{p_1}, \mathbf{p_2}) = -\frac{p_1 p_2}{2\pi\epsilon_0 R^3}, \quad \mathcal{E}_{\text{int}}^{\perp}(\mathbf{p_1}, \mathbf{p_2}) = \frac{p_1 p_2}{4\pi\epsilon_0 R^3}, \quad\quad (2.38)$$

As such, it can be deduced that the classical dipolar interaction energy is of a greater magnitude, but opposing sign, in the attractive case ($\mathcal{E}_{\text{int}}^{\|}$) than the repulsive case ($\mathcal{E}_{\text{int}}^{\perp}$) due to the factor of two inside the bracket in equation 2.37. In both cases, the interaction energy decays as $1/R^3$ and if the field strength is halved, the interaction energy is reduced by a factor of four. However, the classical formalism utilised from Stone's[52] work, as discussed throughout this section thus far, negates the interaction of one particle with another (polarisation), the interaction of which would be expected to heavily influence the resultant surface charge distribution on the particle, and hence the force acting on the particle given equation 2.24.

To account for the polarization of each particle due to the presence of another particle, a formalism such as that derived throughout this chapter is required. However, as the formalism derived throughout section 2.2.3 is reliant on the

truncation of the infinite sum over ℓ_{max} in equation 2.13, a convergent value of ℓ_{max} must be determined such that the interaction can be deemed as physically accurate. This can be achieved graphically by inspection or numerically with a tolerance, both of which are employed throughout this chapter depending on the cost of the computations involved as although this method scales linearly with the number of particles, it scales quadratically with respect to ℓ_{max}, for the evaluation of $\mathcal{E}_{\text{int}}^{\ell_{\max}}$, as in Lindgren's original formalism.[58]
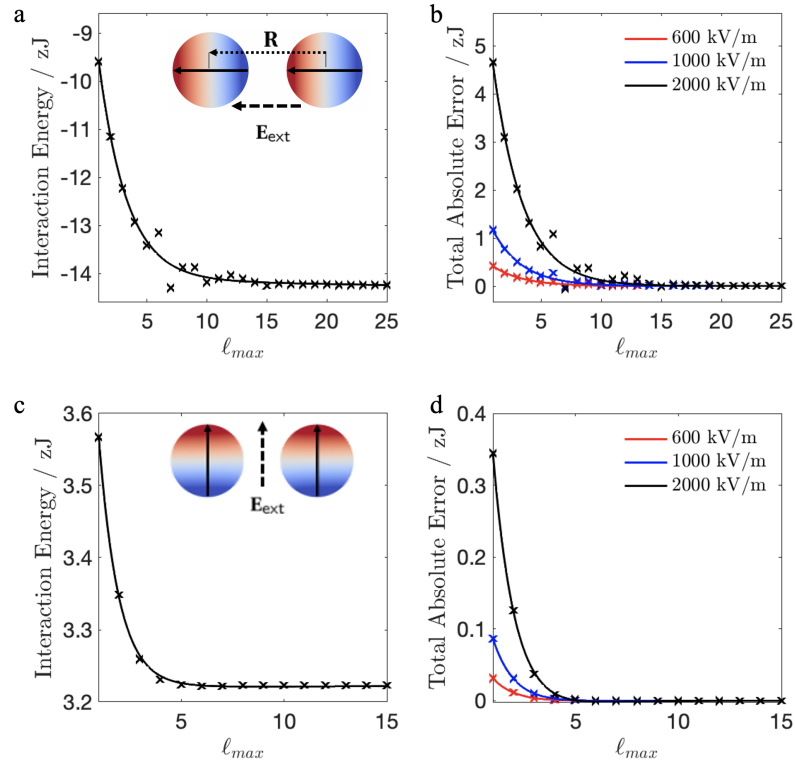
Figure 2.2: *The interaction energy and the error in the interaction energy as a function of ℓ_{max} to determine the convergence; the interaction energy as a function of ℓ_{max} for two particles where $\boldsymbol{R}$ is parallel to $\boldsymbol{E}_{ext}$ in an electrical field of 2000 kV/m as shown in the inset (a), the total absolute error in the calculation of the system depicted in the inset of a for external electrical fields of 600, 1000, and 2000 kV/m (b), the interaction energy as a function of ℓ_{max} for two particles where $\boldsymbol{R}$ is orthogonal to $\boldsymbol{E}_{ext}$ in an electrical field of 2000 kV/m as shown in the inset (c), the total absolute error in the calculation of the system depicted in the inset of c for external electrical fields of 600, 1000, and 2000 kV/m (d). The particles simulated have a dielectric constant of 10, in a vacuum ($\kappa_0 = 0$), with a radius of 5 μm at 0.01 μm surface-to-surface separation.*

Figure 2.2 shows the variation in the accuracy of the formalism presented throughout this section for a given ℓ_{max} in various electrical fields, for the cases of maximum repulsion and attraction, utilising the interaction energy of

the system to assess the accuracy. Whilst the surface charge distribution can also indicate convergence of equation 2.13 via its *smoothness*, the interaction energy is used in this capacity throughout for both simplicity and its physical importance in the analysis/evaluation. An interaction energy deemed to be accurate ($\ell_{max} = 30$) was used as a benchmark to calculate the total absolute error of the system.

It can be seen from figure 2.2a that the interaction energy has converged for the case of two dielectric particles in an external electric field parallel to $\mathbf{R}$ of 2000 V/m in size when $\ell_{max} = 25$, and $\ell_{max} = 15$ if R is orthogonal to $\mathbf{E}_{ext}$. These parameters were chosen given an at least 1% error from the previous point. This difference in the rate of convergence can be physically justified as a consequence of the increased separation between the areas of highest surface charge in the orthogonal case compared to the parallel case, as illustrated via the insets in figures 2.2a and c.

As the magnitude of the external electric field is increased, higher values of ℓ_{max} are required to achieve convergence as shown by figures 2.2b and d. This is due to the increased quantity of charge at the poles of the particles in increasing electric fields causing the polarization on the neighbouring particle to be much greater. As such, the degree of the spherical harmonics required to describe the polarization increases with electric field size.

Given a convergent and computationally affordable regime, $\ell_{max} = 35$, the interaction energy as a function of surface-to-surface separation can be calculated for the systems depicted in the insets figure 2.2a and c. As such, the interaction energy as a function of separation can be determined, as shown in figure 2.3 alongside the interaction of two dipoles, the size of which are determined using equation 2.32.

The results shown in figure 2.3 show that in the case of attraction, the interaction energy between particles can be twice as large as that predicted by the approximation of fixed dipoles (2.37). Consequently, at short separation distances, a quantitatively accurate account of the interaction energy (and the
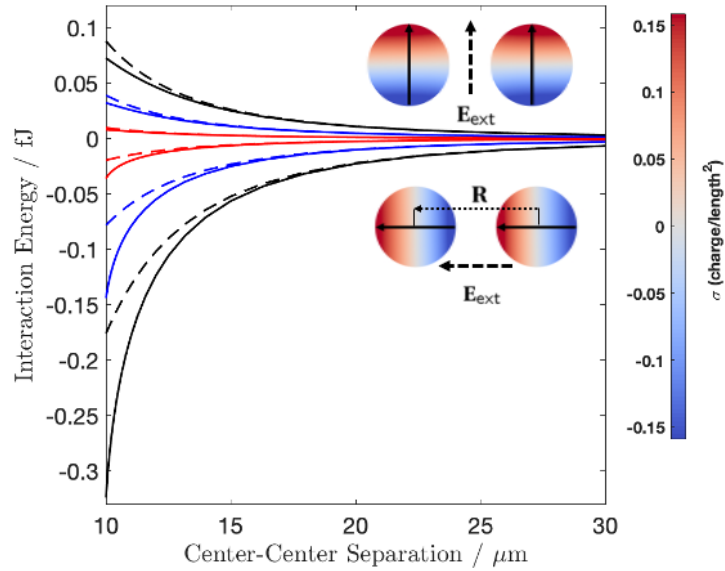
Figure 2.3: *The interaction energy between two neutral dielectric particles ($r_1 = r_2 = 5~\mu m$ and $\kappa_1 = \kappa_2 = 10$) in an applied electric field as a function of the separation distance. Dashed line: approximation of two fixed dipoles as defined by Equation (2.37); solid line: calculation using Equation (2.27) taking into account the separation-dependent particle polarisation. The strength of the applied electric field is 100 kV/m (red), 200 kV/m (blue) and 300 kV/m (black). The interaction takes place in vacuum, i.e. $\kappa_0 = 1$.*

force) can only be achieved through a realistic description of surface charge polarisation, i.e a description beyond the induced dipole $\ell_{\max} = 1$ approxima-tion as we describe here, where in the case of Figure 2, $\ell_{\max} = 30$ with 1454 Lebedev integration points used.
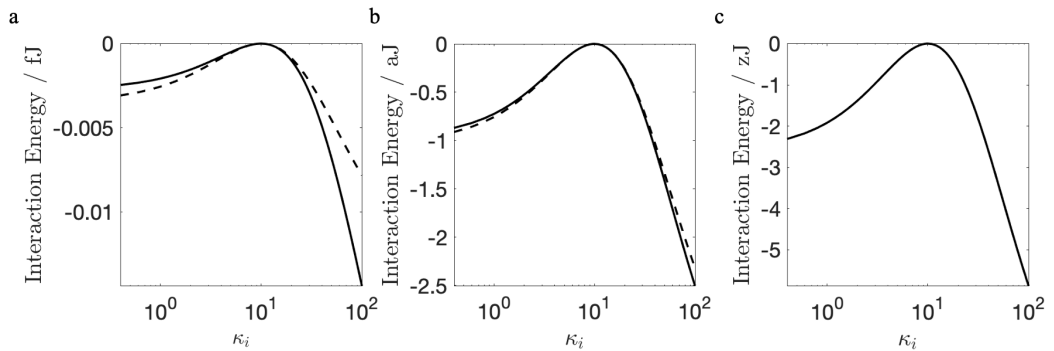
Figure 2.4: *The interaction energy between two neutral particles ($r_1 = r_2 = 5~\mu m$) in an external electric field of 200 kV/m as a function of their dielectric constant. Dashed line: approximation of two fixed dipoles as defined by Equation (2.37); solid line: calculation using Equation (2.27). The surface-to-surface separation distance is $10^{-3}~\mu m$ (a), $5~\mu m$ (b), $100~\mu m$ (c). The interaction takes place in a medium with $\kappa_0 = 10$. Note change of scale along the y-axis.*

The nature of the attraction at short separations is also critically influenced

by the polarisation of the medium, as shown in Figures 2.4 and 2.5. When the dielectric constant of the medium κ_0 is greater than that of the particles κ_i, shielding by the medium reduces the strength of the attractive interaction between particles. Figure 2.4a shows the most pronounced case of such a shielding effect at $10^{-3}\mu m$ surface-to-surface separation. At a large separation, as shown in Figure 2.4c, the shielding effect becomes negligible. When $\kappa_0 < \kappa_i$, the interaction is much stronger when particle polarisation is taken into account, as confirmed in Figures 2.4a and 2.5a, and also in Figure 2.3. Figure 2.5 supplements these observations with calculations of the inter-particle interaction energy for a large range of values of the dielectric constant of the medium - from 1 (vacuum) to 100. The simulations in both Figure 2.4 and 2.5 required spherical harmonics of the 30th degree (i.e., $\ell_{\max} = 30$) with 1454 Lebedev integration points for the evaluation of equation 2.31.
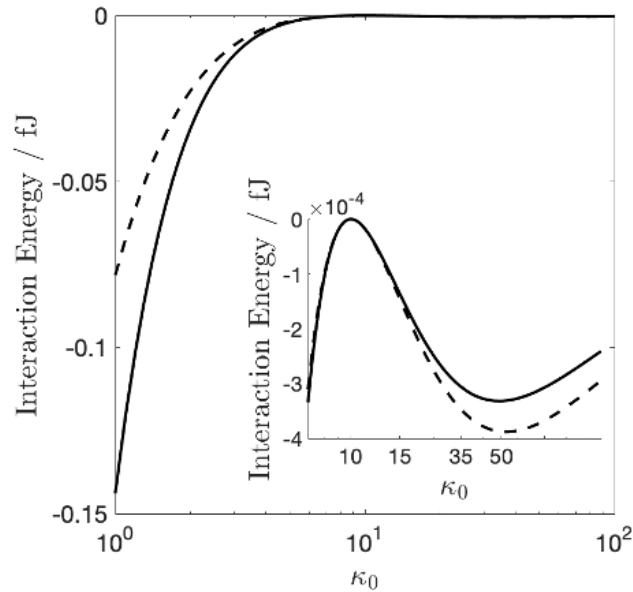
Figure 2.5: *The interaction energy between two neutral particles ($r_1 = r_2 = 5\ \mu m$ and $\kappa_1 = \kappa_2 = 10$) in an external electric field of 200 kV/m as a function of the dielectric constant of medium: a) κ_0 ranging from 1 (vacuum) to 100; b) expansion of the region for κ_0 values between 10 and 45, highlighting minor extrema. Dashed line: approximation of two fixed dipoles as defined by Equation (2.37); solid line: calculation using Equation (2.27). The surface-to-surface separation is $10^{-3}\ \mu m$.*

The special case of a neutral surface containing a point charge has been discussed in Filippov *et al*, [50] where the four extreme orientations of two point surface charges were considered in several different chemical scenarios; this

work[50] is in excellent agreement with the method presented here. For the general case κ_i κ_0, the orientation of the particles shown in Figure 2.6 is the most attractive scenario in the absence of an external electric field. Furthermore, an inhomogeneous surface charge distribution, such as a point charge placed on a neutral sphere, breaks the axial symmetry (except for a few specific cases) thus presenting a more complex system.
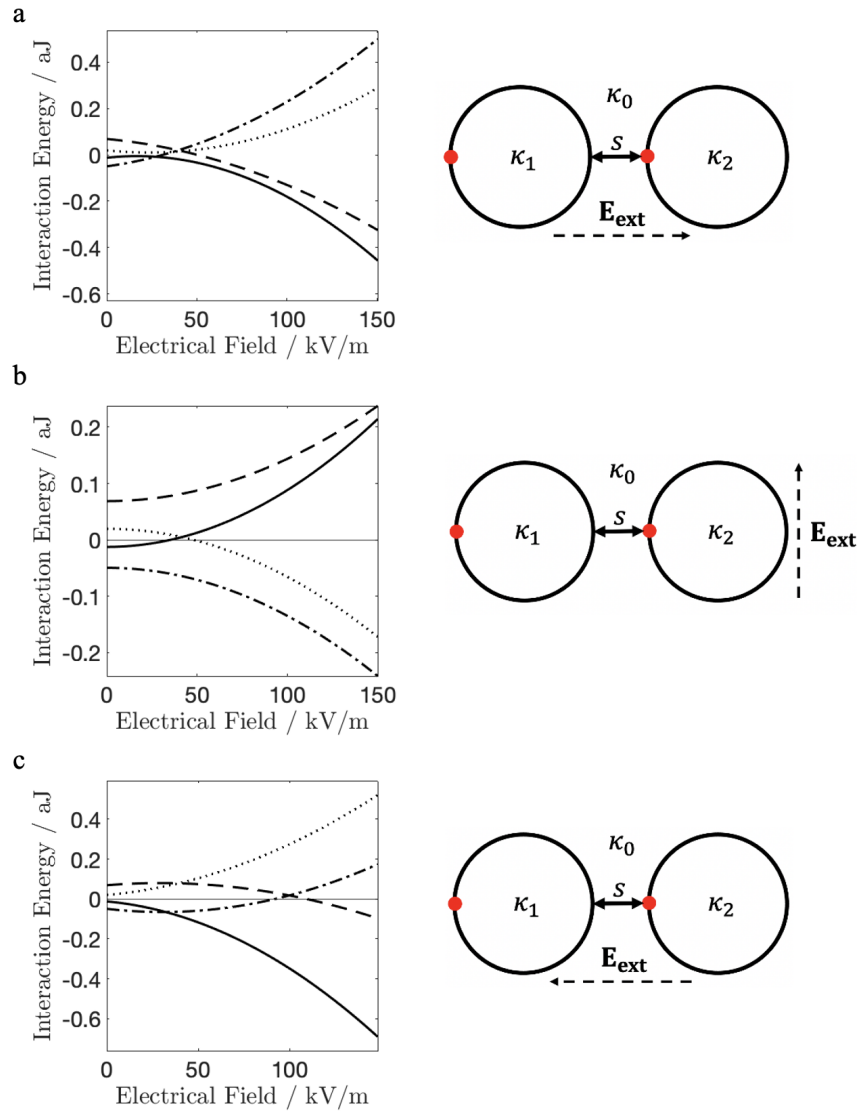
Figure 2.6: *The interaction energy between two dielectric particles ($r_1 = r_2 = 5\mu m$) containing a surface point charge of 50e as a function of the strength of the applied external field: $\kappa_1 = \kappa_2 = 20$ (solid line), $\kappa_1 = \kappa_2 = 5$ (dashed line), $\kappa_1 = 20$ and $\kappa_2 = 5$ (dotted line), and $\kappa_1 = 5$ and $\kappa_2 = 20$ (dot-dashed line). The interaction takes place in a dielectric medium with $\kappa_0 = 10$ at the surface-to-surface separation of $10^{-3}\mu m$. Illustrations alongside each graph show the orientation of the external electric field: parallel with (a and c) and perpendicular to (b) the alignment of the interacting particles.*

As illustrated in Figure 2.3, the interaction between two particles in the presence of an external electric field has a strong directional dependence. If the strength of the applied electric field is high, the interaction between particles containing surface point charge follows the trends seen in Figure 2.3. In this case, the dominant contribution to the interaction energy/force comes from a field-induced dipole-dipole interaction. When both particles have the same dielectric constant (solid and dashed lines in Figures 2.6a-and c), a strong attractive interaction occurs when the field is acting parallel to particle alignment (Figures 2.6a; $\theta = 0$ and 2.6c; $\theta = \pi$); however, if $\kappa_0 > \kappa_i$ (dashed line) the dipole-dipole interaction is reduced due to the medium shielding effect. In Figure 2.6b where the applied field acts in the direction perpendicular to particle alignment ($\theta = \pi/2$), the interaction is driven by the repulsive dipole-dipole interaction.
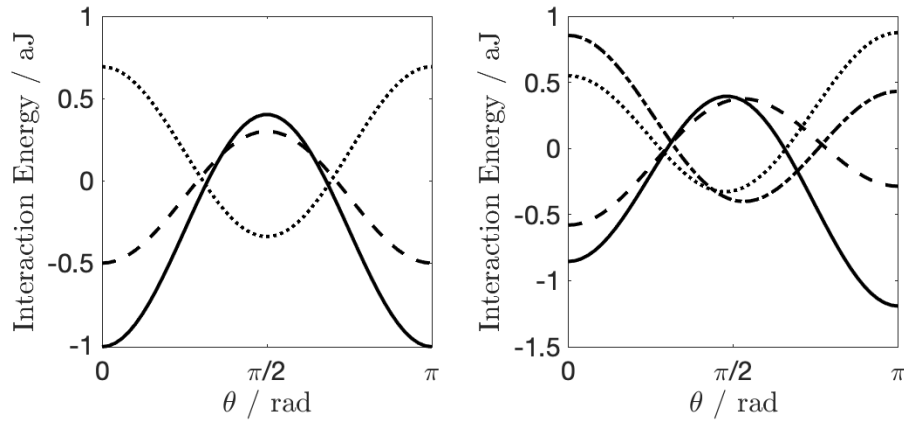
Figure 2.7: *The interaction energy between two particles ($r_1 = r_2 = 5 \ \mu m$) in an external electric field of 200 kV/m as a function of the angle of the field rotation: left) neutral dielectric particles; right) dielectric particles with a point surface charge of 50e, as shown in Figure 2.6. Dashed line: $\kappa_1 = \kappa_2 = 5$; solid line: $\kappa_1 = \kappa_2 = 20$; dot-dashed line: $\kappa_1 = 20$, $\kappa_2 = 5$; dotted line: $\kappa_1 = 5, \kappa_2 = 20$. The interaction takes place in a medium with $\kappa_0 = 10$ at the surface-to-surface separation of 10^{-3} μm. Note that in the case of uniform surface charge distribution (a) the cases of $\kappa_1 = 20$, $\kappa_2 = 5$ and $\kappa_1 = 5$, $\kappa_2 = 20$ are identical.*

If $\kappa_1 < \kappa_0 < \kappa_2$ (dot-dashed lines) or $\kappa_2 < \kappa_0 < \kappa_1$ (dotted lines), the dominant dipole-dipole interaction is repulsive when the field is parallel to particle alignment, and it is attractive when the field is perpendicular to the particle alignment as in the latter case the dipoles point in opposite directions. At

smaller magnitude of applied electric field, an additional contribution to the interaction energy from the surface point charges becomes significant leading to more subtle effects. The strength of the interaction in this case is governed by the total surface charge represented by fixed point charges and induced surface charge. This behaviour can be understood through Equation (2.27) by realising that $\sigma_p^{\ell_{\max}} \geqslant \sigma_{\text{ext}}^{\ell_{\max}}$ for weak external fields and $\sigma_p^{\ell_{\max}} \leqslant \sigma_{\text{ext}}^{\ell_{\max}}$ for strong external fields. However, as these studies refer to charged particles, the interaction energies in both Figures 2.6 and 2.7 are calculated via the evaluation of Equation (2.31) in order to only study the interaction of the particles with one another.

With the addition of a point charge to the surface of each particle, the interaction energy described by Equation (2.27) is again driven by the total surface charge density having both $\sigma_{\text{ext}}^{\ell_{\max}}$ and $\sigma_p^{\ell_{\max}}$ components. For the case of $\kappa_1 = \kappa_2 = 20$, polarisation due to the point charge leads to a more attractive interaction at $\theta = \pi$ where the total surface charge at $10^{-3}\mu m$ surface-to-surface separation (s) increases due to the applied field; the interaction is less attractive at $\theta = 0$ as the total charge at the closest s decreases due to the field. The same reasoning can be applied to the case of $\kappa_1 = \kappa_2 < \kappa_0$ but with the opposite overall effect. Similarly, in the case of $\kappa_1 < \kappa_0 < \kappa_2$, the general shape can be attributed to the effects captured in Figure 2.7 (left) for neutral particles. The deviation in the interaction energy at $\theta = 0$ and $\theta = \pi$ for the cases where $\kappa_2 \neq \kappa_1$ is due to the polarisation caused by the point charge on the surface of the neighbouring particle.

In conclusion, the results presented in Figures 2.3 - 2.7 agree with the classical picture of interaction between two fixed-size dipoles, whilst showing variations in the strength of such interaction due to particle polarisation, which are substantial when the inter-particle separation is comparable to the size of the particles. A quantitative description of charged particles with inhomogenous surface charge distributions interacting in an external electric field can be obtained readily using the formalism presented in Section 2.2.4.

2.3.3 Three-Body Physical Applicability

Given the difficulties that arise upon trying to calculate the effect of three bodies interacting, test cases are formulated to understand the effect of polarization on such systems.

Filippov *et al* [50] showed that two particles with a surface charge distribution including a point charge could attract one another, even if the point charges are of the same sign due to the polarization such a concentrated charge causes for certain linear arrangements of particles.

Given an accurate many-body formalism, such studies can be extended to determine the forces acting on longer ($N = 3$) linear arrangements of particles possessing a point charge of their surface. Although, the particles would also undergo a torque in response to several of the orientations investigated, only the net force acting on the particle is considered here.

Figure 2.8a illustrates the geometric arrangement of three particles in a chain and defines the variable describing orientation of the central smaller particle in the chain, as studied in figure 2.8b. Given the findings of Filippov *et al*, it is expected that upon alignment of the point charge on the central sphere with either of the two outer particles charge-axis, the particle will undergo a maximum force in the direction of the point charges nearest neighbour ($\mathbf{F}_{||}$) due to this position inducing the maximum polarisation between the particles. Given such an orientation, there would also be zero force acting in the direction perpendicular to the alignment of the particles ($\mathbf{F}_{\perp}$). This was observed throughout our simulations, as seen in figure 2.8b.

Given the symmetry of the system, it would also be expected that when the point charge is placed directly atop the central particle in the chain ($\theta = \pi/2$), $\mathbf{F}_{||} = 0$. This is due to the fact that both particles provide an equal force component parallel to the direction of alignment, but in opposite directions, hence cancelling each other out. The framework presented in this section agrees well with this physical justification, as can be seen by the local maxima at θ

a

b
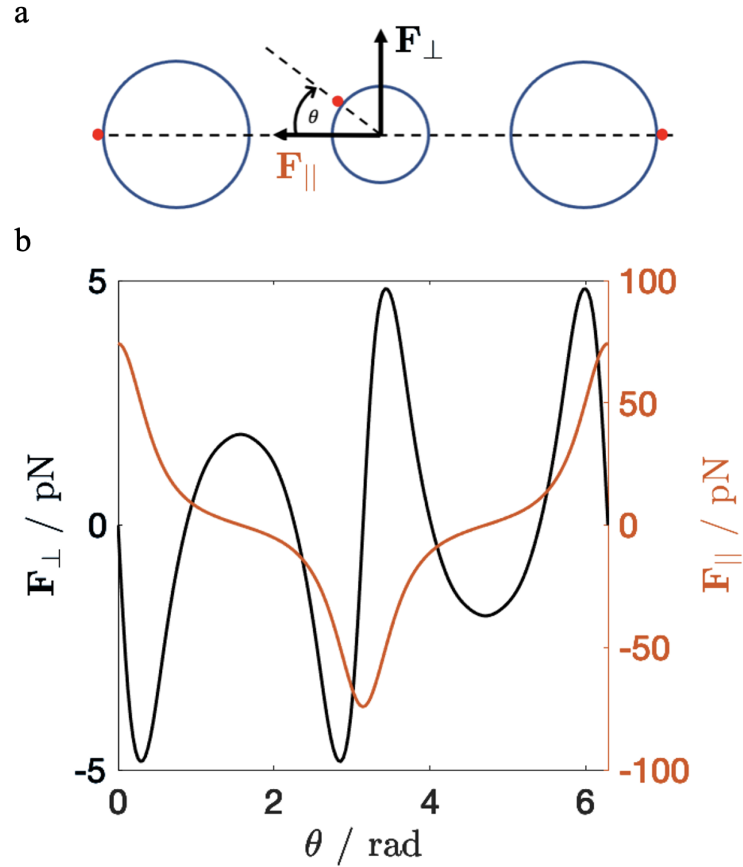
Figure 2.8: *An investigation of the force acting on the central particle, parallel (orange) and perpendicularly (black) to the point charge alignment. The particles have radii of 0.8, 0.5 and 0.8 nm from left to right and are placed at 0.1 nm surface-to-surface separation, with a point charge of 1e placed on each of the surfaces with the two larger spheres at opposite orientations. Each particle has a dielectric constant of 37.5 and exists in a vacuum. (a) shows the system under investigation where $\boldsymbol{F}_{||}$ is the force acting parallel to particle alignment, $\boldsymbol{F}_{\perp}$ is the force acting perpendicular to the point charge alignment, whilst θ is the angle from the axis of charge alignment such that $0 \leq \theta \geq 2\pi$. (b) shows the variation of $\boldsymbol{F}_{||}$ and $\boldsymbol{F}_{\perp}$ with θ.*

$= \pi/2$.

The maximum component of the force experienced by the central particle in such a configuration, according to figure 2.8b, does not occur at one of the limiting geometries previously discussed. Due to the maximum polarisation of the system occurring upon alignment of the central point charge with the axis of particle alignment, the maximum force experienced by the particle in either of the directions defined by $\mathbf{F}_{||}$ and $\mathbf{F}_{\perp}$ occurs as $\theta \to 0$ and $\theta \to \pi/2$. This is due to the restoring force of the system attempting to restore the system to its most stable state ($\theta \to 0$ and $\theta \to \pi$ (maximum attraction), as investigated

in the two-body case by Filippov *et al*[50].

2.3.4 Melting ionic colloidal crystals in external electric fields

A better understanding of opposite-charge colloidal interactions could facilitate the controlled production of binary crystals with nanometre sized constituent particles, which will ultimately find applications in advanced photonic materials[59]. Leunissen *et al.* [47] investigated the formation of apolar colloidal crystals consisting of polymethyl methacrylate (PMMA) particles with opposite, dissimilar charges and different sizes suspended in a density matching mixture of cyclohexyl bromide (CHB) and cis-decalin. The particle charge was regulated by the addition of tetrabutyl- ammonium bromide (TBAB) salt, which also controlled the Debye screening length. This electrolyte could act as a screening agent, stabilising the crystal given its large excess-charge. The authors [47] reported that for a broad range of particle sizes and charges, the PMMA particles formed body centred cubic type (Caesium Chloride) crystals, which could be reversibly destabilised by the application of an electric field. The latter behaviour can be explained by calculating the electrostatic force that charged particles experience in an external electric field. A force acting in the direction of the applied field can be understood as a consequence of a surface charge distribution different from that in the absence of the field (see Figure 2.1). When exposed to a sufficiently high electrical field, the dipolar nature of the surface charge distribution leads to repulsion between particles in the plane perpendicular to the direction of the field,[52] behaviour similar to that shown in Figure 2.3.

If the movement of surface charge causes a colloidal crystal to destabilise then the energy required could be of significant practical interest, which would require the evaluation of Equation (2.27), however here we evaluate Equation (2.31). In the subsequent numerical results, the interaction energy between
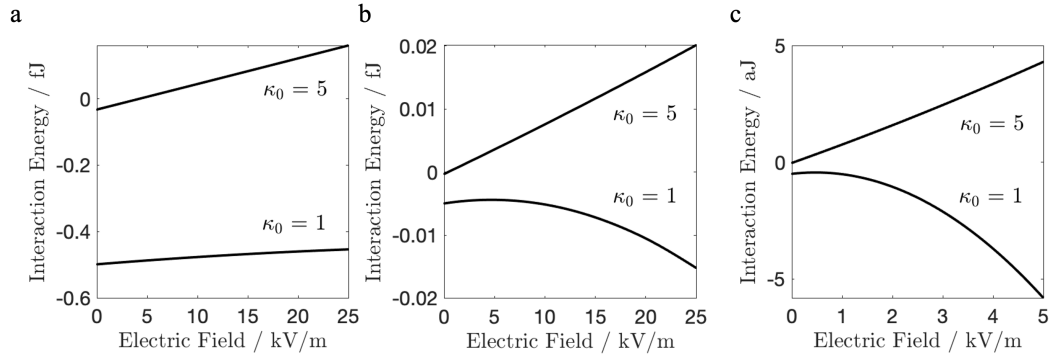
Figure 2.9: *The interaction energy of PMMA colloidal crystal ($\kappa_{PMMA} = 3$, $r_1 = 1.08\ \mu m$, $r_2 = 0.99\ \mu m$, lattice parameter $a_l = 2.4\ \mu m$) as a function of the applied electric field. The PMMA crystal is suspended in vacuum ($\kappa_0 = 1$) and in solvent ($\kappa_0 = 5$). The charge on PMMA particles is $\pm 100e$ (a), $\pm 10e$ (b), $\pm 1e$ (c). In the absence of the external electric field, the interaction energy of the PMMA crystal is small but negative in all three cases.*

particles in the crystal only has the electrostatic component as described in Section 2.2.3. A vanishingly small osmotic pressure, such that the crystals are self-supported by the cohesive energy is also assumed; indeed, these were experimental conditions adopted by Leunissen *et al.*[47]

Figure 2.9 presents the electrostatic energy of a PMMA crystal both in vacuum and in the presence of a solvent. The dielectric constant of the latter ($\kappa_0 = 5$) matches that reported in experiments by Leunissen *et al.* [47] The model crystal used in simulations contains 1024 particles making it smaller than single crystals formed in experiments. Due to the negative value of the electrostatic interaction energy, the PMMA crystals in vacuum are predicted to be stable over a wide range of charge on the constituent particles. An interesting result from the calculations presented is that in vacuum the crystal can be stabilised even further with an increase of the strength of the applied field. This model also predicts that the PMMA crystal is stable in solvents in the absence of the applied electric field, but its structure can be destabilised by application of the field. Therefore, this model implies that if the solvent is more polarisable than the colloidal particles, then the crystal becomes unstable with increasing strength of the external field, as also seen in the experiments reported in Leunissen *et al*, [47] where $\kappa_0 = 5$ was greater than $\kappa_{PMMA} = 3$.

If the external field is switched on, the average electrostatic forces on oppositely charged particles act in opposite directions along the applied field, eventually causing the crystal structure to break apart and melt (see Figure 2.10). A more subtle change in the electrostatic force due to polarisation occurs in directions perpendicular to the applied field. Figure 2.10a exhibits several interesting features, including the value of the field strength at which the average force on a particle in the direction of the applied field is zero and the point at which it crosses forces acting in the two directions perpendicular to the field. As Figure 2.10 shows, in the absence of an external field all three components of the net force on each particle have the same magnitude. At low field strength, the three components of the force are comparable in magnitude, and when the net force in the direction of the field is zero, the crystal particles still experience opposing and equal forces acting in the perpendicular directions (Figures 2.10b,c). Eventually, the direction of the force components parallel to the field change sign and become dominant with a further increase in the field strength, causing displacement of the oppositely charged particles in opposite directions along the field.

Experimental studies [47] have reported observations of PMMA crystal melting through the application of an electrical field. At low values of the field strength, approximately 7 kV/m, a large CsCl-type crystal was found to be generally disordered. However, with the increase of the field strength to about 20 kV/m, lane formation was observed. These findings can be explained using the calculations presented here using spherical harmonics of the 13th degree with 266 Lebedev integration points in a compromise of accuracy for computational cost. Disorder and melting of crystals occurs in the range of electric field values which are greater than the field strength corresponding to zero interaction energy in Figure 2.9 (positive interaction energies indicate unstable structures) but less than the value of the field at which the force components in Figure 2.10a are all equal in magnitude. Lane formation, in which channels of like-charged particles segregate into groups perpendicular to the field, is
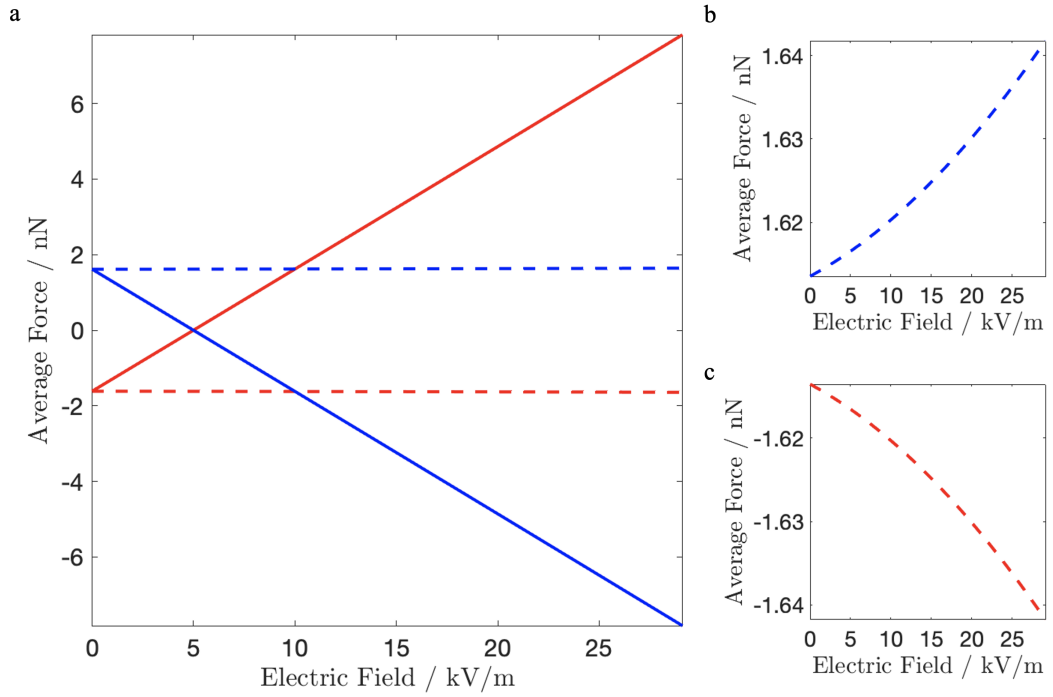
Figure 2.10: *The average force acting on PMMA particles in the crystal ($z_{1,2} = \pm 10e$, $r_1 = 1.08~\mu m$; $r_2 = 0.99~\mu m$) suspended in solvent ($\kappa_0 = 5$): a) in the direction of the applied field (solid lines) and in the directions perpendicular to the field (dashed lines), b) and c) scale up of the forces acting in the directions perpendicular to the field. The force on negative particles is depicted in blue and on positive particles in red.*

observed at much higher fields, exceeding the value at which the force components in Figure 2.10a are equal. In this case, strong average forces acting on each particle, either in the direction of the field (positively charged particles) or anti-parallel to the field (negatively charged particles), cause their spatial separation and lane formation.

2.3.5   Conclusion

Initially, an extension to the framework developed by Lindgren *et al*[49] was derived and implemented in MATLAB. The physical applicability of this framework was then tested against the arguments posed by Lindgren *et al*, general physical justifications, and classical formalisms from throughout the literature.[50, 52] Excellent agreement was found in all comparative test cases, with any deviation found to be physically well justified. The formalism was then applied to qualitatively describe the destabilisation of colloidal crystals within a relatively

highly polarisable medium. Such simulations found good agreement with the experiments of Leunnisen *et al.*, and hence confirmed their findings. Given the novelty of such systems, the presented formalism was used to determine the nature in which such crystals destabilise due to the presence of an electric field for the first time.

Chapter 3

Coalescence of Ice and Dust in the Atmosphere

3.1 Introduction

A significant fraction of the cosmic dust and meteoroid material that hits the Earth remains in the atmosphere for extended periods of time and is a source of solid dust particles, referred to as meteoric smoke particles (MSP) [60, 61]. MSP are formed by an ablation process, whereby meteoroids colliding with atmospheric particles experience strong deceleration and are heated to evaporation temperatures. Meteoric and atmospheric species form an expanding column of partially ionised gas behind the meteoroid, which is observed as a meteor, see e.g. [62]. Part of the meteoroid material vaporises, and the released small solid particles and gaseous species are incorporated into the atmosphere where they grow further to form MSP, see e.g. [60, 63]. The coalescence or condensation mechanisms leading to dust agglomerates is considered to be an important aspect of atmospheric physics and chemistry. A better understanding of these mechanisms could help to establish the significance of particles containing refractory materials that are present in the upper mesosphere and lower thermosphere (MLT), which in short, is the region of 60 to 130 km. These small solid particles could also play a role in the for-

mation of ice clouds by providing a core for heterogeneous condensation that is more effective than homogeneous nucleation. During summer, at high and mid latitudes the temperature near the mesopause reaches a minimum and can fall below the freezing point of water [64], and clouds of ice particles, polar mesospheric clouds (PMC), can form at heights of 80 to 85 km [65]. These are also observed from Earth after sunset and are known as noctilucent clouds (NLC). Because NLC may be an indicator of climate change [66], it is important to understand the possible role of meteoric smoke in the coalescence of ice particles, although the growth of the meteoric smoke is an interesting topic of research in itself.

Models of coagulation [60, 63, 67] take into consideration the convection of dust particles in global atmospheric circulation, the influence of gravitational force, and Brownian motion. The models also assume that particles stick together after a collision, which is not always the case. The outcome can depend on the relative velocity of the colliding particles and the elasticity of a collision as defined by the ratio of the particle speeds after and before the collision (coefficient of restitution), which can vary according to the composition of a particle. Dust charging, which can cause particles to experience either strong attractive or repulsive forces, could also play a role in the growth process. This consideration has not previously been included in modelling the collisional dust growth in the MLT, but has been studied for droplets in tropospheric clouds [68].

In this work, the influence of surface charge on particle agglomeration processes is investigated utilising the formalism developed in chapter 2, alongside statistical mechanics protocols presented by [69] and [50]. These theories predict collision outcomes according to the variables of particle size, charge, dielectric constant, relative kinetic energy, collision geometry and the coefficient of restitution. The presence of negative, positive and neutral particles in the MLT region implies that Coulomb forces between oppositely charged objects are the main attractive component of any electrostatically-driven dust agglomeration

process. However, in addition to the strong attractive interaction between oppositely charged particles, attractive interactions between particles of the same sign of charge can also take place at small separation distances, leading to the formation of stable aggregates. This attractive force is governed by the polarisation of surface charge, leading to regions of negative and positive surface charge density close to the point of contact between colliding particles [21]. The strength of the resulting attractive electrostatic force depends on particle composition as the value of the dielectric constant determines the extent of polarisation of bound surface charge. Previously, the model has successfully explained the effects of like-charge attraction in a range of coalescence processes such as agglomeration of single particles and small clusters derived from a metal oxide composite [70], aerosol growth in the atmosphere of Titan [71] and self-assembly behaviour of charged micro-colloids [72]. Interactions between pairs of neutral and charged particles also depend on the polarisation of surface charge, but these take place in the absence of a Coulomb barrier (see below). In atmospheric science, the method of image charges is routinely used to study collision outcomes if particles can be approximated by conducting spheres (or having the dielectric constant greater than 80). The image charge model can also be applied to study qualitatively the interaction between dielectric particles if the value of the image charge is corrected as $q' = \frac{\epsilon_1 - \epsilon_2}{\epsilon_1 + \epsilon_2} q$, where ϵ_1 and ϵ_2 are the dielectric constants, q' is image charge, and q is real charge. [73] In contrast, quantitatively accurate theoretical studies of interacting dielectric spheres began only quite recently.

The focus of this work is on aggregation processes relevant to mesospheric conditions and in particular at high latitudes. The MLT region offers unique conditions in terms of the electrostatic environment, composition and physical parameters such as temperature and pressure. The pressure at 60 km is less than 100 Pa and decreases further with increasing altitude; therefore, particles interact essentially in vacuum, and, consequently in these simulations, the dielectric constant of the surrounding medium is taken to be one. To investigate

the growth of meteoric smoke particles, both charged and neutral metal oxide particles are considered, with radii ranging from 0.2 nm to 5 nm as shown in Table 3.1. To simulate the growth of ice onto the meteoric smoke, interactions between metal oxide particulates and large ice particles ranging in size from 10 nm to 100 nm and with charges 0 to -5 e are examined. As these particles typically possess a low charge (or a single charge arising, for example, from either a photoionisation event that removes a single electron from a molecule on the particle or the attachment of an ambient ion) the charge distribution is best represented by a point free charge residing on the surface. For this case, the numerical method developed in chapter 2 is utilised to allow for a description of particle charge in the form of point charge(s) residing on its surface, similar to a solution proposed in [50]. Comparisons with a uniform distribution of free surface charge, as described in [69], shows that for particles with radii greater than 10 nm, the choice of a specific form of surface charge distribution does not affect the calculated electrostatic energy between particles; however, the difference does become important for sub-nanometer particles.

Table 3.1: Common particulates found in the MLT region which are considered in this study.

Particle	Dielectric Constant	Density / g/cm^3	Size range / nm	Charge / e
Ice, H_2O	100	0.92	3 - 100	0, -1 to -5
Silicon Dioxide, SiO_2	3.9	2.65	0.2 - 5	0, -1, -2
Magnesium Oxide, MgO	9.6	3.58	0.2 - 5	0, -1, -2
Iron Oxide, FeO	14.2	5.74	0.2 - 5	0, -1, -2

The remaining parts of this chapter are organised as follows. In section 3.2, we describe the ionospheric dusty plasma in the region where we study dust growth. In section 3.3, the range of relative velocities for collisions leading to aggregation is calculated for all collision scenarios that are considered suitable to describe the interactions between ice and dust particles in the mesosphere. These velocity ranges are subsequently used to calculate the percentage aggregation outcome. The orientational geometry of the collisions is discussed,

and a quantitative estimation of the electrostatic interaction energy profile is presented for collisions between like-charged particles. Section 4 focuses on specific cases of aggregation between like-charged dust and ice particles, and section 5 deals with aggregation between small charged dust particulates. A brief discussion of the results is provided separately in section 6.

3.1.1 Aims and Objectives

The aim of this study is to accurately describe the collision mechanics and charge induced polarization between ice and meteoric dust particles in the mesosphere and lower thermosphere. This data will be utilised alongside experimental findings to evaluate the probability of particulate growth in these environments. Factors including particulate size, composition and charge are to be considered.

3.2 Collision Mechanics

Temperatures close to the mesopause at high latitudes fall during summer to the range of 130 K to 150 K, but observational studies have shown this to be variable [64]. Such low temperatures have a significant effect on the nature of water droplets, as according to the appropriate phase diagram [74, 75], ice particles are in a 'soft ice' state and may absorb some of the kinetic energy present during a collision. This possibility has implications for the outcome of all collisions between small metal oxide particulates and ice particles, which at short separation distances can exhibit a strong attraction, even when both particles have a charge of the same sign [69]. However, for like-charged particles with low velocities, this attractive region is largely inaccessible due to the presence of a large repulsive Coulomb energy barrier (E_{Coul}) which prevents their aggregation. In addition to the Coulomb barrier, other factors affect aggregation during a collision; these include the binding energy as defined by the interaction energy at the point of contact (E_0), the coefficient of restitution

(k_r), the Maxwell-Boltzmann distribution of particle velocities at a defined temperature, and the composition of colliding particles (as defined by the dielectric constant and particle density).

The total kinetic energy of a system containing two colliding particles is the sum of the relative kinetic energy with respect to the centre of mass (K_{rel}) and the kinetic energy of the centre of mass (K_{cm})

$$K_{\text{tot}} = \frac{1}{2}\mu v_{\text{rel}}^2 + \frac{1}{2}M v_{\text{cm}}^2 \tag{3.1}$$

where $\mu = \frac{m_1 m_2}{m_1 + m_2}$ is the reduced mass of the colliding particles, $M = m_1 + m_2$, $v_{\text{rel}} = v_1 - v_2$, and $v_{\text{cm}} = \frac{\sum m_j v_j}{M}$ $(j = 1, 2)$. The kinetic energy of the centre of mass is unaffected by changes in the inter-particle interaction energy, but due to the law of conservation of energy, the loss or gain of electrostatic interaction energy between the colliding particles leads to corresponding changes in the relative kinetic energy. At the point where the electrostatic interaction energy is at the maximum (E_{Coul}), the relative kinetic energy of the colliding pair is at the minimum. Once over the barrier and immediately before the collision the kinetic energy is at its highest, i.e. $K_{\text{rel}}^{\text{before}} = K_{\text{rel}}^{\text{initial}} - E_0$, and in an inelastic collision, it is reduced to $K_{\text{rel}}^{\text{after}} = k_r^2 \times K_{\text{rel}}^{\text{before}}$. If $k_r = 1$, the collision is elastic and the kinetic energy does not change during the collision. The minimum relative initial velocity colliding particles require to overcome the Coulomb barrier is therefore

$$v_{\text{rel}}^{\text{min}} = \sqrt{\frac{2E_{\text{Coul}}}{\mu}}. \tag{3.2}$$

If the loss of kinetic energy during a collision $(K_{\text{rel}}^{\text{before}} - K_{\text{rel}}^{\text{after}})$ is greater than the excess kinetic energy as compared to the Coulomb barrier $(K_{\text{rel}}^{\text{initial}} - E_{\text{Coul}})$, then the particles are trapped behind the barrier. The maximum relative initial velocity $(v_{\text{rel}}^{\text{max}})$, above which coalescence is not possible, is derived from the situation where, during a collision, insufficient kinetic energy is removed through the action of the coefficient of restitution and the particles fly apart.
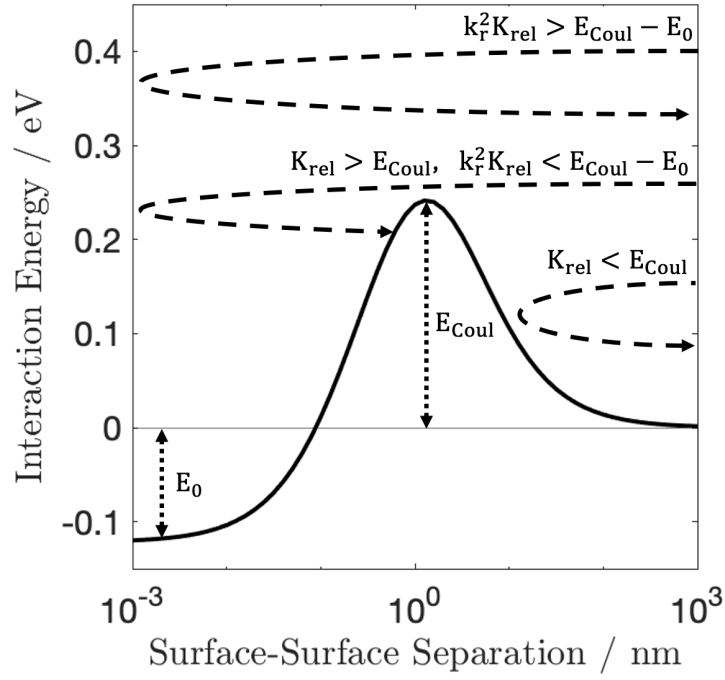
Figure 3.1: *Possible outcomes for a collision between like charged particles. The total energy is schematically split into two components: the electrostatic interaction energy (solid) and the relative kinetic energy (dashed). The electrostatic interaction energy profile is calculated for a collision between ice particle ($r_1 = 3$ nm) and SiO_2 particle ($r_2 = 0.5$ nm) both carrying the charge of $q_1 = q_2 = $ -1e.*

This maximum initial velocity is given by:

$$v_{\text{rel}}^{\max} = \sqrt{\frac{2[(E_{\text{Coul}} - E_0)/k_r^{\,2} + E_0]}{\mu}}. \tag{3.3}$$

Such collision scenarios are illustrated in Figure 3.1 based on an example case of a small SiO_2 particle colliding with a larger ice particle both carrying a negative charge of $q_1 = q_2 = -1e$. Three possible outcomes are described. If the relative kinetic energy of the colliding particles is smaller than the height of the Coulomb barrier ($K_{Rel} < E_{Coul}$) then the particles always repel one another without energy loss. If the particles collide inelastically with a relative kinetic energy sufficient to overcome the Coulomb barrier, the loss of kinetic energy during a collision may prevent their subsequent separation and lead to the formation of a stable, or metastable, aggregate ($K_{Rel} > E_{Coul}$, $k_r^2 K_{Rel} < E_{Coul} - E_0$). If the energy loss during such a collision is not sufficient to stabilise
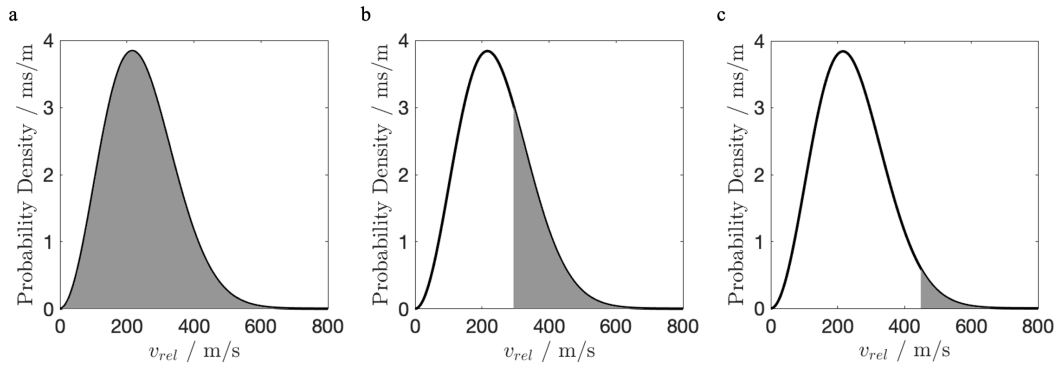
Figure 3.2: *Aggregation probability, indicated by the shaded area, for a collision between SiO₂ particle (r₂ = 0.2 nm, q₂ = -1e) and ice particle (r₁ = 30 nm) as defined by the Maxwell-Boltzmann distribution of the relative velocity at T = 150 K: (a) the case of neutral ice particle (q₁ = 0), the probability of aggregation is one as $P(v_{\text{rel}})$ is integrated in the velocity range of [0,1192] ms⁻¹; (b) q₁ = -1e, the probability of aggregation is 0.293 as $P(v_{\text{rel}})$ is integrated in the velocity range of [295,1219] ms⁻¹; (c) q₁ = -2e, the probability of aggregation is 0.034 as $P(v_{\text{rel}})$ is integrated in the velocity range of [450,1260] ms⁻¹. The values of $v_{\text{rel}}^{\min}$ and $v_{\text{rel}}^{\max}$ are taken from Table 2.*

the pair, the particles rebound and separate ($k_r^2 K_{Rel} > E_{Coul} - E_0$). The latter case may be applicable in warmer regions of the atmosphere where particles move with higher velocities. In this work, we consider a wide range of particle velocities in order to identify a wide range of possible collision outcomes. The probability distribution for the relative velocity of two colliding particles in the form of a Maxwell-Boltzmann distribution at temperature T is given by [76]

$$P(v_{\text{rel}}) = \sqrt{\frac{2}{\pi}} \left(\frac{\mu}{kT} \right)^{3/2} v_{\text{rel}}^2 e^{-\frac{\mu v_{\text{rel}}^2}{2kT}}. \tag{3.4}$$

assuming the direction of the velocity of the three-dimensional particles' is along the axis of particle alignment.

In Figure 3.2, representative examples for the Maxwell-Boltzmann distribution of the relative velocities are shown for collisions between SiO₂ particles carrying a charge of q₂ = -1e and ice particles with q₁ = 0, -1e, and -2e at T= 150 K. If the surface charge is represented by a point charge residing on the particle's surface then the orientational geometry of a collision becomes important. Figure 3.3 shows the geometries considered in this study, both for
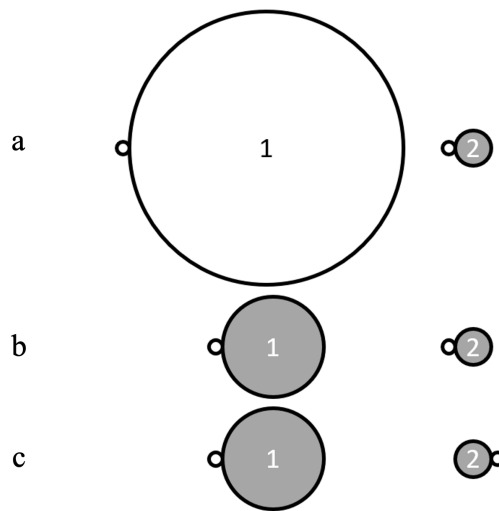
Figure 3.3: *Position of the point charge on the surface of colliding particles depicted by a small open circle: (a) ice particle (1) and small oxide particulate (2); (b) and (c): both particles (1 and 2) are oxides.*

collisions between ice particles and small metal oxide particulates (Figure 3a) and for collisions between metal oxide particles (Figures 3b and 3c).

Bichoutskaia *et al.*[69] have shown conclusively that, between like-charged attraction between particles is strongly size-dependent, such that particles carrying the same amount of charge should have dissimilar sizes. This effect becomes more noticeable with the increase of the ratio of particle radii, r_1/r_2; as the ratio increases, surface charge polarisation becomes more pronounced, leading to strong attraction at short separation distances and a reduction of the Coulomb barrier. This effect is illustrated in Figure 3.4a, which shows electrostatic interaction energy profiles as a function of separation distance for collisions between like charged ice and SiO_2 particles ($q_1 = q_2 = $ -1e) as the size of the ice particle varies between $r_1 = $ 10 nm, 20 nm and 30 nm. As the ice particle becomes larger, the height of the Coulomb barrier decreases, which in turn can affect the outcome of a collision. Note that Figure 3.4 refers to a collision geometry shown in Figure 3.3a which favours the attractive interaction between two particles, each with a point charge located on their surface.

In this example, SiO_2 particle approaches the ice particle from the direction opposite the location of the point charge on the latter, and this collision cor-
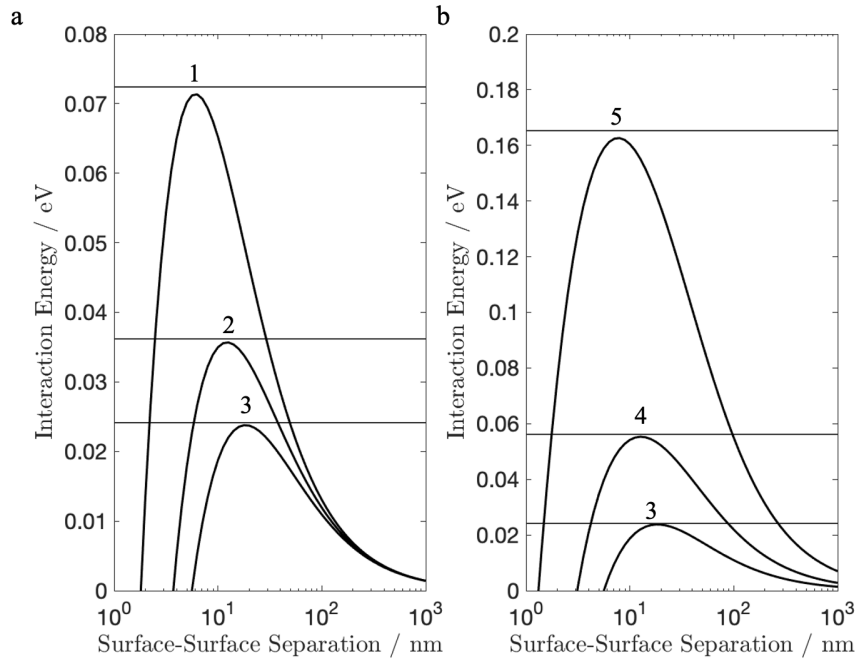
Figure 3.4: *Electrostatic interaction energy as a function of the separation distance between an ice particle and a SiO_2 particle ($r_2 = 0.2$ nm, q_2 = -1e) in the geometry shown in Figure 3.3a. Horizontal lines indicate the value of the Coulomb energy barrier obtained using the uniform surface charge model: (a) the charge of the ice particle is q_1 = -1e, and the radius varies as r_1 = 10 nm (line 1), 20 nm (line 2) and 30 nm (line 3); (b) the radius of the ice particle is r_1 = 30 nm, and the charge varies as q_1 = -1e (line 3), -2e (line 4) and -5e (line 5). Note the change of scale on the y-axis.*

responds to the least repulsive interaction. An equivalent scenario has been considered assuming a uniform distribution of surface charge on both particles, following the approach described in [69]. The height of the Coulomb barrier obtained using a uniform distribution of surface charge is depicted in Figure 3.4 by horizontal lines. For the size of particles considered in this work, these two approximations give very similar results. Although the height of the Coulomb barrier is strongly influenced by the size of the large ice particle (Figure 3.3a), it shows no change with variation in sizes of SiO_2 particles considered here.

The height of the Coulomb barrier is affected even more greatly when the charge of colliding particles is changed. In the case considered in Figure 3.4b, the charge on ice particle was increased from $q_1 = -1e$ to $-5e$ to show almost linear dependence of the barrier on charge variation, in accordance with the leading Coulomb energy term $E \propto \frac{q_1 q_2}{s}$. The variation of the electrostatic

energy with particle size shown in Figure 3.4a is a more subtle effect related to surface charge polarisation (note in Figure 3.4b the change of scale along y-axis).

3.3   Modelling Ice and Mesospheric Dust

Table 3.2 shows values of $v_{\text{rel}}^{\min}$ and $v_{\text{rel}}^{\max}$ calculated using equations 3.1 and 3.3 with $k_r = 0.9$ upon the collision between an SiO_2 MSP and and ice particle. Integrating the probability distribution shown in Figure 3.2 between these limits gives the probability that the particles in questions will possess the required velocity for aggregation. The results are presented in Table 3.2, where aggregation is expressed as a percentage of all collisions. Table 3.2 summarises results for the aggregation of a metal oxide particle, with a fixed size and charge, with ice particles of varying size and charge. These data show that large ice particles with low charge have the highest probability of coalescence with like-charged metal oxide particles. However, in many cases the Coulomb barrier prevents aggregation of particles with the kinetic energies typically found in the MLT region ($kT = 12.9$ meV at $T = 150$ K), assuming that thermal motion is the predominant contribution to velocity. The barrier can be overcome by a small number of high kinetic energy particles found in the tail of the Maxwell-Boltzmann distribution of molecular speeds at 150K. For these particular interactions, the free charge on the surface of both colliding particles is described by a point charge with the geometry shown in Figure 3.3a, and the change in electrostatic interaction energy is due to a redistribution of bound charge (polarisation effects). Note that for ice particles with higher charges, a uniform distribution of free charge might be more appropriate. As mentioned previously, if the initial relative velocity of the incoming particles is smaller than $v_{\text{rel}}^{\min}$ the two like charged particles repel (case 1 shown in Figure 3.1), however if it is greater than $v_{\text{rel}}^{\max}$ the particles do not coalesce but instead fly apart due to the residual excess kinetic energy (case 3). Therefore, only

collisions with a relative initial velocity greater than $v_{\text{rel}}^{\text{min}}$ and smaller than $v_{\text{rel}}^{\text{max}}$ lead to coalescence. In these examples, a change of the coefficient of restitution, k_r, would not affect the probability of aggregation as k_r only reduces $v_{\text{rel}}^{\text{max}}$, and values of the latter that fall within the temperature range appropriate for these calculations have extremely low probabilities.

Table 3.2: Energetic considerations and the percentage of aggregation for SiO_2 - ice collisions at T = 150K and k_r = 0.9 (the surface point charge model). SiO_2 particle has the fixed radius and charge (r_2 = 0.2 nm, q_2 = -1e), and the size and charge of ice particle is varied. The collision geometry is shown in Figure 3.3a. The interactions of MgO and FeO particles with ice show the same trend (see Tables in appendix B).

Ice Particle	E_{Coul}, meV	$v_{\text{rel}}^{\text{min}}$, ms^{-1}	$v_{\text{rel}}^{\text{max}}$, ms^{-1}	Aggregation %
r_1 = 30 nm; q_1 = 0	0	0	1192	100
r_1 = 30 nm; q_1 = -1e	23.8	293	1219	29.9
r_1 = 30 nm; q_1 = -2e	55.3	447	1260	3.57
r_1 = 20 nm; q_1 = 0	0	0	1235	100
r_1 = 20 nm; q_1 = -1e	35.7	361	1275	13.7
r_1 = 20 nm; q_1 = -2e	82.9	547	1333	0.50
r_1 = 10 nm; q_1 = 0	0	0	1251	100
r_1 = 10 nm; q_1 = -1e	71.3	511	1330	1.15
r_1 = 10 nm; q_1 = -2e	165.8	780	1441	0

Figure 3.5 shows coalescence results where the size of the ice particle has been increased to 100 nm. These data reinforce the fact that, for like-charge collisions, an increase in the size of the ice particle from 10 nm to 100 nm can lead to an order of magnitude increase in the probability of aggregation. Also given in Figure 5 are data calculated for a charge of -2e on the ice particle. In this case, the probability of aggregation is increased from zero (for r_1 < 20 nm) to more than 40% (for $r_1 \approx$ 100 nm), thus providing a mechanism whereby ice particles can increase their charge, but still participate in aggregation processes.

The results in Table 3.2 and Figure 3.5 demonstrate that there are several routes whereby ice particles can become contaminated by both neutral and like-charged MSPs. These calculations on the coalescence of ice particles and dust are supported by the experimental observations of [77], who have identified the presence of meteoric smoke in ice particles. Our results also point to
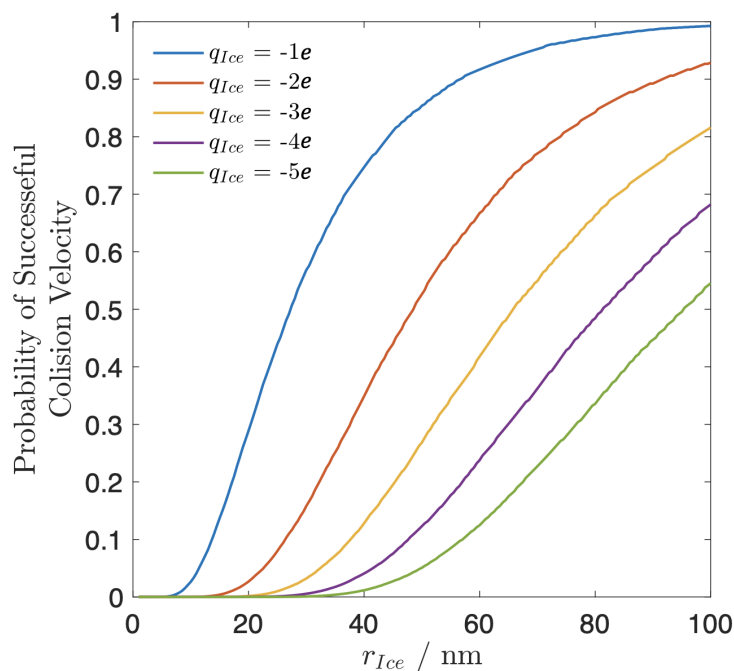
Figure 3.5: *Aggregation probability, presented as percentage, for a collision between SiO_2 particle ($r_2 = 0.2$ nm, $q_2 = $ -1e) and ice particle ($q_1 = $ -1e and $q_1 = $ -2e) whose size varies from $r_1 = 1$ nm to 100 nm.*

coagulation rather than condensation as a possible growth mechanism. Further studies are however required to help understanding how the collision probabilities influence the magnitudes of rate coefficients for coagulation.

3.4   Aggregation of metal oxide and silica particles

The abundant presence of metal oxide and silica particles in meteoric smoke in the MLT region [78] leads to a possibility that these may also aggregate, and with radii ranging from 0.2 nm to 5 nm, these are amongst the smallest particles found in this region of atmosphere. Their size means that if the point charge approximation is used to describe the surface charge, then the exact location of the point charge on the surface of each colliding particle becomes very important because, as shown previously by [50], collision geometry can alter the strength of the electrostatic interaction. This statement does not

apply to most like-charged interactions because, as shown in Table 3.3, the height of the Coulomb barrier prevents very small like-charged particles (less than 5 nm radius) from aggregating. Note that collisions between like-charged silica particles have lower energy barriers than those calculated for collisions between iron oxide particles. For collisions involving larger particles ($r_1 = 5$ nm), despite the lower energy barriers the minimum initial velocity ($v_{\text{rel}}^{\text{min}}$) required to overcome the barriers for SiO_2 are still higher for than those for FeO particles. These effects arise from differences in density and mass.

Table 3.3: Energetic considerations and the percentage of aggregation for SiO_2 - SiO_2 and FeO - FeO collisions at T = 150K and $k_r = 0.9$ (the surface point charge model). Particle 2 has the fixed radius and charge ($r_2 = 0.2$ nm, $q_2 = -1e$), and the size and charge of particle 1 is varied. The collision geometry is shown in Figure 3b.

SiO_2 - SiO_2	E_{Coul}, meV	$v_{\text{rel}}^{\text{min}}$, ms^{-1}	$v_{\text{rel}}^{\text{max}}$, ms^{-1}	Aggregation, %
$r_1 = 0.2$ nm; $q_1 = 0$	0	0	8112	100
$r_1 = 1.0$ nm; $q_1 = 0$	0	0	3914	100
$r_1 = 5.0$ nm; $q_1 = 0$	0	0	2187	100
$r_1 = 0.2$ nm; $q_1 = -1e$	2889	4566	9168	0
$r_1 = 1.0$ nm; $q_1 = -1e$	622	1504	4156	0
$r_1 = 5.0$ nm; $q_1 = -1e$	125	671	2273	0.02
FeO - FeO				
$r_1 = 0.2$ nm; $q_1 = 0$	0	0	2876	100
$r_1 = 1.0$ nm; $q_1 = 0$	0	0	1811	100
$r_1 = 5.0$ nm; $q_1 = 0$	0	0	1307	100
$r_1 = 0.2$ nm; $q_1 = -1e$	3056	3175	4150	0
$r_1 = 1.0$ nm; $q_1 = -1e$	679	1068	2055	0
$r_1 = 5.0$ nm; $q_1 = -1e$	136	476	1376	0.03

For collisions between charged and neutral particles the Coulomb barrier is always zero, and their aggregation is driven by polarisation effects. Again, orientation of the particles becomes important and here two limiting cases are considered. Table 3.3 corresponds to the case where the point charge on the surface of particle 2 faces the neutral particle 1 (geometry shown in Figure 3.3b, but we now assume that particle 1 is neutral). In this configuration, there is strong attraction as the point charge approaches the neutral particle leading to a re-distribution (polarisation) of surface charge on the latter. This

leads to a significant increase in the binding energy between the particles (E_0) and results in coalescence through the subsequent action of the coefficient of restitution. Irrespective of particle composition, the absence of a Coulomb barrier results in aggregation for all of the examples examined in Table 3.3. The data displayed in Table 3.4 correspond to the case least favourable to aggregation between neutral and charged particles. Here, the point charge on the surface of particle 2 faces away from the neutral particle 1 (geometry shown in Figure 3.3c but particle 1 is neutral). In this orientation, collisions with the smallest charged particles ($r_2 = 0.2$ nm) strongly favour aggregation often resulting in a 100% coalescence outcome, even though the maximum relative initial velocity of colliding particles required for coalescence is significantly lower. When the charged particle is very small, the interaction resembles a point charge - neutral particle case which is always attractive. Note that the aggregation remains almost complete (100%) even when both charged and neutral particles are extremely small ($r_1 = r_2 = 0.2$ nm) and highly polarisable (FeO, MgO). In general, there are distinct differences between the aggregation outcomes for SiO_2 particles and the more polarisable FeO particles, with the FeO collisions consistently having higher percentage aggregation and MgO particles lie somewhere between the two. For the geometry shown in Figure 3.3c, the aggregation percentage drops very significantly as the size of the charged particle 2 grows. This is because any surface polarisation response on the neutral particle due to the presence of a point charge on the surface of particle 2 is now hindered by the volume of the charged particle itself. Finally, when the charged particle is large and the neutral one is very small, surface polarisation effects on the neutral particle are negligible and aggregation does not occur. This can be illustrated by comparing two examples: if $r_2/r_1 = 10$ (radius of charged particle is ten time bigger than that of neutral particle) the aggregation is 0%, and if $r_1/r_2 = 10$ (radius of neutral particle is ten time bigger than that of charged particle) the aggregation is 100% (Table 3.4).

Table 3.4: Energetic considerations and the percentage of aggregation for SiO_2 - SiO_2 and FeO - FeO collisions at T = 150K and $CR = 0.9$ (the surface point charge model). Particle 2 has the fixed charge (q_2 = -1e) and particle 1 is neutral ($q_1 = 0$), and the size of both particles is varied. The collision geometry is shown in Figure 3c.

r_1 / nm	r_2 / nm	SiO_2 - SiO_2		FeO - FeO		MgO - MgO	
		v_{rel}^{max} , m/s	aggregation,%	v_{rel}^{max} , ms^{-1}	aggregation,%	v_{rel}^{max} , ms^{-1}	aggregation,%
0.2	0.2	364	58.3	445	96.0	495	93.1
0.2	1.0	569	99.7	625	100	714	100
0.2	5.0	737	100	748	100	869	100
1.0	0.2	34.2	0.29	29.8	0.49	29.3	0.29
1.0	1.0	14.6	9.75	18.0	36.3	20	30.4
1.0	5.0	22.8	57.2	25.2	91.4	28.7	88.4
5.0	0.2	9.00	0.01	0.0*	0.0*	0.0*	0.0*
5.0	1.0	1.42	0.02	1.15	0.04	1.24	0.03
5.0	5.0	0.59	1.01	0.72	4.78	0.80	3.81

* zero within the accuracy of our calculations

Finally, if the results given in Table 3.3 and 3.4 for percentage aggregation are compared, it can be seen that there are differences that depend on how the point charges are orientated on these particles, all of which have comparatively low dielectric constants. In all instances where a charge is pointing towards a large polarisable particle (Table 3, when $q_1 = 0$ and $q_2 = -1e$), aggregation is 100%. However, when in Table 4 the charge is located at 180° from the adjacent particle (case 3c in Figure 3), aggregation drops to 58% when in the least polarisable particle pair, SiO_2, the neutral particle has a radius of 0.2 nm. As the dielectric constant increases on moving to MgO and FeO the particles become more polarisable and the percentage aggregation increases.

3.5   Conclusion

This work is focused on the description of basic principles underpinning the coalescence of ice and dust particles in thermal motion. Specific examples considered in this study examine coalescence between particles, commonly found in the mesosphere, at the temperature T = 150 K which is typical to this region of atmosphere. Pair interactions of charged particulates follow the Coulomb law with an additional contribution from the attraction between like-charged and neutral-charged pairs driven by induced polarisation of the particle surface charge. The latter interactions can be significant at short separation distances between interacting particles. Low temperatures in the MLT region imply that the colliding particles are not very energetic, and for a like-charged pair, the relative kinetic energy is often insufficient to overcome the Coulomb barrier. However, the high energy tail of the Maxwell-Boltzmann distribution of the relative velocity at T = 150 K provides an adequate amount of collisions leading to aggregation both between like-charged particles of ice and dust, and between dust particulates themselves.

Like-charged attraction is more common (and stronger) between particles with low charge. This collision scenario can be described by a localised, point

surface charge model and one where the charge is assumed to be uniformly distributed over the entire surface of a particle. An earlier study by Filippov *et al.* [50] of the interaction between positively charged particles showed that for particles with low dielectric constants, there is a difference in predicted behaviour between these two models. As the dielectric constant increases in value, results from the two models became equivalent. Similarly, differences in orientational geometry of a collision (extreme scenarios are shown in Figures 3.3b and 3.4c) were also found to be evident at low dielectric constants; but again these disappeared as the value of the dielectric constant increased. The presented results provide a basis for future work to estimate the coagulation rates between particles of a given size and charge and their variation with temperature.

Chapter 4

The Importance of Polarisation in Volcanic Ash Clouds

4.1 Introduction

Volcanic ash clouds are of great interest due to both the destruction they have caused throughout history, and the disruption they cause in the present day.[79–84] Due to their high density, and consequential opaqueness, their sudden appearance can cause major disruptions to international travel, the climate and even human health.[81, 85, 86] As such, understanding the transport mechanism of volcanic ash is of crucial importance, and given that these ash clouds are high-temperature environments dense with charged particulates[87–90], understanding the nature of their growth and nucleation is pertinent.

Volcanic ash clouds are composed primarily of silicate, SiO_2,[90, 91] along with other trace elements such as zinc, vanadium, copper, mercury and even uranium. The exact composition of trace elements can be unique to a particular volcano or eruption, as can the characteristics of the silicate particles. [88, 90, 91] Recent analysis has found that in contrast to this, the particles have minimum density variation from site to site, and are thought to be of a similar enough geometry to undergo similar fluidization.[90, 92]

During their transport, these silicate particles readily undergo tribocharging

(the charging of materials through contact), aggregation and de-cumulation,[88, 90, 93] causing a large variation of particulate sizes, charges and charge densities.[90] With such variation in the properties of the ash particles, polarisation could pose a significant contribution to the charge-charge interactions in the system, which also experiences various temperatures throughout the eruption process. Given the lack of magnetic material present in the ash and its macroscopic nature, such systems can be investigated via statistical analysis as done for the aggregation of meteoric dust and ice particles in chapter 3.[94] However, given the various contributions to the particles' velocity in such an atmosphere, an understanding of the particles' behaviour independent of temperature is also required.[93, 95]

Collisional cross-sections are utilised across physics in various capacities to study the influence of long range interactions on the trajectories of particles.[96–98] The definition of the collisional cross section varies from case to case, however, the scalar definition as utilised in [98] has been shown to be particularly versatile with applications in both molecular and particulate systems.[98–100] This also allows one to directly see the variation in the system in comparison to that of non-interacting models, as utilised throughout the literature.[101–103] In this chapter, the aggregation of silicate ash particles is investigated. Firstly, a detailed breakdown of the composition of an ash cloud is presented from data sourced in literature, before the introduction of a dynamic method utilising the framework developed in chapter 2 to determine the collisional cross section of a particle.[98] Initially, the statistical method utilised in chapter 3 [94] is applied to investigate the effect of temperature on the aggregation of the system, before a dynamic investigation of the collisional cross section of volcanic ash is presented.

4.2 Methods

4.2.1 Composition

After volcanic ash clouds have dispersed and fallen to the Earth's surface, the particulates can be collected and examined.[81, 90, 91] Such studies compare these particles, showing variation in their size and composition. The trace elements present in these particulates is also unique to the location and possibly even the individual eruption.[104, 105] However, given the primary component of their composition is silicate, here we assume pure silicate composition, with a dielectric constant of 8 given the exact composition of the sample.[90, 106, 107]
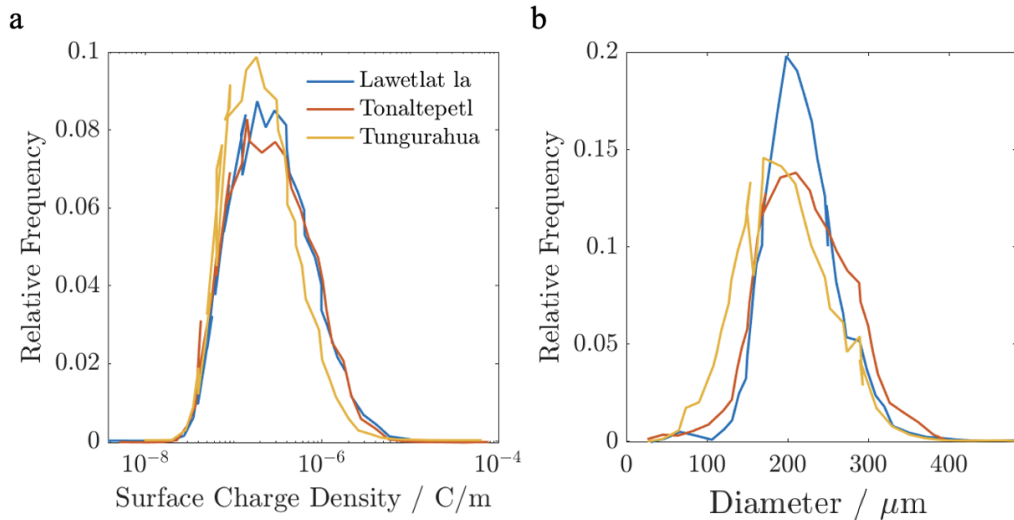
Figure 4.1: *The relative frequency of occurrence of the detection of surface charge density (a) and Diameter (b) of volcanic ash samples from the Lawetlat la (blue), Tonaltepetl (red) and Tungurahua (yellow).*

Although the particles from each eruption are observed to be approximately uniform in composition,[90, 91] they can vary widely in charge, charge distribution and radius.[90] Harper and Dufek [90] observed this by recreating the ejection of volcanic ash under laboratory conditions with samples collected from various ash sites; this was done in an effort to study the lightning often reported during volcanic eruptions. The recreation was required due to the charging mechanism of tribocharging in ash clouds. As such, all samples were analysed after 10 minutes of charging/ejection when a steady state of charge

can be assumed. A small asymmetry in the sign of charge was also observed by Harper and Dufek, [90] with them reporting a 1-4% more negative grains than positive charge.

The probability distributions of surface charge and radius can be seen in figure 4.1. Using these distributions, two particle sizes and surface charge distributions can be randomly chosen to determine the parameters required to investigate the particles nucleation both statistically and dynamically. Given the nearly equal split in the sign of the charged particles, both like charged and oppositely charged interactions are considered.

4.2.2 Collisional Cross-Section

The collisional cross section (CCS) is defined throughout this work as

$$\text{CCS} = \pi b_{max}^2 \tag{4.1}$$

where b_{max} is the maximum distance above the centre of one particle from which a successful collision will occur at a given velocity (the impact parameter), as illustrated in figure 4.2, in which all the particles have the same initial velocity.
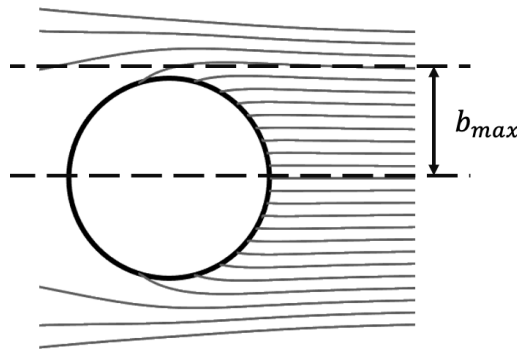
Figure 4.2: *Illustration of like-charge attraction causing a collision with particles as further than sum of their radii, and their relation to b_{max} using a set of trajectories, each of different offset, evaluated with a dynamics implementation the framework extended in 2.*

In the hard sphere approximation it is assumed that particles only interact via

collision and undergo no long range interactions - this approximation can be seen to be accurate at sufficiently high velocity/temperature. It is therefore possible to directly and quantitatively compare the CCS with that of the sum of the radii (r_1 and r_2) of two non-interacting particles, such that

$$CE = \frac{b_{max}^2}{(r_1 + r_2)^2} \tag{4.2}$$

Collisional cross section is largely dependent on the velocity of the incoming particle, a consequence of the particles environment. As such, it is possible to investigate the nature of such collisions in a range of environments, and not just due to thermal motion as in chapter 3.

To conclude, the impact parameter of a system is determined here by the simulation of two particles of varying radius and charge density, as determined from a population of particles, separated by a distance at which their interaction is negligible, are propelled towards one another with some offset from the direct collisions as considered in figure 4.2. These simulations are evaluated via a dynamics implementation of the many body framework that was extended in chapter 2. The maximum offset that leads to a collision is determined to be the impact parameter b_{max}.

4.3   Results and Discussion

The statistical approach to determine the percentage of velocities able to cause aggregation requires the parameters of two particles - as a distribution of sizes and surface charges were measured by Harper and Dufek, [90] the choice of particle parameters for simulation is a non-trivial. As Harper and Dufek [90] present the properties of volcanic ash (charge, charge distribution and size) from three volcanic eruptions, an average was taken of three distributions for each measured parameter.

Whist the charge density of such particulates belongs to a distribution of var-

ious densities, each with a corresponding probability of occurring, the mean free path of a larger particle is much smaller than that of a smaller particle. As such, tribocharging of the larger particles is often assumed to occur more readily leading to more larger particles with a higher than average surface charge density.[108, 109]

Given the distribution of parameters as measured by Harper and Dufek, [90] three particle radii were chosen to investigate the possibility of like charge attraction in these systems, and the effect it could have on aggregation. Each particle was then assigned a randomly chosen surface charge density from the average distribution reported in [90], where the the smaller particle is modelled with the smallest surface charge density, the largest particle has the largest surface charge density and the median sized particle has the median, randomly chosen, surface charge density.

Particle	Radius / μm	σ / μC/m^2	Mass / ng	Charge / fC
Smallest	50	0.0200	13	0.006
Median	100	0.1585	104.3	1.99
Largest	150	1	352	282.7

Table 4.1: The parameters of the particles modelled given a randomly chosen particle size, and an assigned but randomly chosen surface charge density.

The interaction energy as a function of separation was then determined for each possible set of asymmetric particle pairs; the smaller particle interacting with the larger, the larger interacting with the median, and the median interacting with the smaller. The free charge of each particle was assumed to be uniformly spread over the particle's surface; this was chosen as given the magnitude of the charges investigated, it is unlikely that charges of the magnitude considered here will be concentrated on a single point. However, given the smaller size discrepancy observed between volcanic ash particles compared to ice and meteoric dust, less like-charge attraction could be expected to occur. Figure 4.3a shows that particles of the largest and smallest sizes investigated can undergo like-charge attraction, hence forming the most stable state of the system given the global energy minimum as the surface-to-surface separation
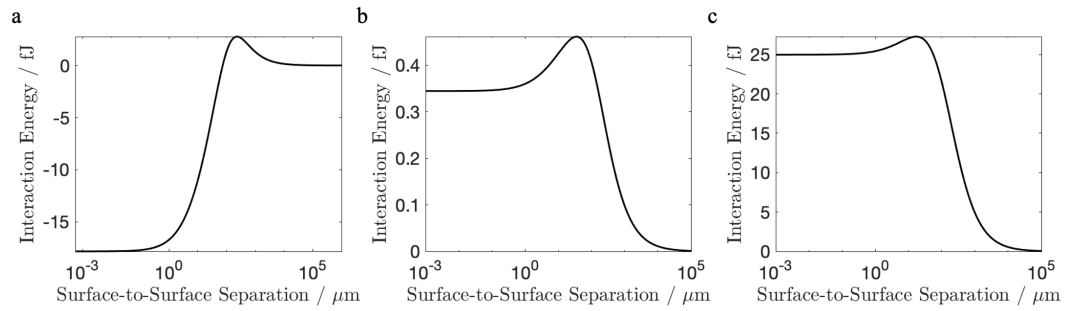
Figure 4.3: *The interaction energy of two uniformly charged particles as a function of surface-to-surface separation. The particles have radii: 50 μm and 150μm (a), 50 μm and 100μm (b), and 100 and 150 μm (c).*

tends to zero. In contrast, the combination of the smallest or larger particle with the median particle (figures 4.3b and c respectively), can be seen to have a local energy minimum at the same point as the global minimum in figure 4.3a.

Given the presence of a minimum at close separation, all the systems shown in figure 4.3 are capable of aggregating due to their charged nature; after a certain separation all systems studied here will undergo a force pushing the particles together. However, for the system shown in figure 4.3a the barrier to cluster destruction is greater than that of particle formation, which is not the case in figure 4.3. Given that such systems are subject to random fluctuations, such as those due to temperature, these metastable states are expected to have a shorter lifetime than their stable counter parts.

Volcanic ash clouds are subject to a range of temperature conditions, ranging from 1000^oC when inside the volcano and just after ejection, to the temperature of the ground upon deposition. Unlike most charged particle environments, several examples of which are given throughout this work, volcanic eruptions have a time and location dependent background temperature. Given the variation of the size and charge of the particles in this environment, and the presence of a theoretical maximum charge density as calculated by Harper and Dufek, [90] it is unknown if the particles, such as those investigated in figure 4.3, can self-assemble at certain temperatures to form larger particles. By considering the Boltzmann distribution of each pair of particles, the percentage of particles

at velocity able to cause aggregation can be considered.
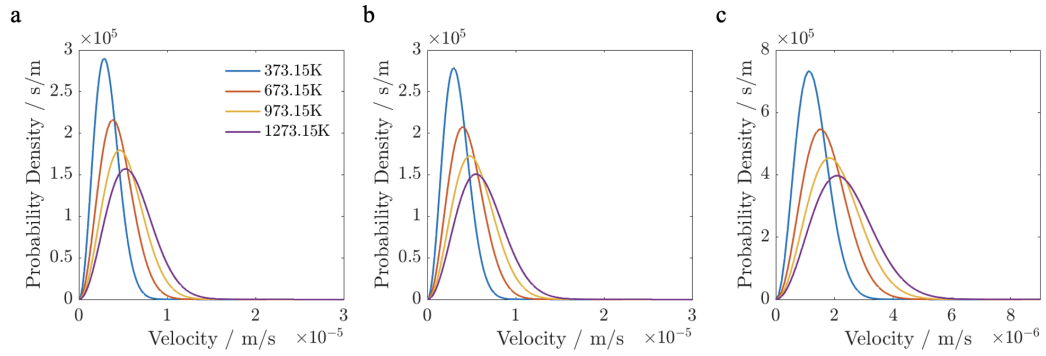
Figure 4.4: *The Boltzmann distribution of probability density as a function of velocity, for the largest -small (r = 50, 150μm) (a), smallest-median (r = 50, 100μm)(b) and median-largest (r = 100, 150μm) (c) particle pairs at: 373.15 K (blue), 673.15 K (red), 973.15 K (yellow) and 1273.15 K (purple). Note the change in scale of the both axis.*

Figure 4.4a and b show that the possible velocities of particles are extremely similar for the big-small and small-median sized particle pairs but much smaller for the median-large particle pair (figure 4.4c). This is due to the Boltzmann distributions dependence on the reduced mass of the system, which is the only difference between variations a-c of figure 4.4. As the reduced mass of the system tends to the smaller of the values being combined in its evaluation, this is to be expected for the pairs that contain particles of the smallest size in figure 4.4. Velocities in the micrometer per second regime are shown to be a regular occurrence at many temperatures in figure 4.4, and as the particles are of a micrometer size, this implies that at such temperatures the particles are mobile (in a manner comparable to their size over a second) due to thermal fluctuations. Although the particles appear to be of a comparable size when considering their radii, due to the cubic scaling of the volume with respect to the radius, the mass of the largest and median particle is 27x and 8x that of the smaller particle respectively, hence justifying the change in scale of the x-axis in figure 4.4.

However, such thermal fluctuations should be carefully considered as these particles are extremely charged and will undergo a repulsive force for the majority of their approach towards one another given the range of their interaction, not-

ing the use of the log scale on the axis of figure 4.3, and considering that the Boltzmann distribution assumes the particles only interact via collisions. However, upon comparison of figure 4.4 and table 4.2, it can be seen that percentage of particles with sufficient velocity to overcome any of the Coulomb barriers shown in figure 4.3 is approximately zero. This can be seen upon inspection of figure 4.4 as every minimum velocity shown in table 4.2 would be to the far right of its corresponding Boltzmann distribution, with the maximum velocity able to cause aggregation of an even greater magnitude.

Pair	Reduced Mass / ng	E_{Coul} / fJ	E_0 / fJ	v_{min}^{rel} / mm/s	v_{max}^{rel} / mm/s
Smallest-Largest	1.257	2.768	-17.8	2.1	82.7
Median-Largest	8.046	27.28	24.98	2.6	7.40
Median-Smallest	0.4618	1	0.3446	0.8927	7.50

Table 4.2: The parameters of the particles modelled given a randomly chosen particle size, and an assigned but randomly chosen surface charge density.

This absence of aggregation due to thermal fluctuations is not conclusive proof that the like-charge attraction does not occur in such environments as many other perturbations that could drive the these particles close enough to attract, such as turbulent flow, initial ejection, falling under gravity, and weather effects such a wind. Such perturbations cannot be modelled as consistently due to the specific environmental factors they depend on. Therefore, given the violence of such eruptions, and the drastic winds and lightning caused as a result of the eruption, the particles may still possess a great enough velocity to overcome the Coulomb barrier.

If one assumes that there is some probability a smaller particle can gain a higher surface charge density, and that the use of surface charge density already adequately scales the charge each particle with respect to its size, then the more favourable interaction of a highly charged smaller particle interacting with a larger particle can be realised. Given the various possible values of both the radii and surface charge density, two were selected at random from the average distributions of each and assigned accordingly, as shown in table 4.3.

Particle	Radius / μm	σ / μC/m^2	Mass / μg	Charge / fC
Smallest	57.05	1.74	0.401	71.2
Largest	156.7	0.0473	1.94	14.6

Table 4.3: The parameters of the particles modelled given a randomly chosen particle size and surface charge density.

Figure 4.5 shows that the Coulomb barrier is of a comparable size to those shown in figure 4.3, and as such no thermal motion is likely to overcome the barrier at temperatures ranging up to 1000 ^{o}C. However, there does appear to be an increased in stability of this system (deeper minimum) than those studied in figure 4.3.
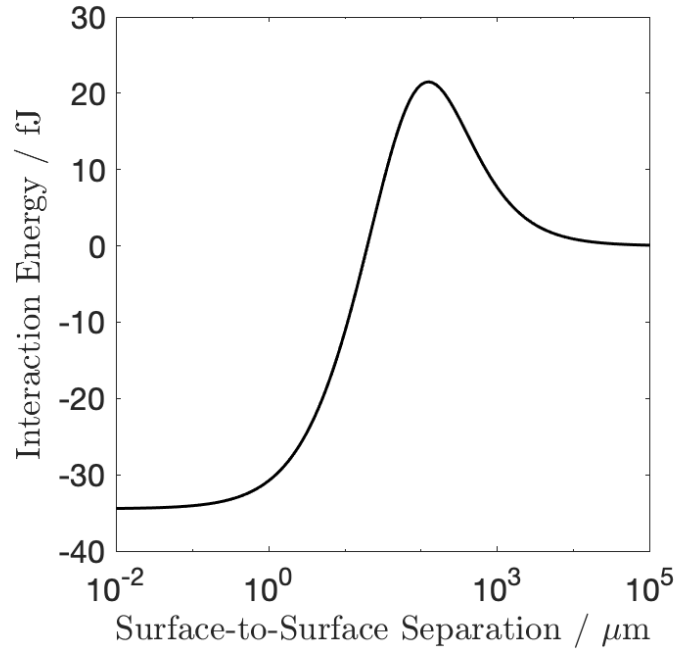
Figure 4.5: *The interaction energy as a function of surface-to-surface separation between the smallest particle in table 4.3(q = 71.2 fC, r = 57.05 μm) and the largest (q = 14.6 fC, r = 156.7 μm).*

To investigate the range of the interaction of these particles, given a fluctuation of great enough magnitude to propel the particles toward one another, the impact parameter, b_{max}, was determined via a dynamics implementation of the mathematical framework extended in chapter 2. b_{max} was determined by considering multiple trajectories of the smaller particle towards the larger particle at a given velocity. Given an offset less than or equal to b_{max}, and a great enough velocity to overcome the Coulomb barrier, the particles will

collide. However, offsets greater than b_{max} will cause the particles not to collide. As such, it is possible to determine b_{max} dynamically by trial and error. This was investigated for several incident velocities as seen in figure 4.6. As figure 4.5 enables one to determine E_0 and E_{Coul}, and consequently v_{min}^{rel} and v_{max}^{rel}, one can also test the accuracy of this method of investigation against the statistical method utilised in chapter 3, as the first non-zero impact parameter should occur close to v_{min}^{rel} (-0.0051 m/s).
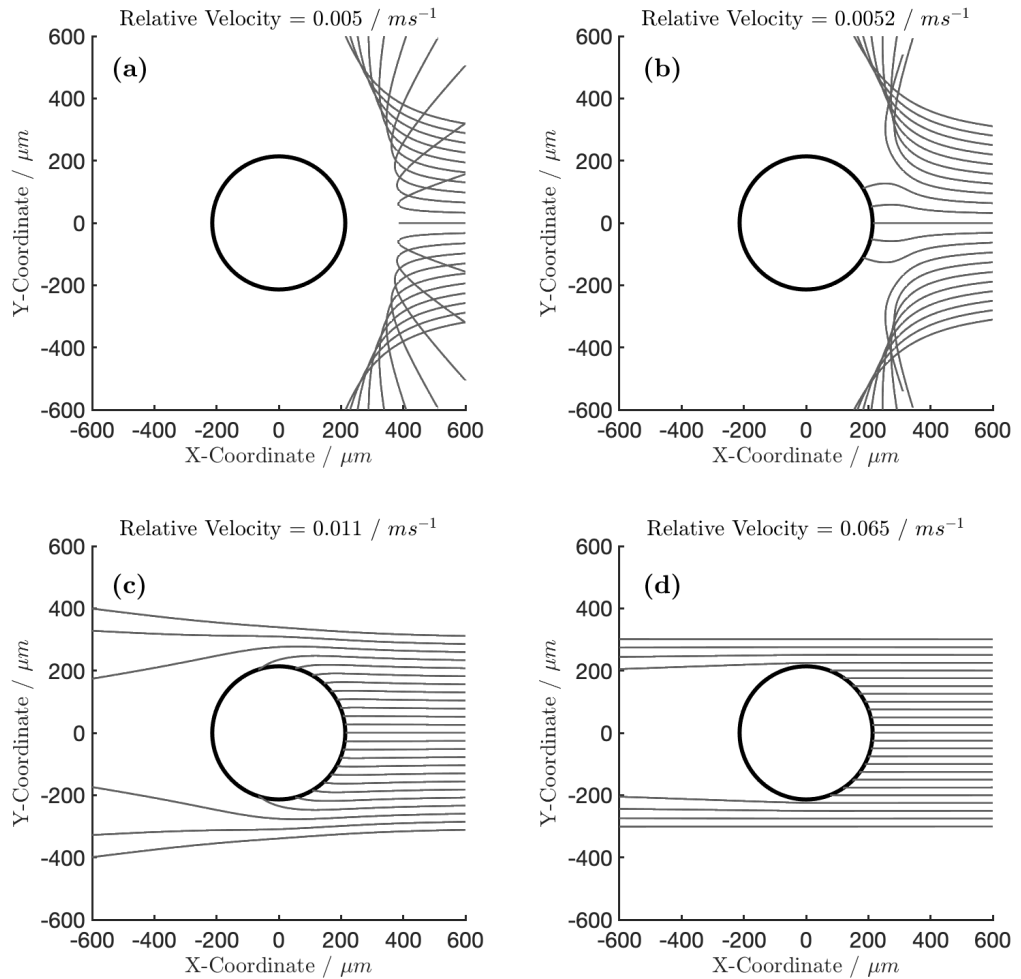
Figure 4.6: *Particle trajectories of the smallest particle (q = 71.2 fC, r = 57.05 µm) approaching the largest particle (q = 14.6 fC, r = 156.7 µm), for which v_{min}^{rel} = 0.0051 m/s, with relative velocities 0.005 m/s (a), 0.0052 m/s (b), 0.011 m/s (c), and 0.065 m/s (d). The centre circle shows the combined radius of the two particles, i.e. the location of smallest particles centre location upon collision. Each simulation was modelled using a timestep of 0.1µs.*

As expected, if the particle has a velocity less than that of the critical veloc-

ity, no successful collisions can occur in the dynamic simulation, and all the particles are strongly repelled, as seen in figure 4.6. It is worth noting that although the particles do not collide directly, the scattering angle of the system appears large for even small offsets. As such, if the particles in an ash cloud were moving at this velocity although no particles would ever collide, particles would still undergo various accelerations due to long-range interactions.

As the velocity of the trajectories is increased, the more central of the trajectories (as seen in figure 4.6b) begin to overcome the Coulomb barrier, enabling the particles to accelerate towards one another and collide. The effect of repulsion between the particles can also be observed in figure 4.6b, as seen by the curvature of the off-centre trajectories. It is worth noting that for the velocities considered in figure 4.6b, any particles that collide would eventually stick together if no other perturbation occurs, as would any collision below 9.5 mm/s (v_{max}^{rel}) but greater than 5.1 mm/s.

The collisional cross section of a particle can be greater than the sum of the two radii, even if they are like-charged as shown by figure 4.6c, in which the velocity at which the maximum impact parameter occurs is illustrated by the highest trajectory to result in a collision. Therefore, the two ash particles (as in table 4.3) with velocity 0.011 m/s have the maximum probability of colliding with one another with respect to their velocity. However, as this is more than 9.5 mm/s (v_{min}^{rel}) many of these particles will not aggregate.

At extremely high impact velocities, the ash particles would behave according to the hard sphere approximation - almost independently of their charge, as shown in figure 4.6d. A small amount of scattering is observed in figure 4.6d for closest trajectory to the surface of the particle, showing that such like-charge attraction can be observed within a relatively small space due to the strength of the interaction. This is supported by the steeper gradient left of the Coulomb barrier compared to the right where $F = -dU/ds$, where s is the surface to surface separation and U is the interaction energy. If the particles do not deform in these collisions, then it is suspected that none of the trajectories

in figure 4.6d would result in nucleation. However, given the low coefficient of restitution of ash (0.69) and its malleable nature these particles may still aggregate due to deformation upon impact.

Given such variation of the impact parameter, and consequently the probability of particles colliding upon perturbation, with the particle velocity, in conjunction with b_{max} quadratic effect on the collision efficiency in the systems as illustrated by equation's 4.1, polarisation could be key to the behaviour of these fast moving particles, and therefore their aggregation and nucleation. As such both b_{max} and CCS should be considered to be a function of velocity.
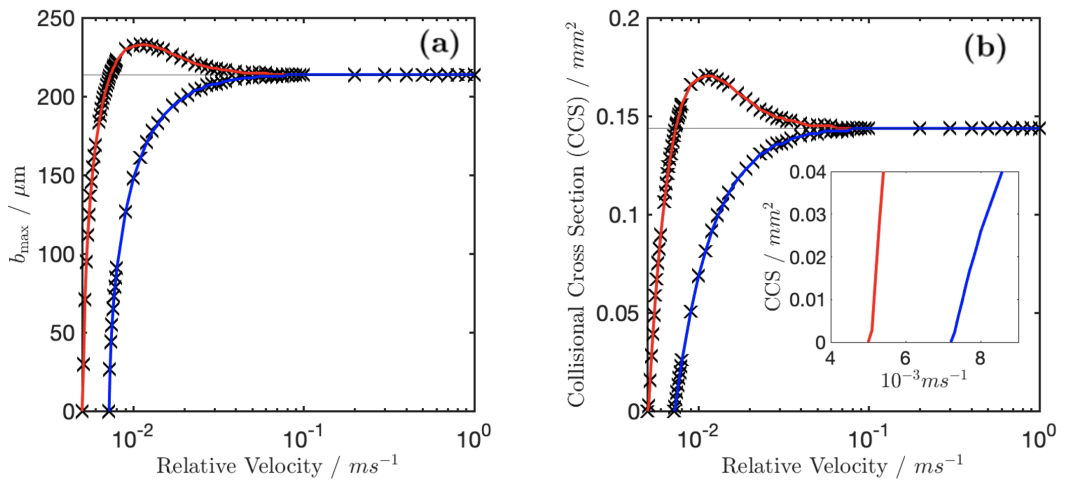
Figure 4.7: *The impact parameter (a) and collisional cross section (b) as a function of relative the velocity of the smallest particle in table 4.3(q = 71.2 fC, r = 57.05 μm) approaching the largest particle (q = 14.6 fC, r = 156.7 μm), with (red) and without (blue) polarisation accounted for compared to the hard sphere approximation (grey).*

It can be seen in figure 4.7 that although these particles have the same sign of charge, the impact parameter determined here is still 9% larger than that of the particle pair when polarisation is not accounted for. As such, the collisional cross section of this system has increased by 19%.

Figure 4.7 also highlights the drastic difference of accounting for polarisation in comparison to using purely Coulombic models. Not only is there a 40% increase in the initial velocity able to cause an impact in the simulation as seen in the inset, but by accounting for polarisation, it can be seen that the particle pair is most likely to undergo such a collision (maximum b_{max}) with

a relative velocity of 0.0330 m/s, as the sum of the radii of the particles has increased by 19% . In comparison, the impact factor and CCS as determined by the Coulombic simulation (blue line) are still less than half of the hard-sphere case at the same velocity.
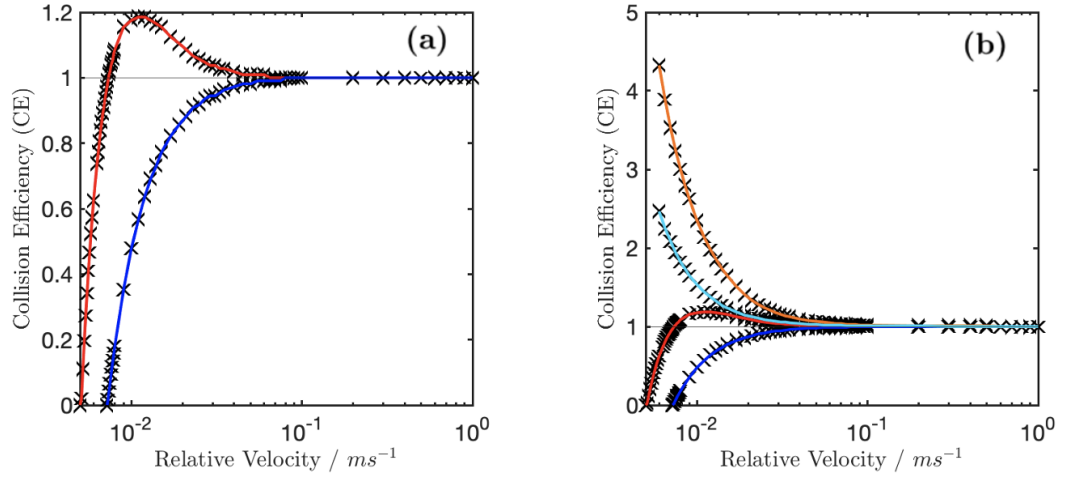
Figure 4.8: *The collision efficiency of the particles undergoing the collision, as a function of relative the velocity of the smallest particle in table 4.3(q = 71.2 fC, r = 57.05 μm) approaching the largest particle (q = 14.6 fC, r = 156.7 μm), with (red) and without (blue) polarisation accounted for compared to the hard sphere approximation (grey), and upon a change in sign of the smallest particle in table 4.3, the outcome of the same analysis with (yellow) and without (cyan) polarisation.*

The collision efficiency as defined in equation 4.2, enables graphical comparison of the requirement for polarisation, as it illustrates the large discrepancy caused by accounting for polarisation, from the methods utilised in previous granular models,[110, 111] and how much more likely the particle is to undergo such collisions under such conditions in direct comparison to the Coulombic case, with the collisional efficiency of 1.19 at 0.0330 m/s accounting for the polarisation of the system, in comparison to a collision efficiency of 0.45 at the same velocity.

Although only the like-charged case has been studied thus far, it is clear from figure 4.8 that polarisation is of equal importance in the interactions between oppositely charged particles which with polarisation has a 69% greater collision efficiency than without. In the case of oppositely charged particles, the maximum collision efficiency of the system, in both cases considered in figure

4.8, occurs at 0 surface-to-surface separation, in complete contrast to the like-charged case. As such, it can be seen that nucleation in such an environment could occur readily in the oppositely charged case, and at an even greater rate than Coulombic models or hard-sphere models would suggest.

4.4 Conclusion

In conclusion, we have found that for particulates within volcanic ash clouds, there exists a relative velocity able to induce collision and aggregation in the case of both the oppositely and like-charged particle pairs due to the polarisation interactions between them. The capacity of polarisation to accelerate this aggregation in comparison to the pure Coulombic or hard-sphere approximations has also been realised via a novel application of the formalism developed upon in chapter 2. Whilst the velocities required for such collisions cannot originate from thermal fluctuations for any of the cases considered throughout this chapter, the aggregation of volcanic ash remains not impossible given the violent winds and ejections associated with a volcanic eruption and the findings of this chapter.

Chapter 5

Electrostatic Interactions in Dry Powder Inhalers

5.1 Introduction

Electrostatic tribocharging of pharmaceutical powders can adversely affect formulation and aerosolisation processes, manufacture and handling procedures, and alter the properties of powder flow. [112–115] Finding solutions to control the effects caused by particle charging in various powder delivery systems, such as the metered dose inhaler (MDI) or the dry powder inhaler (DPI), could offer the potential to improve device dosing consistency and targeted deposition in the respiratory system. [116–118] In pharmaceutical DPIs, active particles, both in-flow and on surfaces, possess a bipolar charge distribution, which may influence their aggregation and deposition onto the large permeable membrane of the lungs. [117, 119, 120] A number of the experimental techniques developed to measure the electrostatic charge of powders [121–125] are based on the Faraday-well; a well-known method for measuring the net charge of bulk powders. However, with regard to DPIs, these measurements are often conducted in an uncontrolled environment, leading to limited reproducibility and insight into the electrostatic characteristics of dispersed aerosols, the dynamics of dose emission, and the effects of agglomeration. In particular, the net charge

of the powder does not provide information regarding the bipolar nature of the charge on individual particles or agglomerates, both of which directly affect particulate behaviour and consequently product performance.

It is currently understood that particles with an aerodynamic diameter of less than 5 μm are most likely to reach and deposit in the pulmonary regions of the lungs, but according to the literature particles with a diameter of 0.5 to 10 μm can still penetrate into the lungs.[126–128] The aerosolisation process within a DPI is understood to be complex, but is conventionally viewed as the dispersion of the powder dose into the air-stream and further separation of agglomerates largely due to shear forces, turbulence and wall collisions occurring before the powder has left the device. It is not typically viewed as a dynamic process of both de-aggregation and re-aggregation. The bipolar charge state of particles, following their transmission through a DPI, suggests that any aggregation is dominated by Coulomb forces as each drug dose released by a DPI consists of a wide range of particle sizes and charges. During in-flow collisions, the varied composition of a particle stream has been shown to promote additional attractive interactions at short separations, even between particles of the same sign of charge; the latter process being driven by polarisation effects. [49] In inelastic collisions, often present in fine powders, like-charged particles with the initial velocity sufficient to overcome the Coulomb barrier. As seen previously in this work and in [48, 49, 129], attractive interactions between like-charged particles can play a significant role in particle aggregation, sometimes leading to undesirable growth ('charge scavenging') prior to deposition. Previous analysis [48, 129] also indicates that collision velocity plays a key role in these inelastic, electrostatically driven aggregation processes.

A Dekati bipolar charge analyser BOLAR™ [130] was utilised to measure the net and bipolar charge distribution of aerosolised lactose (the primary ingredient in many DPIs) as a function of particle size, under controlled conditions of temperature and humidity. [131] In order to better understand the behaviour of charged particles in an emitted stream, the experimental measurements of

the BOLAR have been utilised in a computational model of agglomeration under conditions analogous to those present in a DPI. As such, many-body electrostatic methods, [17, 49] suitable for describing charge induced interactions including polarisation effects, combined with classical particle dynamics are able to simulate fine powder streams travelling through an inhaler or human airway. DPIs are highly diverse in design and operation - products with two or more active components (combination products) have recently proliferated. Some devices separate active components to either enhance product shelf life or to facilitate the manufacture of products with multiple variations in such combinations. These products may therefore have dual rather than single airflow paths within the device.

Possible outcomes of particle aggregation in single and dual stream devices have been analysed in this work, with the role of the larger highly charged particles -'potential scavengers' formed from carrier particles - investigated in detail. The nature of the charge scavengers has been described previously. [95, 132, 133] If such particles are present in a stream, even after the 'de-coating' precautions described in [132], then they may be able to re-adsorb smaller particulates. Simulations of this nature, supported by experimental data, could provide valuable insight for the development of inhalers designed with improved drug powder flow.

5.2 Dekati BOLAR™ measurements of charge in dry powders

In a Dekati BOLAR™, a collection of particles or droplets, e.g. a drug dose or drug analogue, may be aerosolised at a typical flow rate of 60 L/min and is split equally by the flow divider for aerodynamic size differentiation and filtration by the impaction stages (Figure 5.1a). The dose, now divided into six fractions, travels beyond the impaction stages and is separated by the bipolar charge

detection tubes; the inner detector (ID) surfaces are charged to +1kV, which attract negatively charged particles and the outer detector (OD) surfaces, held at ground potential, attract positively charged particles. Electrical signals from the particles interact with the corresponding detection surfaces such that the total positive and negative charge of a single size fraction can be measured, in addition to the total mass collected on each electrode. [130]
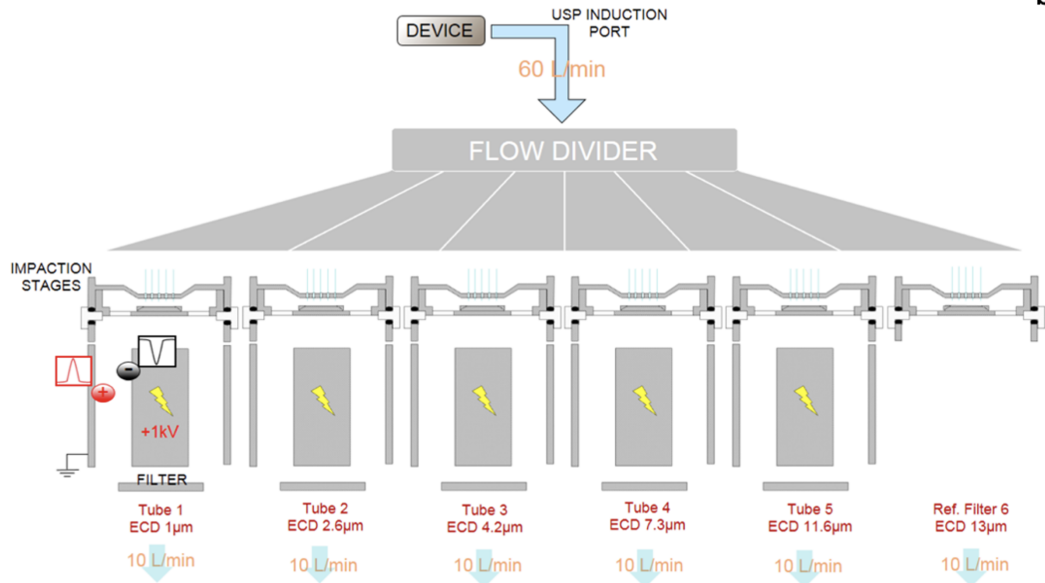
Figure 5.1: *Dekati BOLAR™ showing the effective cut-off diameter (ECD) of the particles collected in the detector tubes.*

Lactose-based DPI formulations, known to exhibit bipolar charge characteristics, have been used in these experiments. The total bipolar charge, measured in picoCoulombs, was observed to be largely comparable across a range of operating conditions.

Table 5.1: The size distribution and average radius of particles in five detector tubes of Dekati BOLAR™.

detector	radius range / μm	average radius, $\bar{a}$ / μm
1	$0.00 - 0.48$	0.24
2	$0.48 - 1.30$	0.89
3	$1.30 - 2.13$	1.72
4	$2.13 - 3.61$	2.87
5	$3.61 - 5.83$	4.72

Dose to dose variability of the total charge was also found to be similar across the detector tubes and formulations throughout the experiments. A small net positive charge was observed for the total charge covering all size ranges (detectors), due to an overall higher charge on the positive particles in comparison to that on the negative particles. Charge distributions similar to that observed and reported in table 5.2 have been presented previously. [134] Whilst other particles, such as carrier particles or scavengers, will be present in a DPI stream, these are less likely be included in the collected mass as they are usually too large to enter any size fraction of the apparatus.

Table 5.2: The mass, charge, and distribution of the particles collected by the outer (OD1 - OD5) and inner (ID1 - ID5) BOLAR™ detectors: $\bar{m}_d$ is the total average mass collected by a detector; $\bar{q}_d$ is the total average charge collected by a detector. The average mass of a particle, $\bar{m}_p$, is calculated using the average radius of a particle within a detector ($\bar{r}_p$, Table 5.1) and the density of lactose of 1.52 g/cm^3; n is the number of particles in a detector and $\bar{q}_p$ is the average particle charge.

	positively charged particles					negatively charged particles				
detector	OD1	OD2	OD3	OD4	OD5	ID1	ID2	ID3	ID4	ID5
$\bar{m}_d$ / μg	0.13	3.64	7.93	16.64	14.77	0.14	3.99	8.27	21.23	14.47
$\bar{q}_d$ / pC	29.54	510.9	337.7	325.5	156.9	-9.543	-462.2	-304.0	-297.8	-144.1
$\bar{m}_p$ / pg	0.0088	4.49	31.0	150	667	0.0088	4.49	31.0	150	667
$n, \times 10^3$	1477	811	255.8	111.1	22.1	1590.6	888.9	266.7	141.8	21.9
$\bar{n}$/%	26.44	14.52	4.58	1.99	0.40	28.47	15.91	4.77	2.54	0.39
$\bar{q}_p$ / fC	0.02	0.63	1.32	2.93	7.10	-0.006	-0.52	-1.14	-2.10	-6.58

The average mass of the collected particles is $\bar{m} = 91.21 \pm 5.91$ μg which is concentrated predominantly in detectors OD4 and OD5 (positive particles) and detectors ID4 and ID5 (negative particles). However, the average combined percentage of particles in the stream from detectors OD5 and ID5 is less than 0.8%, and from detectors OD4 and ID4 is less than 2.6% , as shown in Table 5.2. This suggests that the population of larger particles in the stream is negligible. Although detectors OD5 and ID5 contain particles of the largest size and the highest charge, the highest total average charge, $\bar{q}_d$, has been collected by detectors OD2 and ID2. This is due to a significant number of charged particles in the size range of 0.48

μm to 1.30 μm present in the stream (see Table 5.2). The experimental results also show that, numerically, the majority of particles in a DPI stream are of the smallest size, with an average radius of 0.24 μm, which constitute 26.4% of the positively charged stream and 28.5% of the negatively charged stream. Further details of the composition of each stream expelled from the DPI can be seen in Table 5.2.
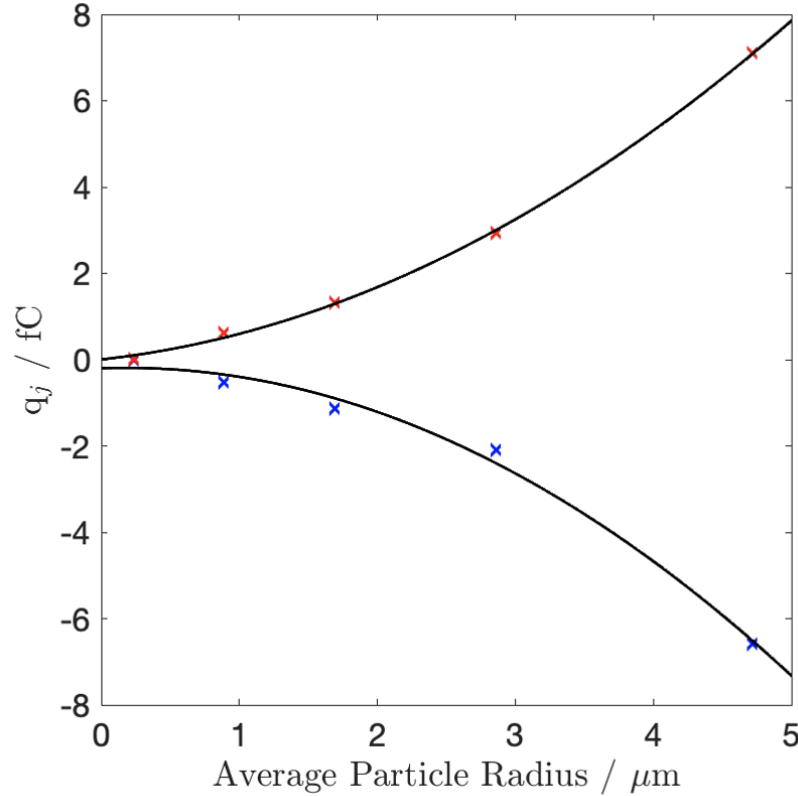
Figure 5.2: *The average particle charge as a function of the average particle radius calculated using the data presented in Table 5.2. The magnitude of charge on the positively (red crosses) and negatively (blue crosses) charged particles scales as the square the radius (solid line) with an R^2 of 0.99. For comparison, the scaling as radius cubed is shown by the dashed line.*

The charge on each particle, $\bar{q}_p$, has been estimated using the values for the overall collected charge, $\bar{q}_d$, and the number of particles collected on a detector, n. The results show that the absolute value of $\bar{q}_p$ scales with the square of the radius of a particle (last line in Table 2 and Figure 5.2). This suggests that charge resides on the particle's surface and no charge is present within the internal volume. In this work, we model the agglomeration of particles in the stream using a mathematical formalism [17] which accounts quantitatively for the surface charge and polarisation of particles during a collision.

5.3 Computational methodology and justification

In this work, the many-body framework outlined in chapter 2[17] has been used in conjunction with Verlet classical particle dynamics with an adapted NVE ensemble (constant number of particles, volume and energy) to study the effect of many-body electrostatic interactions within a stream; it was adapted such that energy could be lost during collisions. A single stream of DPI particles has been modelled as a collection of hard spheres with dimensions and charges described in Table 5.2, initially moving with a constant velocity v_{Stream} (Figure 5.3). Following earlier work [135], the particles were assigned a coefficient of restitution of 0.8 to allow for the energy loss via inelastic collisions. No interactions with the walls were considered as a DPI stream was assumed to be much narrower than human airways.

The interacting particles in a stream cause the induction of non-uniform surface charge distributions due to distance dependent many-body electrostatic interactions. Utilising the fast multipole method, as described in chapter 2,[17] these interactions can be accurately described at a linearly scaling computational cost with respect to the number of particles, and the solution yields the interaction energy, the surface charge distribution and the force acting on each particle. Lindgren *et al.* [49] shows that it is possible to combine such a solution with classical dynamics simulations to study the propagation of a many-body system of colliding particles as a function of time. The convergence of these solutions for the particulates studied here was found to occur at $\ell_{max} = 15$, and all simulations were carried out within this regime with a timestep of 0.01μs.

We first consider single collision events taking place in a stream, which had previously been shown to affect particle coalescence in air; for example, in the agglomeration of charged ice and dust particles in the mesosphere and lower thermosphere as in chapter 3. [94] In the collision scenarios considered in this work, a pair of particles form a cluster only if they carry opposite charge, and any like-charge aggregation as described in [136] is negligible as no stable state exists beyond the Coulomb barrier. As the BOLAR results show, the majority of particles emerging from a DPI
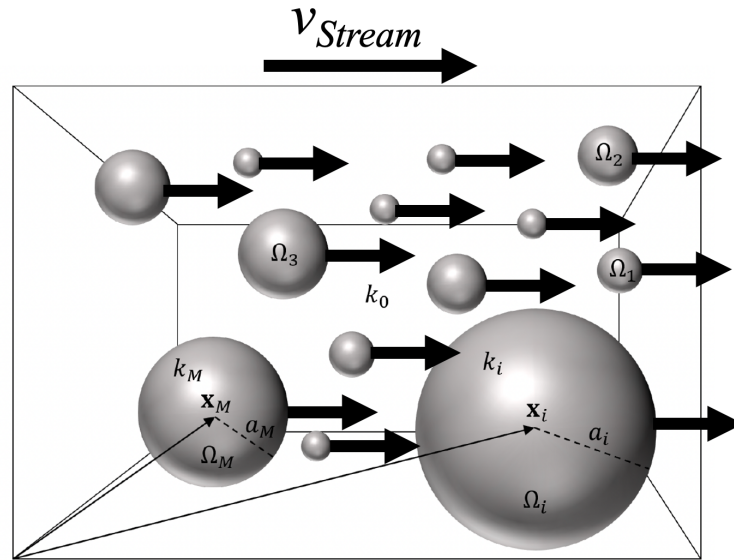
Figure 5.3: *Illustration of a typical single stream of particles moving with a constant initial velocity: a is the radius, Ω is the volume, and k is the dielectric constant of a particle. The interactions take place in vacuum $k_0 = 1$.*

are collected in OD1 and ID1 detectors, therefore clusters containing pairs of the smallest particles ($a < 0.48 \ \mu m$) are expected to be common.
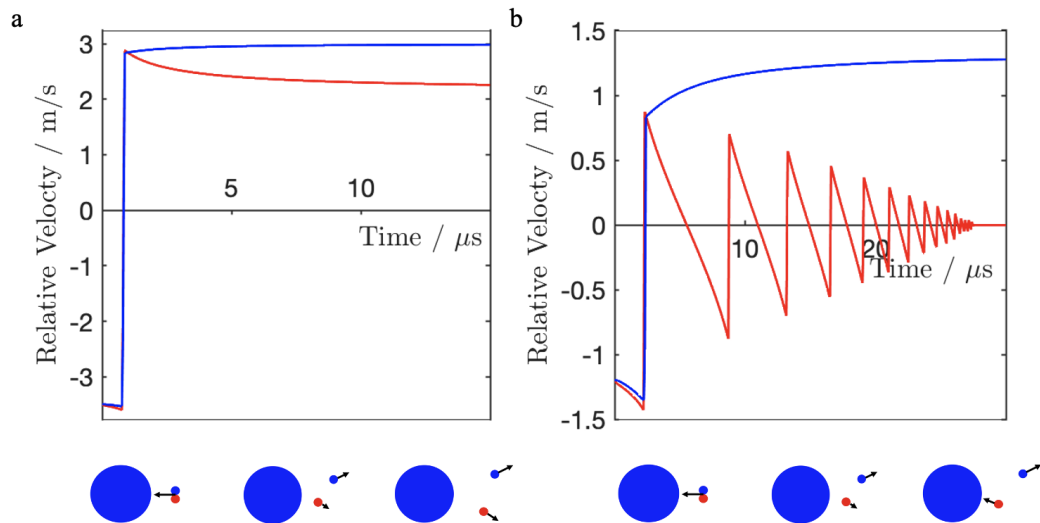
Figure 5.4: *Relative velocity as a function of time for a positive (red) and a negative (blue) particle in a small cluster colliding with the large negatively charged particulate: a) the incoming relative velocity is 3.5 m/s, b) the incoming relative velocity is 1.2 m/s. The cluster is composed of two particles of the smallest size fraction ($a_{+,-} = 0.24 \ \mu m$, $q_+ = 0.02 \ fC$, $q_- = -0.006 \ fC$); the large particle is typical of that identified in the ID5 detector ($a = 4.72 \ \mu m$, $q = -6.58 \ fC$).*

The dynamics of an interaction between a small cluster with one of the larger particles in a DPI stream is depicted in Figure 5.4 to highlight a potential scavenging mechanism [132] that could occur in the stream, given a flow rate of 60 L/min and

the particle parameters shown in Table 5.2.

The incoming relative velocity of a small cluster during a collision with a large particle plays a critical role in the dynamic behaviour. Collisions shown in Figure 5.4 destroy the small pair and provide a route to the formation of a larger bipolar cluster. This coalescence step could be critical in cluster formation in a DPI stream, making the product of the collision - a pair of oppositely charged particles with drastically different sizes - even more abundant than the original small pair.
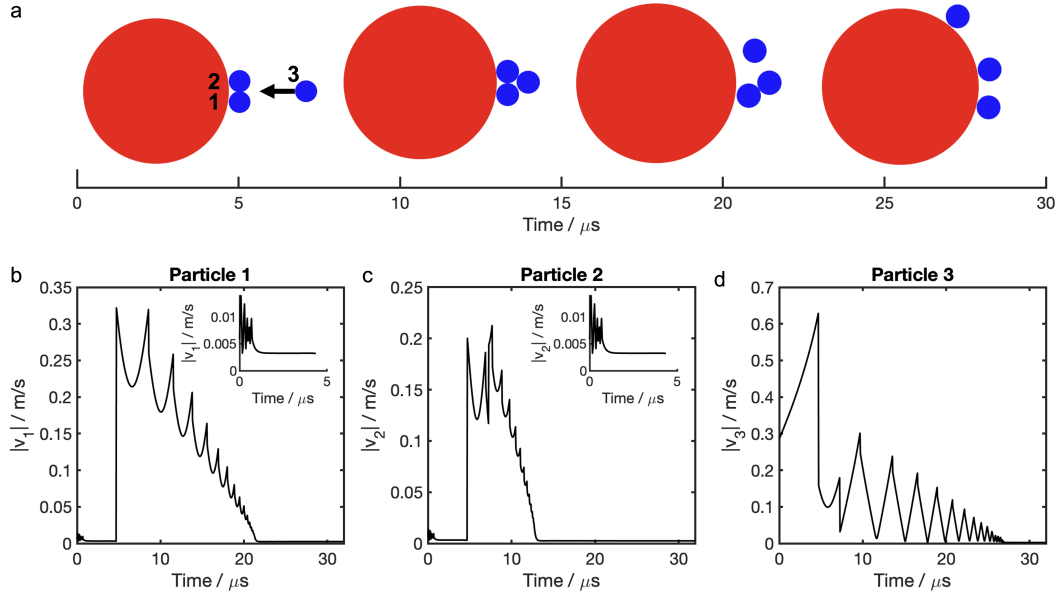
Figure 5.5: *The role of the large (lactose) particle (a = 4.72 μm, q = 7.10 fC) in scavenging smaller charged particles (a = 0.24 μm, q = -0.006 fC): a) snapshots of the particle dynamics simulation at 2μs, 8μs, 12.5μs, and 20μs, (b), (c) and (d) velocity of the smaller particles during the scavenging process. Particle 3 has initial relative velocity of 0.3 m/s. The insets in (b) and (c) depict the velocity for the first 5 μs seconds of the simulation. The red and blue depict positive and negative charge respectively.*

One pathway for the formation of individual triplets and quartets (clusters containing three or four particles, respectively) is shown in Figure 5.5. Two small negative particles 1 and 2 are stabilised initially on the surface of the large positively charged (lactose) carrier through the dissipation of kinetic energy in the first few microseconds of a simulation (inset in Figures 5.5b and 5.5c). The residual velocity at times shorter than 5 μs indicates a slow transition into a more stable configuration where the negative particles 1 and 2 move further apart. This relaxation process is orders of magnitude faster than the corresponding kinetic energy of the incoming particle 3, which has an initial absolute velocity of 0.3 m/s and then accelerates towards the

cluster driven by attraction to the highly charged large carrier.

Upon collision, particle 3 is also stabilised on the surface leading to further cluster growth. The incoming trajectory of this particle has been chosen to represent the most repulsive case and yet such a collision still leads to cluster growth. Given the correct conditions, this cluster growth process, known as charge scavenging, will persist in a DPI stream.

5.4 Cluster growth in a single stream

Particles of larger size occasionally enter a DPI stream. Initially, these large carriers (or charge scavengers) aid the smaller active pharmaceutical ingredients (API) in gaining the velocity and direction required for inhalation and release into the stream. Subsequently, they are often ejected through collisions with the walls before entering the mouth or trachea; [132] however, given the size and charge of the scavengers, [117, 126] further interactions between particles in the stream could lead to re-adsorption of the API onto the scavenger and prevent deposition into the lungs. To understand the mechanisms leading to re-adsorption of the API within a DPI stream, a more complete particle dynamics simulation of the stream containing potential charge scavengers has been undertaken.

The scavenging effect has been investigated using the computational setup described in chapter 2. In this computation, a charge scavenger passes at a speed of 6.5 m/s through a DPI cloud consisting of 300 particles each with a dielectric constant of 2.9 (100 negatively and 100 positively charged particles where $a = 0.24$ μm, 40 negatively and 40 positively charged particles where $a = 0.89$ μm, and 10 negatively and 10 positively charged particles where $a = 1.72$ μm). The simulation time has been increased to 200 μs. The size of the scavenger ($a = 10$ μm) corresponds to one of the smaller carrier particles found within a commercial DPI stream [126]. The relative velocity used in the simulation corresponds to a DPI flow of 60 L/min through an outlet of 1.4 cm in diameter. All interactions are assumed to take place in a vacuum (dielectric constant of 1) at room temperature, and random velocities are assigned to the stream particles following the Maxwell-Boltzmann distribution determined by collisions.
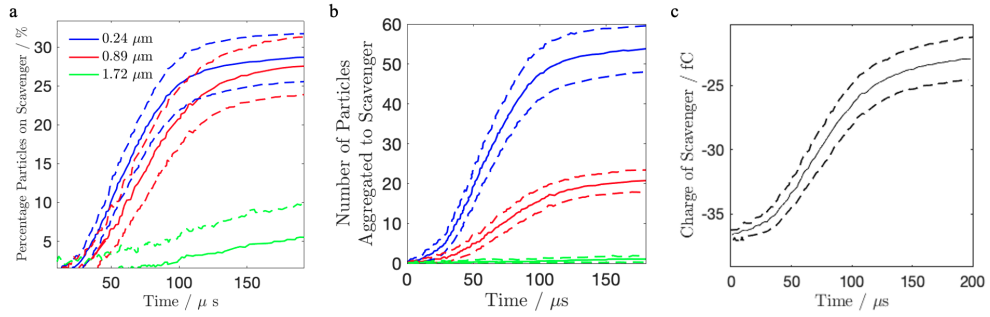
Figure 5.6: *Aggregation outcome for a scavenger (a = 10 µm, q = -38.5 fC) passing through a cloud containing 300 particles: 200 particles with a = 0.24 µm (blue), 80 particles with a = 0.89 µm (red) and 20 particles with a = 1.72 µm (green) showing the number of particles in a cluster (a) and the total accumulated charge (b). The population of each sized particles is equally bipolar.*

As Figure 5.6 shows, if a large particle is present within a stream a spontaneous aggregation of smaller API particles on the charge scavenger readily occurs, thus preventing the active API from reaching the lung membrane. For a negatively charged scavenger (q = -38.5 fC in this case), all the particles that aggregate onto the surface have positive charges. As figure 5.6 also shows, the majority of particles aggregated on the scavenger are of the smallest size fraction (Figure 5.6a), and the percentage uptake of 0.24 µm and 0.89 µm particles is similar. The aggregation rate is mainly determined by the change in the total charge of the scavenger (Figure 5.6b) as the added mass makes a very small contribution to its size. On average, 30 % of 0.24 µm and 0.89 µm particles and 10 % of 1.72 µm particle have been adsorbed onto the scavenger.

Figure 5.7 shows that if the charge on the scavenger is halved (q = -19.3 fC) half the amount of aggregation occurs within a stream. This decrease is due to a 2.5 times lower aggregation rate as compared to the case shown in Figure 5.6. The simulations also show that the aggregation outcome for a positively charged scavenger with q = 46.3 fC is halved in comparison to the data shown in Figure 5.6. The decrease in the amount of charge scavenging on the positive scavenger can be attributed to the skewed bipolar nature of the stream (see table 2). Positively charged particles that aggregate onto the negative scavenger (Figure 5.6) carry 3.5 times more charge than their negative counterparts. In larger streams, the shape of the agglomerates remains predominantly spherical (Figure 5.8a) as the scavenger continues to adsorb particles to its surface in size order - from smallest to largest - as seen by the gradients of
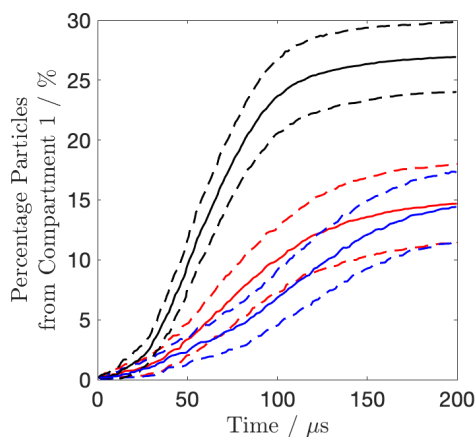
Figure 5.7: *A comparison of the percentage of OD/ID 1 (a = 0.24 μm) particles aggregated onto one of three scavenger particles over the entire 200 μs dynamic simulations; whereas scavenging particles with a = 10 μm I (q = −38.5fC, black) and II (q = −19.3fC, blue), and III (q = +46.3fC, red). Each plot shows the mean and standard deviation for the sample size.*

the curves in Figure 5.6. Other smaller assemblies are also formed, two of which are shown in Figures 5.8b and 5.8c. These clusters could also become too large to be adsorbed into the lungs, and their formation in the stream should be minimised.
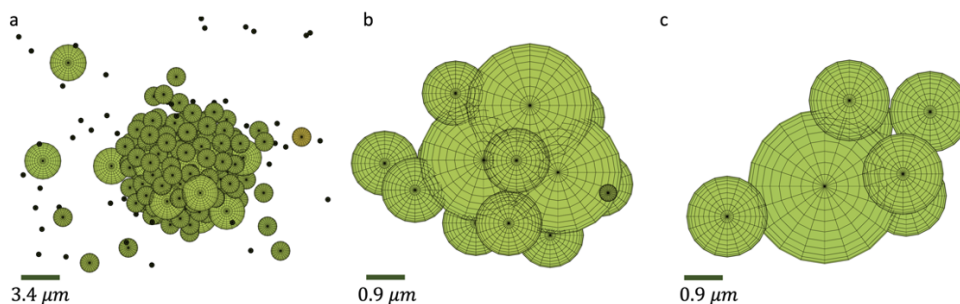
Figure 5.8: *Examples of large clusters formed in a single simulation of a DPI stream containing a charge scavenger and 1500 smaller particles (500 negatively and positively charged particles where a = 0.24 μm , 200 negatively and positively charged particles where a = 0.89 μm, and 50 negatively and positively charged particles where a = 1.72 μm. The simulation time is 200 μs.*

In conclusion, even for the smallest carrier particle used in dry powder inhalers (a = 10 μm), charge scavenging may cause re-adsorption of API particulates and reduce the required amount of the API during inhalation leading to the use of higher doses. This effect will be even more pronounced for the larger carriers. As charge scavenging has been shown to remove more than a quarter of the stream particles of smaller size fractions, the elimination of charge scavengers from the DPI stream before entering the mouth/trachea should be considered. Additionally, reducing the

rate of higher energy collisions between particles would help to avoid the formation of larger clusters shown in Figures 5.8b and 5.8c.

5.5 Possible solutions to reducing charge scavenging: dual stream

In order to prevent particles from becoming too large to permeate the lung membrane, one may consider altering the stream configuration to reduce the high energy collisions and charge scavenging and to manipulate the size range of the particles in the stream. Multiple propulsions of less dense streams could also reduce the number of collisions and hence clustering. This can be realised in two adjacent DPI streams composed of particles of the smallest three size fractions and directed towards the target at a small angle. A simple schematic of such a design can be seen in figure 5.9.
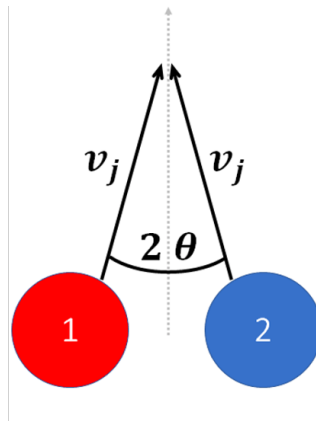
Figure 5.9: *Definition of the angle (2θ) between stream 1 (red) and stream 2 (blue) for two streams angled equally (by θ in opposing directions) towards a common target perpendicular to their midpoint, where each stream has a velocity such that the speed of each flow is the same magnitude ($|\nu_{stream}| = |v_j|$).*

Dual stream dynamics has been investigated for two streams of particles representing the three smallest radii. The two streams were directed at a target at a 6° angle and with a velocity of 6 m/s. These simulations were carried out under the same conditions as described in the previous section. In the dual stream, particle growth appears to be significantly reduced, as shown in Figure 5.10. The majority of particles do not aggregate, with only about 6% of particles forming clusters after

100 μs of simulation time; a significant reduction in comparison to 25% in the case of a single stream (Figure 5.6).
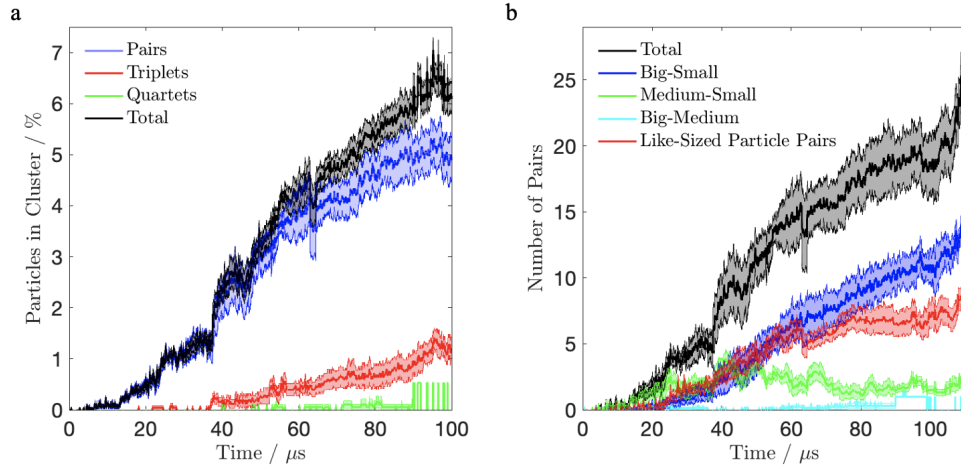
Figure 5.10: *Composition of the dual stream averaged over 10 runs, initially containing 125 negatively and positively charged particles where a = 0.24 μm, 50 negatively and positively charged particles where a = 0.89 μm, and 13 negatively and positively charged particles where a = 1.72 μm. The stream are directed at the target at 6° angle. The stream contains a) pairs (blue), triplets (red), quartets (green), and the total percentage of particles in clusters is shown in black; b) the aggregated pairs are big-small with a_1 = 1.72 μm, a_2 = 0.24 μm (blue), medium-small with a_1 = 0.89 μm, a_2 = 0.24 μm (green), big-medium with a_1 = 1.72 μm, a_2 = 0.89 μm (cyan), like-sized particles (red), alongside the total number of pairs is shown in black. The shaded regions indicate the standard error of the obtained results.*

Particles that do form clusters in the dual stream are typically organised in pairs, with some small presence of triplets and even fewer instances of clusters containing four particles. The aggregated pairs frequently feature the attachment between a larger particle and a smaller particle (Figure 5.10b). A small contribution from surface polarisation effects, fully accounted in the computational setup as shown in Supporting Information, is expected to increase the stability of the pairs containing dissimilar size particles compared to like-size configurations. [136] All pairs were found to contain oppositely charged particles, as expected, given the bipolar nature of the stream and low polarisability of the constituent particles. Triplets formed in the stream are composed of one larger particle and two smaller particles with charge opposite to that of the larger particle, similar to the initial geometry shown in Figure 5.5. The rarely occurring quartets are formed following the mechanism described in Figure 5.5. This shows that although charge scavenging is limited in the dual stream, it still occurs. Given that the majority of particles emerging from

an API are very small, the conclusions cited in reference [126] would suggest their aggregation into larger units could be beneficial providing the final particle remains smaller than 10 μm in diameter.

5.6 Conclusions

In summary, our simulations have shown that using two or more streams aimed at a common target and filtering out charge scavengers could enable more efficient drug delivery for users of DPI. Within a single stream a charge scavenger present can re-adsorb up to 25% of API particles, hence reducing the API reaching the lungs. An inhaler designed more than one stream and a smaller size range of particles has been shown to limit aggregation growth over a similar time period such that all the particles formed could reach the lungs and as such, the aerosolisation process in DPIs is shown here to be a dynamic combination of both deaggregation and reaggregation. The development of efficient DPI products has historically focused on maximising deaggregation. This study has shown the importance of also minimising reaggregation.

Chapter 6

Casimir Force in Layered Materials and Control of the Stable Equilibrium

6.1   Introduction

A visionary theoretical prediction, known as the Casimir effect, [31] that two uncharged dielectric or conducting interfaces experience an attractive interaction at very close separations is purely quantum mechanical in nature, as discussed in section 1.3. It stems from the permanent existence of fluctuating fields on either side of a nanometre-size cavity created between the interfaces, which are present even in a perfect vacuum and can be suppressed or enhanced inside the cavity. Whilst free space outside the cavity is filled with a continuous sequence of electromagnetic fluctuations at all wavelengths, inside a Casimir cavity only fluctuations at half-integer wavelengths are present (these are defined by the separation distance between the interfaces) and the fluctuations at longer wavelengths get pushed out. This creates a slight discrepancy in the energy density inside and outside the cavity and, if the interfaces are made from the same material, a net attractive force is produced which is independent of the exact shape of the interacting bodies and their dielectric properties. [137]

Due to the lack of sophisticated instrumentation capable of measuring these subtle

changes at such close separations, the Casimir effect remained experimentally elusive for almost 50 years, drawing little interest outside the theoretical community. With the first unambiguous measurements by Lamoreaux in 1997, [138] experimental evaluations of the attractive Casimir force between metal plates and spheres have become more common and have been realised in a range of geometries. [139–141] Despite many subsequent measurements of the attractive Casimir force in cavity quantum electrodynamics, physical interpretation of this important nanoscale effect is often lacking in the literature.

The Lifshitz theory of van der Waals forces [142] states that the Casimir force can change from attractive to repulsive through a suitable choice of interacting materials immersed in a fluid. First experimental evidence confirming the general Lifshitz theory was reported by Munday *et al.* [37] They showed that repulsive Casimir interactions can be also realised and measured if the walls of the cavity are composed of materials with different dielectric response functions, ϵ_1 and ϵ_2, when the dielectric response function of the medium, ϵ_m separating the walls satisfies the following criterion

$$\epsilon_1 > \epsilon_m > \epsilon_2. \tag{6.1}$$

Although the measured repulsive force was found to be weaker than the attractive one, the magnitude of both forces increases with decreasing surface separation, in a complete agreement with the Lifshitz theory. The existence of repulsive Casimir–Lifshitz force has been further confirmed, and several interesting experimental setups provided to probe these repulsive interactions [43, 143–147] and optical properties of the interfaces. [148]

The various possible applications of the Casimir effect have become apparent with the rise of research in plasmonics and metamaterials, in which the Casimir force has shown to be manipulated and investigated at the level of accuracy and versatility inaccessible to conventional surfaces. [149–154] Nanopatterning of metallic surfaces opens up opportunities for exploring novel phases that emerge at the interfaces affected by the Casimir force. [155–157] The Casimir effect can also be exploited in this regard to deliver room temperature, low cost precision measurements conducted in the deep sub-micron regime. The developments of micro- and nano- electrome-

chanical systems will probe the existence of repulsive and zero Casimir forces and make these measurements imminently possible. [140, 158–162]

In the era of miniaturisation of integrated electronic devices, unlocking the potential of the Casimir force in practical quantum measurements can not be underestimated. However, this progress depends on our ability to control the Casimir effect and requires the fine tuning of the attractive and repulsive interactions, leading ultimately to a high-precision manipulation of the Casimir equilibrium. For example, the switch between attraction and repulsion has been realised in external magnetic fields in ferrofluids. [163, 164] Whilst the nature of the Casimir force can be controlled via external perturbations, the force - distance profile is largely defined by the materials involved. Experiments by Zhao *et al.* [165] achieved a stable Casimir equilibrium for a gold nanoplate suspended in ethanol above a Teflon-coated gold surface (quantum entrapment of the nanoplate at a fixed height above the surface). Note that if the permittivity relation in equation 6.1 is satisfied, two interfaces repel at all separation distances, as also demonstrated by the measurements of the repulsive Casimir force between Teflon and gold surfaces in cyclohexane. [43, 143]

These systems, and their superpositions, are investigated here by quantitatively accurate predictions of the Casimir effect in layered materials of increasing complexity, with evidence to show that in some instances the Casimir force can be made repulsive by a simple manipulation of the order of the layers. Given the excellent agreement of our calculations with existing experimental data for a range of complex systems, this formalism is utilised to propose layered systems suspended in a range of media that exhibit both attractive and repulsive Casimir effects thus allowing for a fine control of the equilibrium separation and quantum entrapment. A better understanding through quantitatively accurate experimental and theoretical predictions will bring us closer to achieving a full dynamic control over this interesting and indispensable phenomenon.

6.2 Fundamental concepts behind the methodology

Quantum mechanical formalisms of the Casimir interactions [165–167] are principally different to the description of weak intermolecular forces, given the nanometre dimensions of the quantum cavity formed between the interfaces and the nature of the interactions taking place. Following Parsegian [166], two interacting surfaces A and B are modelled as two half-spaces separated by a medium with the dielectric function, $\epsilon_m(i\xi_n)$, and thickness, ℓ, as shown in figure 6.1.
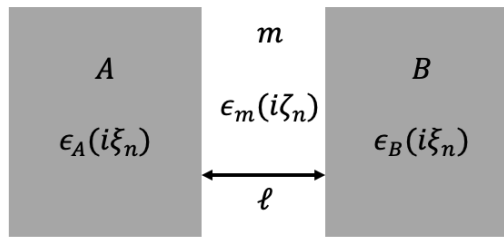
Figure 6.1: *Two semi-infinite half spaces A and B, separated by a distance ℓ: (top) bulk materials A and B described by the complex dielectric functions $\epsilon_A(i\zeta_n)$ and $\epsilon_B(i\zeta_n)$ at the complex Matsubara frequency.*

In the non-relativistic limit, the Casimir interaction free energy (per unit area) can be defined in terms of the summation of the free energies of the allowed surface modes, n, of the fluctuating electric fields as

$$G(\ell, i\xi_n) = \frac{kT}{2\pi c^2} \sum_{n=0}^{\infty} \epsilon_m(i\xi_n)\xi_n^2 \int_1^{\infty} p \ln[D(\ell, i\xi_n)]dp \qquad (6.2)$$

where k is the Boltzmann constant, T is the temperature, c is the speed of light, as discussed in section 1.3.[166] The dielectric function of a material, $\epsilon(i\xi_n)$, is defined at the relevant Matsubara frequencies

$$\xi_n = \frac{2\pi n kT}{\hbar}, \qquad (6.3)$$

where $\hbar$ is the reduced Planck constant, and the Matsuabra frequencies correspond to the energies at which thermal agitation leads to charge fluctuation, as can be seen by a simple rearrangement of equation 6.3.

The function $D(\ell, i\xi_n)$ includes the dielectric properties of the boundaries Am and Bm as

$$D(\ell, i\xi_n) = (1 - \Delta_{Am}(i\xi_n)\Delta_{Bm}(i\xi_n)e^{-2\rho_m \ell}), \tag{6.4}$$

$$\rho_m = \frac{\sqrt{\epsilon_m(i\xi_n)}\xi_n}{c}p$$

where $1 \leq p < \infty$; $\Delta(i\xi_n)$ varies depending on the geometry of the problem and, in the simplest case of a single composition half-space, it takes the following form for the surface A

$$\Delta_{Am} = \frac{s_A \epsilon_m - s_m \epsilon_A}{s_A \epsilon_m + s_m \epsilon_A}, \tag{6.5}$$

$$s_A = (p^2 - 1 + (\epsilon_A/\epsilon_m))^{1/2}, \quad s_m = p$$

where $\epsilon_A = \epsilon_A(i\xi_n)$ is the dielectric function of the surface A at a given complex frequency $i\xi_n$ and s_A is the corresponding component of the radial wave vector at the same frequency. The complex frequency is a result of the consideration of exponential behaviour of the frequency, accounting for loss/dissipation. A separate expression for Δ_{Bm} is derived by replacing A for B in equation (6.5).

As the summation in equation (6.2) is taken over positive values of n only, the $n = 0$ term needs to be multiplied by $1/2$ to avoid double counting of this term. As commonly accepted [37, 143, 165, 168], the magnetic dependence of the Casimir energy is neglected here and it is assumed that the relative magnetic permittivity of the interacting materials is unity (all materials studied here are non-magnetic). However, a rigorous procedure for calculating the Casimir attraction with arbitrary magnetic and dielectric properties using the Minkowski energy–momentum tensors can be found in Ellingsen *et al.* [169]

Some accurate oscillator models [166, 167] calculate $\epsilon(i\xi)$ directly, where the dielectric function takes the general form of

$$\epsilon(i\xi) = 1 + \sum_l \frac{d_l}{1 + \xi\tau_l} + \sum_k \frac{f_k}{\omega_k^2 + g_k\xi + \xi^2}. \tag{6.6}$$

The oscillator form of equation (6.6) considers a damped harmonic oscillator model, where the first summation (over l) describes the Debye dipolar relaxation; τ_l is the relaxation time, and d_l is analogous to the oscillator strength. Higher order frequency terms are accounted for in the second summation (over k) in a damped - oscillator form. The constants f_k and g_k in equation (6.6) have been determined for many well studied materials and have shown excellent agreement with the literature. [166, 167]

Alternative oscillator models include [143]

$$\epsilon(i\xi) = 1 + \sum_l \frac{C_l}{1 + (\xi/\omega_l)^2} \tag{6.7}$$

where ω_l is the resonance frequency and C_l is the oscillator strength. In this study, oscillator models (6.6) and (6.7) have been used along with the recently optimised oscillators by Gudarzi and Aboutalebi [170], which have been shown to accurately reproduce experimental results.

The formalism of [166], describing the Casimir effect, has been adopted here to describe the interactions between materials with multiple layers of arbitrary thickness. Sernelius [171] proposed an alternative solution for calculating the Casimir effects in systems containing two-dimensional (2D) layers such as graphene and 2D electron gases. Tomaš [172] extended the Lifshitz formalism to account for the presence of layered media.
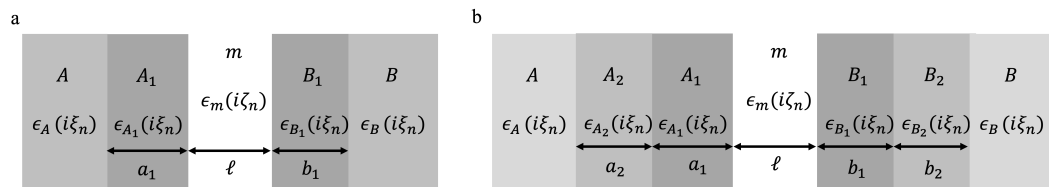
Figure 6.2: *Schematic of two semi-infinite half spaces A and B with a layer A_1 and B_1 of thickness a_1 and b_1 atop each material forming a cavity of size ℓ (a), and with two added layers, A_1 and A_2, B_1 and B_2, of the corresponding thickness a_1 and a_2, b_1 and b_2 (b), where all materials are described by their corresponding complex dielectric functions $\epsilon_A(i\zeta_n)$ and $\epsilon_B(i\zeta_n)$.*

If a layer A_1 with thickness a_1 is added to the interface described by the half-space A, then Δ_{Am} in equation (6.4) is transformed to $\bar{\Delta}_{Am}$ as follows

$$\bar{\Delta}_{Am} = \frac{\Delta_{AA_1} e^{-2\rho_{A_1} a_1} + \Delta_{A_1 m}}{1 + \Delta_{A_1 m} \Delta_{AA_1} e^{-2\rho_{A_1} a_1}} \tag{6.8}$$

where

$$\rho_{A_1} = (\rho_m^2 + (\xi_n/c)^2 (\epsilon_{A_1} - \epsilon_m))^{1/2}.$$

Adding another layer, A_2, with the thickness of a_2 (Figure 6.2) requires Δ_{AA_1} in equation (6.8) to be replaced with

$$\frac{\Delta_{AA_2} e^{-2\rho_{A_2} a_2} + \Delta_{A_2 A_1}}{1 + \Delta_{AA_2} \Delta_{A_2 A_1} e^{-2\rho_{A_2} a_2}} \tag{6.9}$$

The subsequent addition of layers proceeds by induction so that with each added layer the functions Δ_{AA_i} get transformed as

$$\frac{\Delta_{AA_{i+1}} e^{-2\rho_{A_{i+1}} a_{i+1}} + \Delta_{A_{i+1} A_i}}{1 + \Delta_{AA_{i+1}} \Delta_{A_{i+1} A_i} e^{-2\rho_{A_{i+1}} a_{i+1}}}. \tag{6.10}$$

Once again, similar expressions need to be derived for the surface B.

The form (6.2) for the Casimir interaction free energy is convenient for obtaining the Casimir force numerically, as the differential with respect to the cavity size, ℓ, following $F(\ell) = \mathrm{d}G(\ell)/\mathrm{d}\ell$. However, in earlier experimental works the Derjaguin approximation has been widely used to relate the Casimir energy and force. [37, 143, 165–168, 170] In atomic force microscopy (AFM) and surface force apparatus (SFA) experiments, the Casimir force is often scaled to reduce the problem to a sphere - plane solution (in AFM) or a perpendicular cylinder - cylinder solution (in SFA) as follows [166–168]

$$F_{sphere-plane}(\ell) = F_{cyl \perp cyl}(\ell) = 2\pi R_{eff} G(\ell). \tag{6.11}$$

Here, R_{eff} is the radius of the sphere or cylinder, or $\sqrt{R_1 R_2}$ if the cylinders are of a different size. The Derjaguin approximation (as shown in equation 6.11) can be used in cases where the interaction is purely repulsive or attractive, however, in more sophisticated scenarios where the Casimir equilibrium is established its treatment can be non-trivial, such as in quantum entrapment experiments given the planar nature of Zhao *et al*'s work.[165]

In the following, the changing nature of the Casimir effect in layered materials is investigated, and it is shown that the control of the Casimir equilibrium can be achieved by simple compositional changes in the layered materials and the medium. A rigorous testing of the methodology using a variety of experimental setups reported in the literature is also presented. All calculations were performed using MATLAB and associated solvers [173] using the tolerance of 10^{-6}, as deemed appropriate through benchmarking the convergence of the Casimir energy using equation (6.2). The value n of the surface modes of the fluctuating electric field was set to 2^{12} to achieve 1% convergence of the energy within the $n \to \infty$ limit, however higher n will be required for systems with four layers and more.

6.3   Results and discussion

Munday *et al.* [37] used AFM to demonstrate the effect of the dielectric function of the interacting surfaces and medium on the overall Casimir interaction. They presented two examples: attractive Casimir force acting between two gold interfaces (Au AFM tip - Au surface) and repulsive Casimir force between gold and silica interfaces (Au AFM tip - SiO_2 surface), both measured in bromobenzene (see Figure 6.3). The interaction energy for these systems was then evaluated utilizing oscillators to describe the permittivity as defined by van Zwol *et al.* [143]. The Derjaguin approximation was then applied, as in [37], to evaluate the Casimir force. Figure 6.3 shows excellent agreement, within the experimental error, between our computational predictions and the experiments of Munday *et al.* [37] down to the surface separation distances of 20 nm. Some deviation from experiment at these very short separations is to be expected as retardation effects are not accounted for.

Previously, Ederth [167] also reported a strong attractive Casimir force (of the order
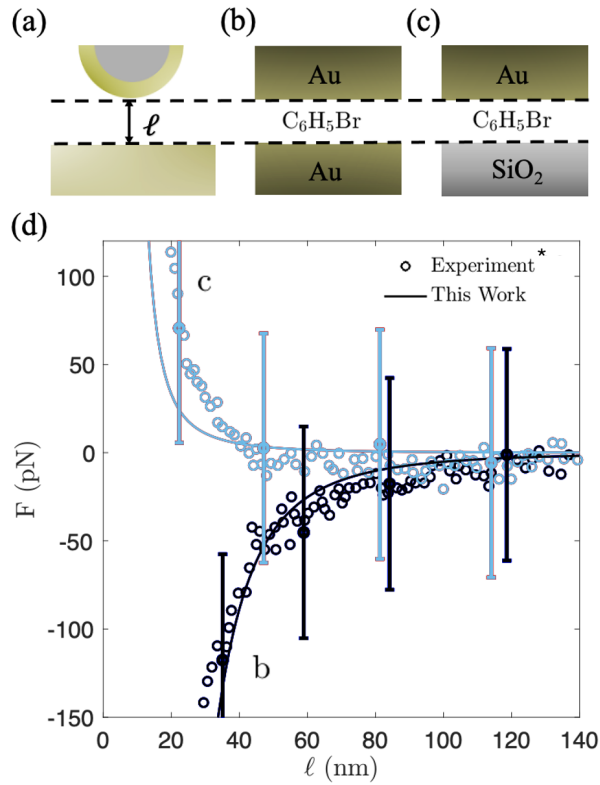
Figure 6.3: *The Casimir force acting between single layer interfaces in bromobenzene; (a) Illustration of AFM experiment computational setup (planar surfaces), (b) Au - Au interface, (c) and Au - SiO$_2$ interface, and (d) the Casimir force as a function of the separation distance (d) showing the results of the experimental AFM measurements [40] (open circles) and calculated in this work (solid line) using equation (6.2) and the Derjaguin approximation (equation 6.11).*

of μN per metre) measured in air between two identical gold surfaces with a more complex double layer structure containing a hydrocarbon layer on top of gold. These measurements were carried out using SFA illustrated in Figure 6.4a. The two perpendicular cylinders with radius of $R_{eff} = 2$ cm were coated with a gold layer of 200 nm thickness and a thin $a_1 = 2.1$ nm overlayer of hydrocarbon (hexadecanethiolate) (Figure 6.4b). The Casimir interactions in this double-layer system were calculated by representing the cylinders as semi-infinite gold half-spaces with a hydrocarbon layer on top. The dielectric functions for gold and hydrocarbon are taken from references [166] and [167], respectively. Our calculations, shown in Figure 6.4c, are in excellent agreement with the measurements [167], in which the Casimir forces were used to estimate the surface roughness.

Generally, the Casimir force between two ideal parallel conducting interfaces is proportional to the cross-sectional area of the interfaces, and it varies with the separa-
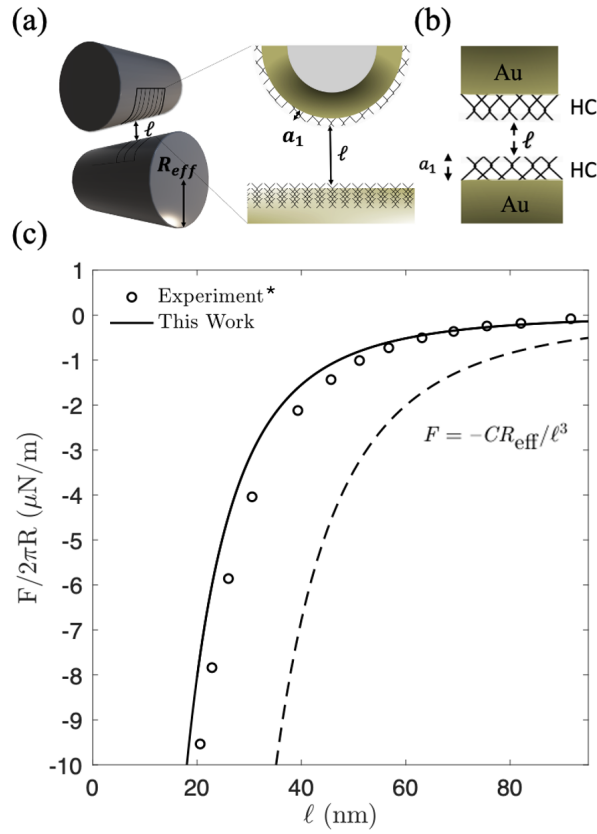
Figure 6.4: *The Casimir force acting between double layer Au - hydrocarbon interfaces in air. Illustration of SFA experiment (a); computational setup (b); the Casimir force as a function of the separation distance (c) showing the results of the experimental SFA measurements [168] (open circles), calculated in this work (solid line), and the case of two ideal conductors (dashed line).*

tion distance as $F(\ell) \propto 1/\ell^4$. Apart from this, the force depends only on fundamental values such as Planck's constant and the speed of light. Following the Derjaguin approximation as in 6.11, the geometry of Ederth's experiments [167] can be, in principle, reduced to a sphere - plane solution in which the Casimir force is defined as $F = -CR_{eff}/\ell^3$, where $C = \pi^3 \hbar c/360$. However, the approximation of ideal conductors is not accurate at short separation distances (see Figure 6.4), despite being widely used in earlier works in the field. [138, 174, 175] It is also worth noting that the calculations carried out in this work show an even larger discrepancy with the limiting case of two perfect conducting plates than that demonstrated by the dashed line in [167].

The quantitatively accurate computational method presented here makes it possible to discuss more delicate scenarios where the attractive and repulsive Casimir forces are kept in balance and a stable equilibrium is maintained. This has been demon-

strated recently by Zhao *et al.* [165] who reported a stable equilibrium, maintained by the Casimir forces, in which a thin, μm-wide gold flake suspended in ethanol (EtOH) was trapped at a fixed height above a double-layer surface composed of gold and a thin overlayer of polytetrafluoroethylene (PTFE). In this case, the equilibrium (quantum trapping) is maintained by competing short-range repulsion between the gold flake and PTFE and long-range attraction between the gold surfaces. The double layer PTFE - Au interface was also utilised to investigate quantum trapping of the gold flake whilst varying the thicknesses of the PTFE overlayer. A linear relationship was established to show that in EtOH the equilibrium trapping distance remains approximately half the thickness of the PTFE layer. [165]
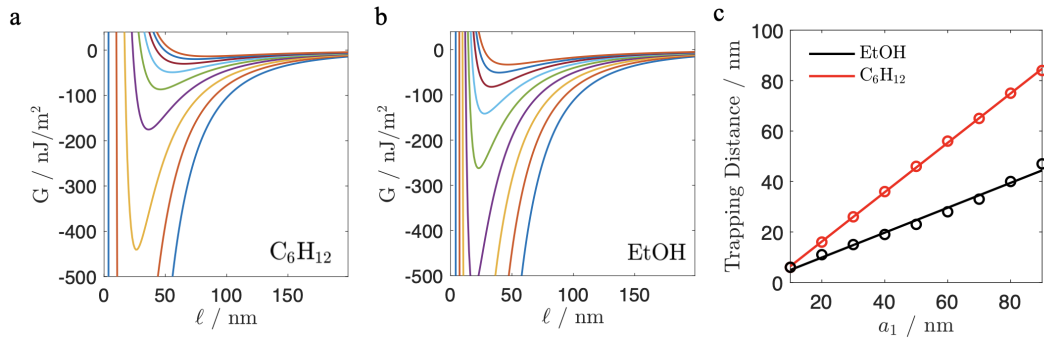
Figure 6.5: *The interaction energy, per unit area, as a function of the separation, ℓ, between gold surface and a PTFE - gold double layer in cylcohexane (a) and ethanol (b). The thickness of the top PTFE layer is 10 nm (blue), 20nm (red), 30 nm (yellow), 40 nm (purple), 50 nm (green), 60 nm (light blue), 70 nm (maroon), 80 nm (dark blue) and 90 nm orange. The minimum of each energy curve in (a) and (b), defined as the trapping distance, is shown in (c) as a function of the thickness, a_1, of PTFE overlayer (a_1) for ethanol (black) and cyclohexane (red).*

Excellent agreement was found with both the AFM and Fabry-Perot experiments [165] confirming not only the presence of the stable equilibrium but also the observed relationship between the equilibrium trapping distance and thickness, a_1, of the top PTFE layer (Figure 6.5c black line). Figure 6.5c also shows that the equilibrium trapping distance in cyclohexane will be close to the thickness of the PTFE layer (red line). For example, for $a_1 = 50$ nm, the equilibrium separation between a Au surface and a double layer PTFE - Au interface is $\ell_{eq} = 23$ nm in EtOH and $\ell_{eq} = 46$ nm in cyclohexane.

Generally, the rate of increase of the equilibrium separation with the thickness of the top PTFE layer doubles in cyclohexane, as indicated by the gradient of the

straight lines in Figure 6.5 of 0.98 (± 0.014) for cyclohexane (solid line) and 0.49 (± 0.047) for EtOH (dashed line) and the location of the minima in figures 6.5a and b. This conclusion is also supported by the observations of Van Zwol and Palasantzas [143] that in cyclohexane the repulsion between gold and PTFE interfaces doubles compared to that in ethanol. It is interesting to note that if the PTFE layer is only 10 nm thick both lines converge at the same equilibrium separation of 6 nm. The Casimir interaction energy profiles from which the data in Figure 6.5c was extracted can be seen in Figure 6.5a and b, with a specific example shown in figure 6.6.
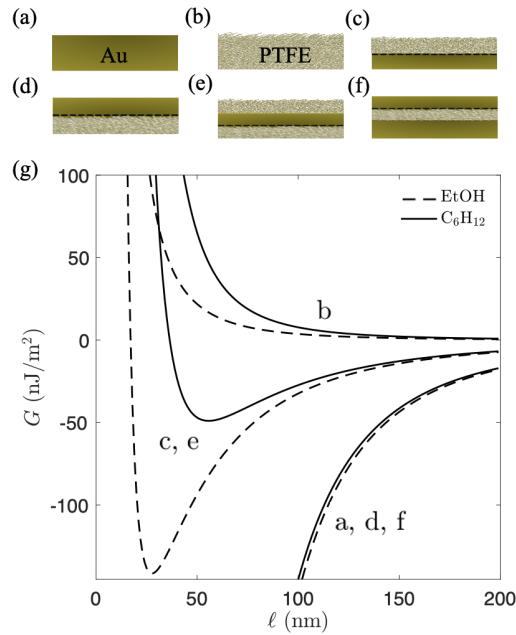
Figure 6.6: *The Casimir interaction free energy, per unit area, as a function of the separation distance (g) between gold surface and a range of interfaces (a-f) in ethanol (dashed line) and cyclohexane (solid line) calculated using equation (6.2). The thickness of the layers are $a_1 = 60$ nm (c), $a_1 = 10$ nm (d), $a_1 = 60$ nm and $a_2 = 90$ nm (e), $a_1 = 70$ nm and $a_2 = 90$ nm (f). The oscillator models are taken from [171].*

Figure 6.6 gives a general overview of our computational predictions for the Casimir interaction energy, G, as a function of the separation distance, ℓ, between the gold surface and a range of other interfaces with an increased layer complexity, which are shown in Figures 6.6 (a-f). These interactions take place in ethanol and cyclohexane. It is shown that in the experimental setup of Zhao *et al.* [165] (case (c), dashed line in Figure 6.6), where the top PTFE overlayer is 60 nm thick, a stable equilibrium in ethanol is formed at $\ell_{eq} = 28$ nm. The interaction energy in this case is not affected by the number of layers (compare cases (c) and (e), which give the same results in

both solvents), and it is independent of the thickness of the gold layer. Note that pure PTFE bulk repels gold surface at all separation distances (case (b)).

Furthermore, if the PTFE and gold layers are swapped so that the gold layer is on top of a double- or triple- layer material (cases (d) and (f) in Figure 6.6), only attractive interactions can be established, identical to the case (a) of two pure gold surfaces. Once again, despite the layer thickness being explicitly present in the formalism, the strength of the attractive Casimir interaction in the case of gold-terminated interface does not change with the thickness of top layer (calculations were ran in the range of 10 nm to 1 μm). Figure 6.6 also shows that changing solvent to cyclohexane would double the equilibrium separation between gold and a PTFE - gold double layer interface as well as between gold and a PTFE - gold - PTFE triple layer interface (cases (c) and (e), solid line in Figure 6.6). As a result, the Casimir interaction energy at the equilibrium is about three times weaker than in ethanol.
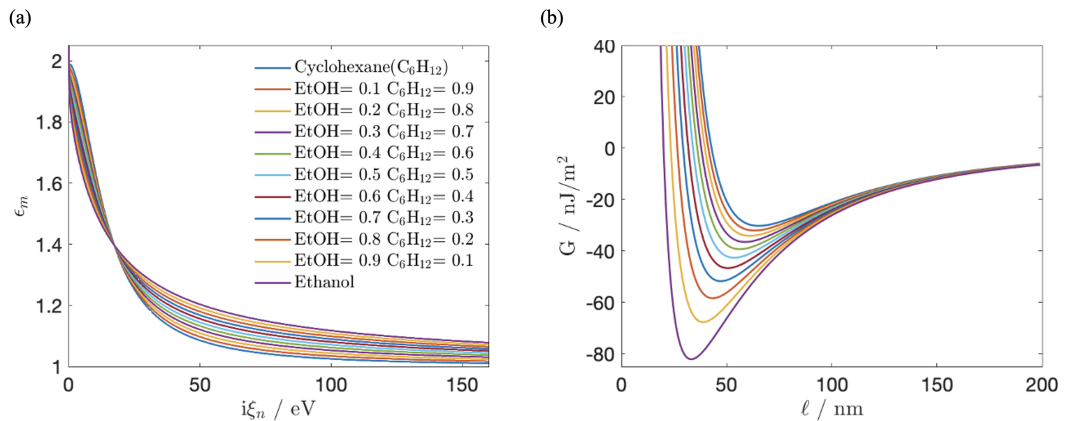
Figure 6.7: *(a) The dielectric functions calculated as a combination of the oscillator models describing cyclohexane and ethanol as a function of $i\xi_n$; cyclohexane is illustrated by the dark blue line (0:1), pure ethanol is depicted by the purple line (1:0), with the intermediate cases labelled accordingly. (b) The interaction energy, per unit area, between gold surface and a PTFE - gold double layer (the thickness of PTFE $a_1 = 70$ nm); EtOH = 0.1 C_6H_{12} = 0.9 (red), EtOH = 0.2 C_6H_{12} = 0.8 (dark yellow), EtOH = 0.3 C_6H_{12} = 0.7 (purple), EtOH = 0.4 C_6H_{12} = 0.6 (green), EtOH = 0.5 C_6H_{12} = 0.5 (light blue), EtOH = 0.6 C_6H_{12} = 0.4 (maroon), EtOH = 0.7 C_6H_{12} = 0.3 (dark blue), EtOH = 0.8 C_6H_{12} = 0.2 (orange) and EtOH = 0.9 C_6H_{12} = 0.1 (yellow). PTFE and EtOH were modelled using oscillators taken from [167], with gold modelled using an oscillator taken from [171].*

Given the great difference in the dielectric constants of ethanol ($\epsilon = 24.3$) and cyclohexane ($\epsilon = 2.02$), it is encouraging to see that a strong stable Casimir equilibrium and quantum trapping can be established in a variety of solvents.

Using the dielectric functions of ethanol and cyclohexane as the upper and lower

bounds for the known substances that could enable quantum entrapment, it is possible to consider additional dielectric functions that could also enable quantum entrapment as a summation ϵ_{EtOH} and $\epsilon_{C_6H_{12}}$ with normalizing/weighted prefactors (w_1 and w_2); $\epsilon_m = w_1\epsilon_{EtOH} + w_2\epsilon_{C_6H_{12}}$ (see Figure 6.7a). Although the ordering of the dielectric functions can be seen to switch at around 18 eV, all solvents for which the interaction was calculated can be seen to possess an equilibrium separation. Figure 6.7b shows that by varying the dielectric function of the medium between those described by ϵ_{EtOH} and $\epsilon_{C_6H_{12}}$, one can gain a soft control of the equilibrium separation with 11 possible equilibrium separations predicted between gold and a PTFE - gold interface. Given the various binary mixture models [176, 177] and the vastly different dielectric nature of the considered solvents, it is reasonable to assume that quantum entrapment can occur in a wide range of solvents.

Whilst the PTFE - gold interaction is largely effected by the change of the medium, attraction between gold terminated interfaces remains almost the same in cycloxehane as in ethanol. This can be attributed to a much greater value of the dielectric function of gold compared to PTFE and the solvents, which makes the gold - gold interaction dominant in any medium.

6.4 Conclusions

In conclusion, this is a comprehensive quantitative analysis of the experimental AFM and SFA measurements of the Casimir force between layered materials in solvents. The complexity of the problem has been extended here to include triple layer interfaces, whilst the effect of the compositional changes on the Casimir effect have also been investigated.

In the context of the quantum entrapment experiments [165], it has been shown that a delicate control of the position of the Casimir equilibrium can be achieved between the gold nanoplate and a PTFE - gold double layer interface through a variation of the thickness of the PTFE overlayer. This has been further extended here, such that if the gold layer is on top, only attractive Casimir interactions can be established, regardless of the chosen solvent, number of layers in the interface, and the thickness of the top gold layer. The equilibrium separation and the strength of the Casimir

interaction also depend critically on the the dielectric function of the medium.

All these findings might have significant implications in self-assembly of layered materials and design of future quantum entrapment experiments, given various experimentally viable layered interfaces. [178]

Chapter 7

Conclusion

In conclusion, theoretical descriptions of charged induced polarisation and dispersion forces between materials have been extended and applied to study a range of natural and novel environments. A mathematical framework previously established to describe many-body interactions between charged dielectric particles[48] was extended to include the effects of inhomogeneous surface charge distributions and externally applied electric fields.[17] This extension was rigorously tested against both classical results and physical justifications, all of which it found excellent agreement with. It was then further justified via providing a platform for the investigation of large, novel, and experimentally realised many-body systems of colloidal particles. In such systems, we found excellent agreement with the experimental observations of colloidal crystal breakdown above certain electric field strengths, which were previously unconsidered, hence proving evidence that the breakdown of such materials in external electric fields is due to the charged induced interactions between the particles.

The framework was then applied to study the effect of surface charge density and polarisation on the interactions between like-charged particles in noctilucent clouds via statistical methods. Previously, like-charge attraction between particles was shown to promote nucleation of particles via thermal fluctuations in the atmosphere of Titan.[25] Such aggregation was hypothesized and investigated in chapter 3, in the context of ice particles and meteoric dust nucleating; this could possibly contribute to noctilucent cloud formation.[129].

Volcanic ash was then initially investigated in a similar context at the various temperatures it would experience throughout an eruption. However, all aggregation states were shown to be inaccessible via thermal motion given the size of the Coulomb barrier between the particles. However, these results did show that like-charge induced aggregation of volcanic ash particles could still be possible due to non-thermal perturbations. This was investigated by considering the collisional cross sections of the clouds constituents via a particle dynamics adaptation of the framework described in chapter 2; such investigations found that like-charge attraction can increase the collisional cross section by up to 19%.

Particle dynamics was then further utilised to study the aggregation driven inefficiencies of dry powder inhalers; although it was shown that no like charge attraction occurs within the stream expelled from an inhaler, the many-body interactions between oppositely charged particles were found to enable uncontrolled cluster growth. This uncontrolled nucleation was further investigated, and it was found that the product of such growth mechanisms are ineffective as pharmaceuticals due to biological size restrictions imposed throughout the bronchial tract. A method to limit such particle growth was proposed in the form of a filtered dual stream device, which given the results of this work would alleviate the growth of such particulates.

Finally, the electronic interaction between neutral materials at close separation was investigated in the context of the Casimir force. Initial bench-marking of a suitable mathematical formalism to describe layered interfaces[166] found unprecedented accuracy with experimental literature at low computational cost when utilising newly optimised oscillator models to describe the materials. As such, new systems in which quantum levitation/entrapment can occur were then proposed via consideration of the relative size of the dielectric function describing each material; this was possible given the low cost of the evaluation of the implemented formalism. Such systems included triply layered substrates and potential new mediums of interaction. Given the (newly found) mediums of interaction able to cause such levitation, the possibility of equilibrium control via the mixing of dielectrics was also realised as a way to fine-tune the equilibrium separation between the two bodies, unlike the drastic changes that were found to occur upon variation of the interface.

7.1   Future Work

Given the many-body formalism presented in this work, many other physically relevant particles/environments can be described; these include but are not limited to the inclusion of a dielectric plane interacting with N spheres, the effect of magnetic perturbations on such system, and the effects of electrolytes on the system. The formalism presented in chapter 2, although able to describe the interaction of particles in volcanic ash clouds and dry powder inhalers, was only able to undergo limited analysis given the lack of temperature dependence on the systems studied. As such, if further external perturbations in such systems were better described mathematically, one could calculate the nucleation within them. Finally, if a suitable dielectric mixing model is utilised, it could be possible to fine tune the equilibrium separation in systems which undergo quantum levitation, hence enabling one to choose the height of their desired levitation - this could also be possible for various solvents not considered in this work, all of which would enable a wider range of possible interactions and, therefore, applications.

Bibliography

[1] J. C. Maxwell, "On physical lines of force. part 1. the theory of molecular vortices applied to magnetic phenomena," *Philosophical Magazine.*, no. XXI, pp. 161–175, 1861.

[2] ——, "On physical lines of force. part 2. the theory of electrical vortices applied to electric currents," *Philosophical Magazine.*, no. XXI, pp. 281–291, 1861.

[3] ——, "On physical lines of force. part 3. the theory of electrical vortices applied to statical electricity," *Philosophical Magazine.*, no. XXIII, pp. 12—-24, 1862.

[4] ——, "On physical lines of force. part 4. the theory of electrical vortices applied to the action of magnetism on polarized light," *Philosophical Magazine.*, no. XXIII, p. 12–24, 1862.

[5] Coulomb, "Premier memoire sur l'electricit'e et le magnetisme." *l'Academie Royale des Sciences*, pp. 569–577, 1785.

[6] R. P. Feynman, *The Feynman Lectures on Physics ii - Electromagnatism*, 2013, vol. 53, no. 9.

[7] R. D. Knight, *Physics for scientists and engineers : a strategic approach : with modern physics / Randall d. Knight.*, 3rd ed.   Boston, Mass. ; London: Pearson, 2013.

[8] J.-L. Lagrange, "Essai sur le problème des trois corps," *Miscellanea Taurinensia*, vol. 5, 1773.

[9] C. F. Gauss, *Carl Friedrich Gauss Werke*, ser. Carl Friedrich Gauss Werke. Königlichen Gesellschaft der wissenschaften, 1877, no. v. 5.

[10] R. Feynman, *The Feynman lectures on physics. Volume 2, Mainly electromagnetism and matter / Richard p. Feynman, Robert b. Leighton and Matthew Sands.*   Reading, Mass.: Addison-Wesley, 1964.

[11] H. A. Lorentz, "La théorie électromagnétique de maxwell et son application aux corps mouvants," *Archives Néerlandaises des Sciences Exactes et Naturelles*, vol. 25, 1895.

[12] J. C. Maxwell, "a dynamical theory of the electromagnetic field," *Philosophical Transactions of the Royal Society of London*, vol. 155, pp. 459–512, 1865.

[13] W. Thomson, *determination of the distribution of electricity on a circular segment of plane or spherical conducting surface, under any given influence*, ser. Cambridge Library Collection - Physical Sciences.   Cambridge University Press, 2011, p. 178–191.

[14] L. D. Landau, E. M. Lifshitz, and L. P. Pitaevskii, *Electrodynamics of Continuous Media*, 2nd ed. London: Elsevier, 1960.

[15] R. Messina, "Image charges in spherical geometry: Application to colloidal systems," *The Journal of Chemical Physics*, vol. 117, no. 24, pp. 11 062–11 074, 2002.

[16] I. V. Lindell, "Electrostatic image theory for the dielectric sphere," *Radio Science*, vol. 27, no. 1, pp. 1–8, 1992.

[17] M. Hassan, C. Williamson, J. Baptiste, S. Braun, A. J. Stace, E. Besley, and B. Stamm, "Manipulating interactions between dielectric particles with electric fields: a general electrostatic many-body framework," *Journal of Chemical Theory and Computation*, vol. 18, pp. 6281–6296, 2022.

[18] E. Bichoutskaia, A. Boatwright, A. Khachatourian, and A. Stace, "Electrostatic analysis of the interactions between charged particles of dielectric materials," *Journal of Chemical Physics*, vol. 133, p. 024105, 2010.

[19] A.-M. Legendre, "Recherches sur l'attraction des sphéroïdes homogènes," *Mémoires de Mathématiques et de Physique*, pp. 178–191, 1782.

[20] E. B. Lindgren, "Theoretical analysis of the electrostatic interactions between charged polarisable particles," Ph.D. dissertation, University of Nottingham, 2017.

[21] A. J. Stace, A. L. Boatwright, A. Khachatourian, and E. Bichoutskaia, "Why like-charged particles of dielectric materials can be attracted to one another," *Journal of Colloid and Interface Science*, vol. 354, no. 1, pp. 417–420, 2011.

[22] A. J. Stace and E. Bichoutskaia, "Absolute electrostatic force between two charged particles in a low dielectric solvent," *Soft Matter*, vol. 8, no. 23, pp. 6210–6213, 2012.

[23] I. N. Derbenev, A. V. Filippov, A. J. Stace, and E. Besley, "Electrostatic interactions between spheroidal dielectric particles," *The Journal of Chemical Physics*, vol. 152, no. 2, p. 024121, 2020.

[24] A. Khachatourian, H.-K. Chan, A. J. Stace, and E. Bichoutskaia, "Electrostatic force between a charged sphere and a planar surface: a general solution for dielectric materials," *The Journal of Chemical Physics*, vol. 140, no. 7, p. 74107, 2014.

[25] E. B. Lindgren, B. Stamm, H.-K. Chan, Y. Maday, A. J. Stace, and E. Besley, "The effect of like-charge attraction on aerosol growth in the atmosphere of Titan," *Icarus*, vol. 291, pp. 245–253, 2017.

[26] J. Baptiste, C. Williamson, J. Fox, A. J. Stace, M. Hassan, S. Braun, B. Stamm, I. Mann, and E. Besley, "The influence of surface charge on the coalescence of ice and dust particles in the mesosphere and lower thermosphere," *Atmospheric Chemistry and Physics*, vol. 21, no. 11, pp. 8735–8745, 2021.

[27] N. Mehr, D. Grigoriev, R. Heaton, J. Baptiste, A. Stace, N. Puretskiy, E. Besley, and A. Böker, "Self-assembly behavior of oppositely charged inverse bipatchy microcolloids," *Small*, vol. 16, p. 2000442, 2020.

[28] A. Miller, M. Halstead, E. Besley, and A. J. Stace, "Designing stable binary endohedral fullerene lattices," *Phys. Chem. Chem. Phys.*, vol. 24, pp. 10 044–10 052, 2022.

[29] E. M. Lifshitz, "Theory of molecular attractive forces between condensed bodies," *Soviet Physics JETP*, vol. 2, p. 73, 1956.

[30] E. M. Lifshitz, I. E. Dzyaloshinskii, and L. P. Pitaevskii, "General theory of van der waals forces," *Soviet Physics Uspekhi*, vol. 4, p. 165, 1961.

[31] H. Casimir, "On the attraction between two perfectly conducting plates," *Proceedings of the Koninklijke Nederlandse Akademie van Wetenschappen*, pp. 793–795, 1948.

[32] P. D. Casimir, H.B.G, "The influence of retardation on the london-van der waals forces," *Physical Review*, pp. 360–372, 1948.

[33] T. Matsubara, "a New approach to quantum statistical mechanics," *Prog. Theor. Phys.*, vol. 14, pp. 351–378, 1955.

[34] V. A. V. A. Parsegian, *Van der Waals forces : a handbook for biologists, chemists, engineers, and physicists.* New York: Cambridge University Press, 2006.

[35] H. A. Kramers, "Dispersion relations for the refractive index of a transparent substance," *Atti Accademia Nazionale Lincei*, vol. 6, pp. 714–720, 1927.

[36] M. Moazzami Gudarzi and S. H. Aboutalebi, "Self-consistent dielectric functions of materials: Toward accurate computation of Casimir–van der Waals forces," *Science Advances*, vol. 7, no. 22, p. eabg2272, 2024.

[37] J. N. Munday, F. Capasso, and V. A. Parsegian, "Measured long-range repulsive Casimir–Lifshitz forces," *Nature*, vol. 457, no. 7226, pp. 170–173, 2009.

[38] G. Palasantzas, M. Sedighi, and V. B. Svetovoy, "Applications of casimir forces: Nanoscale actuation and adhesion," *Applied Physics Letters*, vol. 117, p. 120501, 2020.

[39] S. K. Lamoreaux, "Casimir forces: Still surprising after 60 years," *Physics Today*, vol. 60, p. 40, 2007.

[40] V. B. Svetovoy, P. J. van Zwol, G. Palasantzas, and J. T. M. De Hosson, "Optical properties of gold films and the casimir force," *Physical Review B*, vol. 77, p. 35439, 2008.

[41] D. A. T. Somers and J. N. Munday, "Conditions for repulsive casimir forces between identical birefringent materials," *Physical Review A*, vol. 95, p. 022509, 2017.

[42] N. Inui, "Levitation of a metallic sphere near gas-liquid and liquid-liquid interfaces by the repulsive casimir force," *Physical Review A - Atomic, Molecular, and Optical Physics*, vol. 89, p. 062506, 2014.

[43] Q. Hu, J. Sun, Q. Zhao, and Y. Meng, "Experimentally demonstration of the repulsive casimir force in the gold - cyclohexane - ptfe system," *preprint*, 2019, arXiv:1911.09938.

[44] V. K. Pappakrishnan, P. C. Mundru, and D. A. Genov, "Repulsive casimir force in magnetodielectric plate configurations," *Physical Review B*, vol. 89, p. 045430, 2014.

[45] M. Levin, A. P. McCauley, A. W. Rodriguez, M. T. H. Reid, and S. G. Johnson, "Casimir repulsion between metallic objects in vacuum," *Physical Review Letters*, vol. 105, p. 090403, 2010.

[46] P. J. V. Zwol and G. Palasantzas, "Repulsive casimir forces between solid materials with high-refractive-index intervening liquids," *Physical Review A*, vol. 81, p. 062502, 2010.

[47] M. Leunissen, C. Christova, A.-P. Hynninen, C. P. Royall, A. Campbell, A. Imhof, M. Dijkstra, R. van Roij, and A. Van Blaaderen, "Ionic colloidal crystals of oppositely charged particles," *Nature*, vol. 437, no. 7056, pp. 235–240, 2005.

[48] E. Lindgren, B. Stamm, H.-K. Chan, Y. Maday, A. Stace, and E. Besley, "The effect of like-charge attraction on aerosol growth in the atmosphere of titan," *Icarus*, vol. 291, pp. 245–253, 2017.

[49] E. Lindgren, A. Stace, E. Polack, Y. Maday, B. Stamm, and E. Besley, "An integral equation approach to calculate electrostatic interactions in many-body dielectric systems," *J. Comp. Phys.*, vol. 371, pp. 712–731, 2018.

[50] A. V. Filippov, X. Chen, C. Harris, A. J. Stace, and E. Besley, "Interaction between particles with inhomogeneous surface charge distributions: Revisiting the coulomb fission of dication molecular clusters," *Journal of Chemical Physics*, vol. 151, no. 15, p. 154113, 2019.

[51] M. W. McKittrick and C. W. Jones, "Toward single-site functional materialspreparation of amine-functionalized surfaces exhibiting site-isolated behavior," *Chemistry of Materials*, vol. 15, pp. 1132–1139, 3 2003.

[52] A. J. Stone, *The theory of intermolecular forces*, 2nd ed. Oxford: Oxford University Press, 2013.

[53] J. Bentor, H. Dort, R. A. Chitrao, Y. Zhang, and X. Xuan, "Nonlinear electrophoresis of dielectric particles in newtonian fluids," *Electrophoresis*, vol. 44, no. 11-12, pp. 938–946, 2023.

[54] B. Techaumnat and T. Takuma, "Calculation of the electric field for lined-up spherical dielectric particles," *IEEE transactions on dielectrics and electrical insulation*, vol. 10, no. 4, pp. 623–633, 2003.

[55] M. Hassan and B. Stamm, "An integral equation formulation of the n-body dielectric spheres problem. Part I: Numerical Analysis," *ESAIM: Math. Model. Numer. Anal.*, vol. 55, pp. S65 – S102, 2020.

[56] B. Bramas, M. Hassan, and B. Stamm, "An integral equation formulation of the n-body dielectric spheres problem. Part II: Complexity Analysis," *preprint*, 2020, arXiv:1911.07258.

[57] M. Hassan and B. Stamm, "a linear scaling in accuracy numerical method for computing the electrostatic forces in the n-body dielectric spheres problem," *Commun. Comput. Phys.*, vol. 29, no. 2, pp. 319–356, 2021.

[58] E. B. Lindgren, A. J. Stace, E. Polack, Y. Maday, B. Stamm, and E. Besley, "An integral equation approach to calculate electrostatic interactions in many-body dielectric systems," *Journal of Computational Physics*, vol. 371, pp. 712–731, 2018.

[59] E. Vermolen, A. Kuijk, L. Filion, M. Hermes, J. Thijssen, M. Dijkstra, and A. Van Blaaderen, "Fabrication of large binary colloidal crystals with a NaCl structure," *Proceedings of the National Academy of Sciences*, vol. 106, no. 38, pp. 16 063–16 067, 2009.

[60] L. Megner, M. Rapp, and J. Gumbel, "Distribution of meteoric smoke - Sensitivity to microphysical properties and atmospheric conditions," *Atmospheric Chemistry and Physics*, vol. 6, no. 12, pp. 4415–4426, 2006.

[61] M. Rapp, J. M. C. Plane, B. Strelnikov, G. Stober, S. Ernst, J. Hedin, M. Friedrich, and U.-P. Hoppe, "In situ observations of meteor smoke particles (msp) during the Geminids 2010: constraints on msp size, work function and composition," *Ann. Geophys.*, vol. 30, no. 12, pp. 1661–1673, 2012.

[62] I. Mann, A. Pellinen-Wannberg, E. Murad, O. Popova, N. Meyer-Vernet, M. Rosenberg, T. Mukai, A. Czechowski, S. Mukai, J. Safrankova, and Z. Nemecek, "Dusty plasma effects in near earth space and interplanetary medium," *Space Science Reviews*, vol. 161, no. 1, pp. 1–47, 2011.

[63] J. Brooke, W. Feng, J. Carrillo-Sánchez, G. Mann, A. James, C. Bardeen, L. Marshall, S. Dhomse, and J. Plane, "Meteoric smoke deposition in the polar regions: a comparison of measurements with global atmospheric models," *Journal of Geophysical Research: Atmospheres*, vol. 122, no. 20, pp. 11 112–11 130, 2017.

[64] F.-J. Lübken, "Thermal structure of the Arctic summer mesosphere," *Journal of Geophysical Research: Atmospheres*, vol. 104, no. D8, pp. 9135–9149, 1999.

[65] M. Hervig, R. E. Thompson, M. McHugh, L. L. Gordley, J. M. Russell III, and M. E. Summers, "First confirmation that water ice is the primary component of polar mesospheric clouds," *Geophysical Research Letters*, vol. 28, no. 6, pp. 971–974, 2001.

[66] F.-J. Lübken, U. Berger, and G. Baumgarten, "On the Anthropogenic Impact on Long-Term Evolution of Noctilucent Clouds," *Geophysical Research Letters*, vol. 45, no. 13, pp. 6681–6689, 2018.

[67] C. G. Bardeen, O. B. Toon, E. J. Jensen, D. R. Marsh, and V. L. Harvey, "Numerical simulations of the three-dimensional distribution of meteoric dust in the mesosphere and upper stratosphere," *Journal of Geophysical Research: Atmospheres*, vol. 113, no. D17, 2008.

[68] L. Zhang, B. Tinsley, and L. Zhou, "Parameterization of in-cloud aerosol scavenging due to atmospheric ionization: part 4. effects of varying altitude," *Journal of Geophysical Research: Atmospheres*, vol. 124, pp. 13 105–13 126, 2019.

[69] E. Bichoutskaia, A. L. Boatwright, A. Khachatourian, and A. J. Stace, "Electrostatic analysis of the interactions between charged particles of dielectric materials," *Journal of Chemical Physics*, vol. 133, no. 2, pp. 1–10, 2010.

[70] E. B. Lindgren, I. N. Derbenev, A. Khachatourian, H. K. Chan, A. J. Stace, and E. Besley, "Electrostatic Self-Assembly: Understanding the Significance of the Solvent," *Journal of Chemical Theory and Computation*, vol. 14, no. 2, pp. 905–915, 2018.

[71] E. B. Lindgren, "Theoretical analysis of the electrostatic interactions between charged polarisable particles," *Icarus*, vol. 291, pp. 245–253, 2017.

[72] F. Naderi Mehr, D. Grigoriev, R. Heaton, J. Baptiste, A. J. Stace, N. Puretskiy, E. Besley, and A. Böker, "Self-Assembly Behavior of Oppositely Charged Inverse Bipatchy Microcolloids," *Small*, vol. 16, no. 14, pp. 1–9, 2020.

[73] J. D. Jackson, *Classical Electrodynamics (3rd Edition)*. John Wiley Sons, 1999.

[74] B. Journaux, J. M. Brown, A. Pakhomova, I. E. Collings, S. Petitgirard, P. Espinoza, T. Boffa Ballaran, S. D. Vance, J. Ott, F. Cova, G. Garbarino, and M. Hanfland, "Holistic approach for studying planetary hydrospheres: Gibbs representation of ices thermodynamics, elasticity, and the water phase diagram to 2,300 mpa," *Journal of Geophysical Research: Planets*, vol. 125, no. 1, p. e2019JE006176, 2020.

[75] A. Hudait and V. Molinero, "What Determines the Ice Polymorph in Clouds?" *Journal of the American Chemical Society*, vol. 138, no. 28, pp. 8958–8967, 2016.

[76] H. J. W. Müller-Kirsten, *Basics of Statistical Physics (2nd Edition)*. World Scientific Publishing Company, 2013.

[77] M. E. Hervig, L. E. Deaver, C. G. Bardeen, J. M. Russell, S. M. Bailey, and L. L. Gordley, "The content and composition of meteoric smoke in mesospheric ice particles from sofie observations," *Journal of Atmospheric and Solar-Terrestrial Physics*, vol. 84-85, pp. 1–6, 2012.

[78] J. M. C. Plane, W. Feng, and E. C. M. Dawkins, "The Mesosphere and Metals: Chemistry and Changes," *Chemical Reviews*, vol. 115, no. 10, pp. 4497–4541, 2015.

[79] J. Guiver and J. Jain, "Grounded: Impacts of and Insights from the Volcanic Ash Cloud Disruption," *Mobilities*, vol. 6, no. 1, pp. 41–55, 2011.

[80] T. M. Wilson, S. Jenkins, and C. Stewart, "Chapter 3 - Impacts from Volcanic Ash Fall," in *Hazards and Disasters Series*, J. F. Shroder and P. B. T. V. H. Papale Risks and Disasters, Eds. Boston: Elsevier, 2015, pp. 47–86.

[81] G. T. Swindles, I. T. Lawson, I. P. Savov, C. B. Connor, and G. Plunkett, "a 7000 yr perspective on volcanic ash clouds affecting northern Europe," *Geology*, vol. 39, no. 9, pp. 887–890, 2011.

[82] T. M. Wilson, C. Stewart, V. Sword-Daniels, G. S. Leonard, D. M. Johnston, J. W. Cole, J. Wardman, G. Wilson, and S. T. Barnard, "Volcanic ash impacts on critical infrastructure," *Physics and Chemistry of the Earth, Parts a/b/c*, vol. 45, pp. 5–23, 2012.

[83] S. S. Crowley, D. A. Dufek, R. W. Stanton, and T. A. Ryer, "The effects of volcanic ash disturbances on a peat: Forming environment: Environmental disruption and taphonomic consequences," *Palaios*, pp. 158–174, 1994.

[84] J. Dufek, M. Manga, and A. Patel, "Granular disruption during explosive volcanic eruptions," *Nature Geoscience*, vol. 5, no. 8, pp. 561–564, 2012.

[85] C. J. Horwell and P. J. Baxter, "The respiratory health hazards of volcanic ash: a review for volcanic risk mitigation," *Bulletin of Volcanology*, vol. 69, no. 1, pp. 1–24, 2006.

[86] B. Langmann, "On the Role of Climate Forcing by Volcanic Sulphate and Volcanic Ash," *Advances in Meteorology*, vol. 2014, no. 1, p. 340123, 2014.

[87] A. J. PRATA, "Observations of volcanic ash clouds in the 10-12 μm window using avhrr/2 data," *International Journal of Remote Sensing*, vol. 10, no. 4-5, pp. 751–761, 1989.

[88] R. J. Brown, C. Bonadonna, and A. J. Durant, "a review of volcanic ash aggregation," *Physics and Chemistry of the Earth, Parts A/B/C*, vol. 45-46, pp. 65–78, 2012.

[89] S. B. Mueller, U. Kueppers, M. S. Huber, K.-U. Hess, G. Poesges, B. Ruthensteiner, and D. B. Dingwell, "Aggregation in particle rich environments: a textural study of examples from volcanic eruptions, meteorite impacts, and fluidized bed processing," *Bulletin of Volcanology*, vol. 80, no. 4, p. 32, 2018.

[90] J. M. Harper and J. Dufek, "Journal of geophysical research," *Nature*, vol. 175, no. 4449, p. 238, 1955.

[91] A. Vogel, S. Diplas, A. J. Durant, A. S. Azar, M. F. Sunding, W. I. Rose, A. Sytchkova, C. Bonadonna, K. Krüger, and A. Stohl, "Reference data set of volcanic ash physicochemical and optical properties," *Journal of Geophysical Research: Atmospheres*, vol. 122, no. 17, pp. 9485–9514, 2017.

[92] R. S. J. Sparks, "Gas release rates from pyroclastic flows: a assessment of the role of fluidisation in their emplacement," *Bulletin Volcanologique*, vol. 41, no. 1, pp. 1–9, 1978.

[93] K. H. Wohletz, M. F. Sheridan, and W. K. Brown, "Particle size distributions and the sequential fragmentation/transport theory applied to volcanic ash," *Journal of Geophysical Research: Solid Earth*, vol. 94, no. B11, pp. 15 703–15 721, 1989.

[94] J. Baptiste, "Electrostatic theory of charged particle polarisation: applications in self-assembly, pharmaceutical and atmospheric processes," Ph.D. dissertation, University of Nottingham, 2021.

[95] T. Peng, S. Lin, B. Niu, X. Wang, Y. Huang, X. Zhang, G. Li, X. Pan, and C. Wu, "Influence of physical properties of carrier on the performance of dry powder inhalers." *Acta pharmaceutica Sinica. B*, vol. 6, pp. 308–318, 2016.

[96] I. Starke, S. Fürstenberg, and S. Thomas, "Utilizing esi-ms/ms and ion mobility spectrometry for structural characterization and isomer differentiation of 1, 2-unsaturated (1-4) linked disaccharide derivatives and their 2-c-functionalized analogues," *Rapid Communications in Mass Spectrometry*, vol. 38, no. 23, p. e9899, 2024.

[97] S. Naskar, A. Minoia, Q. Duez, A. Izuagbe, J. De Winter, S. J. Blanksby, C. Barner-Kowollik, J. Cornil, and P. Gerbaux, "Polystyrene chain geometry probed by ion mobility mass spectrometry and molecular dynamics simulations," *Journal of the American Society for Mass Spectrometry*, vol. 35, no. 10, pp. 2408–2419, 2024.

[98] P. Patra, D. L. Koch, and A. Roy, "Collision efficiency of like-charged spheres settling in a quiescent environment," *Journal of Fluid Mechanics*, vol. 968, pp. 1–25, 2023.

[99] K. Giri, L. González-Sánchez, F. Gianturco, U. Lourderaj, A. M. S. María, S. Rana, N. Sathyamurthy, E. Yurtsever, and R. Wester, "Rotationally inelastic rate coefficients for c7n- and c10h- anions in collision with h2 at interstellar conditions," *Monthly Notices of the Royal Astronomical Society*, vol. 534, p. 2187, 2024.

[100] Y. Simón-Manso, "Ion-Neutral Collision Cross Section as a Function of the Static Dipole Polarizability and the Ionization Energy of the Ion," *Journal of Physical Chemistry A*, vol. 127, no. 15, pp. 3274–3280, 2023.

[101] J. Saxby, F. Beckett, K. Cashman, A. Rust, and E. Tennant, "The impact of particle shape on fall velocity: Implications for volcanic ash dispersion modelling," *Journal of Volcanology and Geothermal Research*, vol. 362, pp. 32–48, 2018.

[102] Y. Feng, K. Han, and D. Owen, "Coupled lattice boltzmann method and discrete element modelling of particle transport in turbulent fluid flows: Computational issues," *International Journal for Numerical Methods in Engineering*, vol. 72, no. 9, pp. 1111–1134, 2007.

[103] K. D. Kafui, C. Thornton, and M. J. Adams, "Discrete particle-continuum fluid modelling of gas–solid fluidised beds," *Chemical Engineering Science*, vol. 57, no. 13, pp. 2395–2410, 2002.

[104] N. Numanami, T. Ohba, and M. Yaguchi, "Principal component analysis for the elemental composition of sedimentary sands in the hayakawa river of hakone caldera, japan," *Geochemical Journal*, vol. 58, no. 4, pp. 155–168, 2024.

[105] C. Li, H.-H. Chen, X.-H. Lang, Y.-L. Deng, and Y.-T. Wang, "Volcanic activity during the early–middle triassic transition in the sichuan basin, south china: Duration, evolution and implications," *Geological Journal*, vol. 59, no. 7, pp. 2118–2135, 2024.

[106] P. Delmelle, M. Lambert, Y. Dufrêne, P. Gerin, and N. Óskarsson, "Gas/aerosol–ash interaction in volcanic plumes: New insights from surface analyses of fine ash particles," *Earth Planet. Sci. Lett.*, vol. 259, no. 1-2, pp. 159–170, Jul. 2007.

[107] R. D. Shannon, "Dielectric polarizabilities of ions in oxides and fluorides," *J. Appl. Phys.*, vol. 73, no. 1, pp. 348–366, Jan. 1993.

[108] S. R. Waitukaitis, V. Lee, J. M. Pierson, S. L. Forman, and H. M. Jaeger, "Size-dependent same-material tribocharging in insulating grains," *Phys. Rev. Lett.*, vol. 112, p. 218001, 2014.

[109] X. Liu, J. Kolehmainen, I. Nwogbaga, A. Ozel, and S. Sundaresan, "Effect of particle size on tribocharging," *Powder Technology*, vol. 375, pp. 199–209, 2020.

[110] P. W. Cleary, G. Metcalfe, and K. Liffman, "How well do discrete element granular flow models capture the essentials of mixing processes?" *Applied Mathematical Modelling*, vol. 22, no. 12, pp. 995–1008, 1998.

[111] M. Bursik, A. Patra, E. Pitman, C. Nichita, J. Macias, R. Saucedo, and O. Girina, "Advances in studies of dense volcanic granular flows," *Reports on Progress in Physics*, vol. 68, no. 2, p. 271, 2005.

[112] T. Chan and C. Yu, "Charge effects on particle deposition in the human tracheobronchial tree," *Ann. Occup. Hyg.*, vol. 26, pp. 65–75, 1982.

[113] C. Melandri, G. Tarroni, V. Prodi, T. De Zaiacomo, M. Formignani, and C. Lombardi, "Deposition of charged particles in the human airways," *Journal of Aerosol Science*, vol. 14, pp. 657–669, 1983.

[114] B. Liu, D. Pui, K. Rubow, and W. Szymanski, "Electrostatic effects in aerosol sampling and filtration," *Ann. Occup. Hyg.*, vol. 29, pp. 251–269, 1985.

[115] A. Bailey, "The inhalation and deposition of charged particles within the human lung," *Journal of Electrostatics*, vol. 42, pp. 25–32, 1997.

[116] A.-M. Ciciliani, P. Langguth, and H. Wachtel, "In vitro dose comparison of respimat® inhaler with dry powder inhalers for copd maintenance therapy," *International journal of chronic obstructive pulmonary disease*, vol. 12, pp. 1565–1577, 2017.

[117] J. Wong, H.-K. Chan, and P. C. L. Kwok, "Electrostatics in pharmaceutical aerosols for inhalation," *Therapeutic Delivery*, vol. 4, pp. 981–1002, 2013.

[118] W. Balachandran, W. Machowski, E. Gaura, and C. Hudson, "Control of drug aerosol in human airways using electrostatic forces," *Journal of Electrostatics*, vol. 40, pp. 579–584, 1997.

[119] J. Wong, P. C. L. Kwok, V. Niemelä, D. Heng, J. Crapper, and H.-K. Chan, "Bipolar electrostatic charge and mass distributions of powder aerosols – Effects of inhaler design and inhaler material," *Journal of Aerosol Science*, vol. 95, pp. 104–117, 2016.

[120] W. Balachandran, J. Kulon, D. Koolpiruck, M. Dawson, and P. Burnel, "Bipolar charge measurement of pharmaceutical powders," *Powder Technology*, vol. 135-136, pp. 156–163, 2003.

[121] P. A. Carter, G. Rowley, E. J. Fletcher, and V. Stylianopoulos, "Measurement of electrostatic charge decay in pharmaceutical powders and polymer materials used in dry powder inhaler devices," *Drug Development and Industrial Pharmacy*, vol. 24, pp. 1083–1088, 1998.

[122] J. N. Staniforth and J. E. Rees, "Electrostatic charge interactions in ordered powder mixes," *Journal of Pharmacy and Pharmacology*, vol. 34, p. 69–76, 1982.

[123] P. A. Carter, G. Rowley, E. J. Fletcher, and E. A. Hill, "An experimental investigation of triboelectrification in cohesive and non-cohesive pharmaceutical powders," *Drug Development and Industrial Pharmacy*, vol. 18, pp. 1505–1526, 2008.

[124] P. R. Byron, J. Peart, and J. N. Staniforth, "Aerosol electrostatics. i: Properties of fine powders before and after aerosolization by dry powder inhalers," *Pharmaceutical Research*, vol. 14, p. 698–705, 1997.

[125] F. S. Bennett, P. A. Carter, G. Rowley, and Y. Dandiker, "Modification of electrostatic charge on inhaled carrier lactose particles by addition of fine particles," *Drug Development and Industrial Pharmacy*, vol. 25, pp. 99–103, 1999.

[126] J. C. Sung, B. L. Pulliam, and D. A. Edwards, "Nanoparticles for drug delivery to the lungs," *Trends in Biotechnology*, vol. 25, pp. 563–570, 2007.

[127] M. Taira, M. Sasaki, S. Kimura, and Y. Araki, "Characterization of aerosols and fine particles produced in dentistry and their health risk assessments," *Nano Biomedicine*, vol. 1, no. 1, pp. 9–15, 2009.

[128] J. S. Brown, T. Gordon, O. Price, and B. Asgharian, "Thoracic and respirable particle definitions for human health risk assessment," *Particle and Fibre Toxicology*, vol. 10, p. 12, 2013.

[129] J. Baptiste, C. Williamson, J. Fox, A. J. Stace, M. Hassan, S. Braun, B. Stamm, I. Mann, and E. Besley, "The influence of surface charge on the coalescence of ice and dust particles in the mesosphere," *Atmospheric Chemistry and Physics Discussions*, vol. 21, p. 8735–8745, 2021.

[130] J. Yli-Ojanperä, A. Ukkonen, A. Järvinen, S. Layzell, V. Niemelä, and J. Keskinen, "Bipolar charge analyzer (bolar): a new aerosol instrument for bipolar charge measurements," *Journal of Aerosol Science*, vol. 77, pp. 16–30, 2014.

[131] S. Hoe, P. Young, and D. Traini, "a review of electrostatic measurement techniques for aerosol drug delivery to the lung: Implications in aerosol particle deposition," *Journal of Adhesion Science and Technology*, vol. 25, pp. 385–405, 2012.

[132] Z. Zheng, S. S. Y. Leung, and R. Gupta, "Flow and Particle Modelling of Dry Powder Inhalers: Methodologies, Recent Development and Emerging Applications," *Pharmaceutics*, vol. 13, p. 189, 2021.

[133] B. Chaurasiya and Y.-Y. Zhao, "Dry Powder for Pulmonary Delivery: a Comprehensive Review," *Pharmaceutics*, vol. 13, p. 31, 2021.

[134] J. Wong, Y.-W. Lin, P. C. L. Kwok, V. Niemelä, J. Crapper, and H.-K. Chan, "Measuring bipolar charge and mass distributions of powder aerosols by a novel tool (bolar)," *Molecular Pharmaceutics*, vol. 12, pp. 3433–3440, 2015.

[135] R. Bharadwaj, C. Smith, and B. C. Hancock, "The coefficient of restitution of some pharmaceutical tablets/compacts," *International Journal of Pharmaceutics*, vol. 402, pp. 50–56, 2010.

[136] E. Bichoutskaia, A. L. Boatwright, A. Khachatourian, and A. J. Stace, "Electrostatic analysis of the interactions between charged particles of dielectric materials," *Journal of Chemical Physics*, vol. 133, p. 24105, 2010.

[137] O. Kenneth and I. Klich, "Opposites attract: a theorem about the casimir force," *Phys. Rev. Lett.*, vol. 97, p. 160401, 2006.

[138] S. K. Lamoreaux, "Demonstration of the casimir force in the 0.6 to 6 μm range," *Phys. Rev. Lett.*, vol. 78, pp. 5–8, 1997.

[139] G. L. Klimchitskaya, U. Mohideen, and V. M. Mostepanenko, "The casimir force between real materials: Experiment and theory," *Reviews of Modern Physics*, vol. 81, pp. 1827–1885, 12 2009.

[140] M. Wang, L. Tang, C. Y. Ng, R. Messina, B. Guizal, J. A. Crosse, M. Antezza, C. T. Chan, and H. B. Chan, "Strong geometry dependence of the casimir force between interpenetrated rectangular gratings," *Nature Communications*, vol. 12, pp. 600–609, 2021.

[141] P. Antonini, G. Bimonte, G. Bressi, G. Carugno, G. Galeazzi, G. Messineo, and G. Ruoso, "An experimental apparatus for measuring the casimir effect at large distances," *Journal of Physics: Conference Series*, vol. 161, p. 012006, 2009.

[142] I. E. Dzyaloshinskii, E. M. Lifshitz, and L. P. Pitaevskii, "The general theory of van der waals forces," *Adv. Phys.*, vol. 10, pp. 165–209, 1961.

[143] P. J. V. Zwol and G. Palasantzas, "Repulsive casimir forces between solid materials with high-refractive-index intervening liquids," *Physical Review A*, vol. 81, p. 062502, 2010.

[144] M. Levin, A. P. McCauley, A. W. Rodriguez, M. T. H. Reid, and S. G. Johnson, "Casimir repulsion between metallic objects in vacuum," *Phys. Rev. Lett.*, vol. 105, p. 090403, 2010.

[145] V. K. Pappakrishnan, P. C. Mundru, and D. A. Genov, "Repulsive casimir force in magnetodielectric plate configurations," *Phys. Rev. B*, vol. 89, p. 045430, 2014.

[146] N. Inui, "Levitation of a metallic sphere near gas-liquid and liquid-liquid interfaces by the repulsive casimir force," *Physical Review A - Atomic, Molecular, and Optical Physics*, vol. 89, no. 6, p. 062506, 2014.

[147] D. A. T. Somers and J. N. Munday, "Conditions for repulsive casimir forces between identical birefringent materials," *Phys. Rev. A*, vol. 95, p. 022509, 2017.

[148] V. B. Svetovoy, P. J. van Zwol, G. Palasantzas, and J. T. M. De Hosson, "Optical properties of gold films and the casimir force," *Phys. Rev. B*, vol. 77, p. 35439, 2008.

[149] S. K. Lamoreaux, "casimir forces: Still surprising after 60 years," *Physics Today*, vol. 60, no. 2, pp. 40–45, 2007.

[150] G. Palasantzas, M. Sedighi, and V. B. Svetovoy, "Applications of casimir forces: Nanoscale actuation and adhesion," *Applied Physics Letters*, vol. 117, no. 12, p. 120501, 2020.

[151] J. T. Mendonça, R. Bingham, P. K. Shukla, and D. Resendes, "Casimir effect in a turbulent plasma," *Physics Letters A*, vol. 289, no. 4, pp. 233–239, 2001.

[152] P. Lähteenmäki, G. S. Paraoanu, J. Hassel, and P. J. Hakonen, "Dynamical casimir effect in a Josephson metamaterial," *Proceedings of the National Academy of Sciences of the United States of America*, vol. 110, pp. 4234–4238, 2013.

[153] M. Camacho, T. Gong, B. Spreng, I. Liberal, N. Engheta, , and J. N. Munday, "Engineering casimir interactions with epsilon-near-zero materials," *Phys. Rev. A*, vol. 105, p. L061501, 2022.

[154] W. M. R. Simpson, *Surprises in Theoretical casimir Physics: Quantum Forces in Inhomogeneous Media*. New York: Springer, 2015.

[155] F. Intravaia, S. Koev, W. A. Jung, A. A. Talin, P. S. Davids, R. S. Decca, V. A. Aksyuk, D. A. R. Dalvit, and D. López, "Strong casimir force reduction through metallic surface nanostructuring," *Nature Communications*, vol. 4, p. 2515, 2013.

[156] D. Pérez-Morelo, A. Stange, R. W. Lally, L. K. Barrett, M. Imboden, A. Som, D. K. Campbell, V. A. Aksyuk, and D. J. Bishop, "a system for probing casimir energy corrections to the condensation energy," *Microsystems and Nanoengineering*, vol. 6, p. 115, 2020.

[157] G. Wang, P. Nowakowski, N. F. Bafi, B. Midtvedt, F. Schmidt, A. Callegari, R. Verre, M. Käll, S. Dietrich, S. Kondrat, and G. Volpe, "Nanoalignment by critical casimir torques," *Nature Communications*, vol. 15, p. 5086, 2024.

[158] A. Strange, M. Imboden, J. Javor, L. K. Barrett, and D. J. Bishop, "Building a casimir metrology platform with a commercial mems sensor," *Microsyst. Nanoeng.*, vol. 5, p. 14, 2019.

[159] T. Gong, M. R. Corrado, A. R. Mahbub, C. Shelden, and J. N. Munday, "Recent progress in engineering the casimir effect – applications to nanophotonics, nanomechanics, and chemistry," *Frontiers in Optics and Photonics*, vol. 10, pp. 523–536, 2021.

[160] Y. T. Beni, A. Koochi, and M. Abadyan, "Theoretical study of the effect of Casimir force, elastic boundary conditions and size dependency on the pull-in instability of beam-type NEMS," *Physica E: Low-dimensional Systems and Nanostructures*, vol. 43, pp. 979–988, 2011.

[161] J. Zou, Z. Marcet, A. W. Rodriguez, M. T. H. Reid, A. P. McCauley, I. I. Kravchenko, T. Lu, Y. Bao, S. G. Johnson, and H. B. Chan, "Casimir forces on a silicon micromechanical chip," *Nature Communications*, vol. 4, p. 1845, 2013.

[162] A. Farrokhabadi, N. Abadian, R. Rach, and M. Abadyan, "Theoretical modeling of the casimir force-induced instability in freestanding nanowires with circular cross-section," *Physica E: Low-dimensional Systems and Nanostructures*, vol. 63, pp. 67–80, 2014.

[163] M. Beauregard, G. Fucci, K. Kirsten, and P. Morales, "Casimir effect in the presence of external fields," *Journal of Physics A: Mathematical and Theoretical*, vol. 46, p. 115401, 2013.

[164] Y. Zhang, H. Zhang, X. Wang, Y. Wang, Y. Liu, S. Li, T. Zhang, C. Fan, and C. Zeng, "Magnetic-field tuning of the Casimir force," *Nature Physics*, vol. 20, pp. 1282–1287, 2024.

[165] R. Zhao, L. Li, S. Yang, W. Bao, Y. Xia, P. Ashby, Y. Wang, and X. Zhang, "Stable casimir equilibria and quantum trapping," *Science*, vol. 364, pp. 984–987, 2019.

[166] V. A. Parsegian, *van der Waals forces: a handbook for biologists, chemists, engineers, and physicists.* New York: Cambridge University Press, 2006.

[167] T. Ederth, "Template-stripped gold surfaces with 0.4-nm rms roughness suitable for force measurements: application to the Casimir force in the 20–100-nm range," *Phys. Rev. A*, vol. 62, p. 62104, 2000.

[168] J. N. Israelachvili, *Intermolecular and Surface Forces.* Elsevier, 2010.

[169] S. A. Ellingsen, "Casimir attraction in multilayered plane parallel magnetodielectric systems," *Journal of Physics A: Mathematical and Theoretical*, vol. 40, pp. 1951–1961, 2007.

[170] M. M. Gudarzi and S. H. Aboutalebi, "Self-consistent dielectric functions of materials: Toward accurate computation of casimir – van der Waals forces," *Science Advances*, vol. 7, p. eabg2272, 6 2024.

[171] B. E. Sernelius, "Casimir effects in systems containing 2d layers such as graphene and 2D electron gases," *Journal of Physics: Condensed Matter*, vol. 27, p. 214017, 2015.

[172] M.-S. Tomaš, "Casimir effect across a layered medium," *International Journal of Modern Physics: Conference Series*, vol. 14, pp. 561–565, 2012.

[173] L. F. Shampine, "Vectorized adaptive quadrature in matlab," *Journal of Computational and Applied Mathematics*, vol. 211, no. 2, pp. 131–140, 2008.

[174] A. Roy, C.-Y. Lin, and U. Mohideen, "Improved precision measurement of the casimir force," *Phys. Rev. D*, vol. 60, p. 111101, 1999.

[175] U. Mohideen and A. Roy, "Precision measurement of the casimir force from 0.1 to $0.9 \mu m$," *Phys. Rev. Lett.*, vol. 81, pp. 4549–4552, 1998.

[176] A. A. Amooey, "Improved mixing rules for description of the permittivity of mixtures," *Journal of Molecular Liquids*, vol. 180, pp. 31–33, 2013.

[177] J. C. R. Reis, T. P. Iglesias, G. Douhéret, and M. I. Davis, "The permittivity of thermodynamically ideal liquid mixtures and the excess relative permittivity of binary dielectrics," *Phys. Chem. Chem. Phys.*, vol. 11, no. 20, pp. 3977–3986, 2009.

[178] J. Siegel, R. Krajcar, Z. Kolská, V. Hnatowicz, and V. Svorčík, "Annealing of gold nanostructures sputtered on polytetrafluoroethylene." *Nanoscale. Res. Lett.*, vol. 6, no. 1, p. 588, 2011.

[179] S. Sauter and C. Schwab, *Boundary Element Methods.* Springer-Verlag, Berlin, 2010.

[180] M. Hassan, "Mathematical analysis of boundary integral equations and domain decomposition methods with applications in polarisable electrostatics," Ph.D. dissertation, RWTH Aachen University, 2020.

Appendix A

General Derivations of Many-Body Framework

A.1 Mathematical considerations

This section contains some additional mathematical considerations such as more details about our mathematical assumptions, the properties of the mathematical objects used in this article and a precise definition of the Galerkin approximation space that we use.

To begin with, we assume that the external harmonic potential we consider satifies $\Phi_{\mathsf{ext}} \in H^1_{\mathrm{loc}}(\mathbb{R}^3)$ with the associated *external* electric field $\mathbf{E}_{\mathsf{ext}} := -\nabla\Phi_{\mathsf{ext}} \in L^2_{\mathrm{loc}}(\mathbb{R}^3)$, where $L^2_{\mathrm{loc}}(\mathbb{R}^3)$ and $H^1_{\mathrm{loc}}(\mathbb{R}^3)$ denote the spaces of locally square integrable functions and locally square integrable functions with locally square integrable first derivatives, respectively. Next, we emphasise that, as is common in the mathematical literature, the solution to the PDE (4), i.e., the perturbed electrostatic potential Φ, is typically understood as an element of the space $H^1(\Omega^-) \cup H^1(\Omega^+)$ and is therefore not, in general, continuous. Strictly speaking therefore, the transmission conditions in Equation (4) must be understood in the sense of so-called Dirichlet and Neumann traces in the Sobolev spaces $H^{\frac{1}{2}}(\partial\Omega)$ and $H^{-\frac{1}{2}}(\partial\Omega)$ respectively. A detailed description of trace operators and fractional Sobolev spaces is beyond the scope of this article and can, for instance, be found in [179].

Concerning the mapping properties of the single layer potential and boundary operators, it can be shown that for any $s \in \mathbb{R}$, the mapping $\mathcal{S}$ extends as a bounded linear map from the Sobolev space $H^s(\partial\Omega)$ to $H^{s+32}_{\mathrm{loc}}(\mathbb{R}^3)$ and the operator $\mathcal{V}$ extends as an *invertible*, bounded linear map from $H^s(\partial\Omega)$ to $H^{s+1}(\partial\Omega)$ (see, e.g., [179] for a concise exposition on Sobolev spaces and for precise definitions and properties of the single layer potential). "Local" versions of the single layer potential and boundary operators which we have used frequently in this article are formally defined as follows: For each $i \in \{1, \ldots, N\}$, we have

$$(\mathcal{S}_i\nu_i)(\mathbf{x}) := \int_{\partial\Omega_i} \frac{\nu_i(\mathbf{y})}{4\pi|\mathbf{x} - \mathbf{y}|}\, d\mathbf{y}, \qquad \forall\mathbf{x} \in \Omega_i \cup \mathbb{R}^3 \setminus \overline{\Omega_i}, \quad \forall\nu_i \in H^s(\partial\Omega_i),\ s \in \mathbb{R},$$

$$(\mathcal{V}_i\nu_i)(\mathbf{x}) := \int_{\partial\Omega_i} \frac{\nu_i(\mathbf{y})}{4\pi|\mathbf{x} - \mathbf{y}|}\, d\mathbf{y}, \qquad \forall\mathbf{x} \in \partial\Omega_i, \qquad \forall\nu_i \in H^s(\partial\Omega_i),\ s \in \mathbb{R}.$$

In addition, we have used extensively in this article, the so-called Dirichlet-to-Neumann map, denoted DtN. Mathematically, the map $\mathrm{DtN}\colon H^s(\partial\Omega) \to H^{s-1}(\partial\Omega)$, $s \in \mathbb{R}$ is defined as follows: Given some boundary function $\lambda \in H^s(\partial\Omega)$, let u_λ denote the harmonic extension of λ in Ω^-. Then $\mathrm{DtN}\lambda \in H^{s-1}(\partial\Omega)$ is the normal

derivative (more precisely, the Neumann trace) of u_λ on the boundary $\partial\Omega$. We emphasise that in contrast to the single layer potential and boundary operator, the DtN map is a purely local operator, i.e., for any $\lambda \in H^s(\partial\Omega)$, $\mathrm{DtN}\lambda|_{\partial\Omega_i}$ depends only on $\lambda|_{\partial\Omega_i}$.

Concerning the regularity of solutions to the BIE (6), we recall from Equation (2) that the point-charge contribution σ_p to the free surface charge is assumed to be a linear combination of Dirac delta distributions. It is possible to show therefore that σ_p is an element of the Sobolev space $H^r(\partial\Omega)$ for every $r < -1$. In view of the regularising property of the single layer boundary operator $\mathcal{V}$, we can conclude that the right-hand side of the BIE (6) is, in general, an element of $H^r(\partial\Omega)$ for every $r < 0$. This implies in particular that solutions to the BIE (6) are <u>not</u>, in general, square integrable functions. On the other hand, we recall that $\sigma_s \in L^2(\partial\Omega)$ by assumption so that solutions to the BIE (9) can be readily understood as elements of the Sobolev space $H^1(\partial\Omega)$.

Finally, let us state the definition of the approximation space used in the proposed Galerkin discretisation.

Definition (Spherical Harmonics) For every integer $\ell \in \mathbb{N} \cup \{0\}$ and $m \in \{-\ell, \ldots, \ell\}$ we define $\mathcal{Y}_\ell^m \colon \mathbb{S}^2 \to \mathbb{R}$ as the real-valued L^2-orthonormal spherical harmonic of degree ℓ and order m on the unit sphere $\mathbb{S}^2$ (see [180] for a precise, constructive definition).

The set of spherical harmonics is dense in $L^2(\mathbb{S}^2)$ and is therefore well-suited for the choice of basis functions in the Galerkin discretisation of BIE (9).

Definition (Approximation Spaces) Let $\ell_{\max} \in \mathbb{N}$ be a discretisation parameter. First, on each sphere $\partial\Omega_i$, $i = 1, \ldots, N$ we define a local approximation space $W^{\ell_{\max}}(\partial\Omega_i)$ as

$$W^{\ell_{\max}}(\partial\Omega_i) := \left\{ u \colon \partial\Omega_i \to \mathbb{R} \quad \text{such that} \quad u(\mathbf{x}) = \sum_{\ell=0}^{\ell_{\max}} \sum_{m=-\ell}^{m=+\ell} [u]_\ell^m \mathcal{Y}_{\ell m}^i(\mathbf{x}) \right\},$$

with $[u]_\ell^m \in \mathbb{R}$, and where we introduced for notational convenience the basis functions $\mathcal{Y}_{\ell m}^i \colon \partial\Omega_i \to \mathbb{R}$ as

$$\mathcal{Y}_{\ell m}^i(\mathbf{x}) := \mathcal{Y}_\ell^m \left(\frac{\mathbf{x} - \mathbf{x}_i}{|\mathbf{x} - \mathbf{x}_i|} \right) \qquad \forall \mathbf{x} \in \partial\Omega_i.$$

Next, we define the global approximation space $W^{\ell_{\max}}$ as

$$W^{\ell_{\max}} := \left\{ u \colon \partial\Omega \to \mathbb{R} \text{ such that } \forall i \in \{1, \ldots, N\} \colon u|_{\partial\Omega_i} \in W^{\ell_{\max}}(\partial\Omega_i) \right\}.$$

A.2   Mathematical Proofs of Theorems 2.1 and 2.2

In this section we provide proofs of Theorems 2.2.1 and 2.2.2 from Section 2.2.4. For technical reasons, it is useful to begin with the proof of Theorem 2.2. This result shows that the definition of the interaction energy that we have provided in this article using quantities of interest from the integral equation (6) is consistent with the electric field-based definition of the interaction energy as derived directly from the PDEs (3) and (4). Throughout this section, we will use the notation and setting introduced in Sections 2.1, 2.2 and 2.4.

A.2.1 Proof of Theorem 2.2

Let $j \in \{1, \ldots, N\}$ and let $\mathbb{B}_r$ be an open ball large enough so that $\Omega^- \subset \mathbb{B}_r$. We begin by defining precisely $\mathbf{E}^{jj}$, i.e., the electric field produced *only due to the sphere* $\partial\Omega_j$ in the absence of both the external field $\mathbf{E}_{\mathsf{ext}}$ as well as the other spheres. Maxwell's equations imply that $\mathbf{E}^{jj} := -\nabla\Phi^{jj}$ where the self-potential Φ^{jj} satisfies the PDE (c.f., Equation (4))

$$
\begin{aligned}
-\Delta\Phi^{jj} &= 0 & &\text{in } \Omega_j \cup \mathbb{R}^3 \setminus \overline{\Omega_j} \\
[\![\Phi^{jj}]\!] &= 0 & &\text{on } \partial\Omega_j, \\
[\![\kappa\nabla\Phi^{jj}]\!] &= \sigma_{s,j} + \sigma_{p,j} & &\text{on } \partial\Omega_j, \\
|\Phi^{jj}| &\to 0 & &\text{as } |\mathbf{x}| \to \infty,
\end{aligned}
\tag{A.1}
$$

where we remind the reader that $\sigma_{s,j} := \sigma_s|_{\partial\Omega_j}$ and $\sigma_{p,j} := \sigma_p|_{\partial\Omega_j}$.

Next, to aid the subsequent exposition, we define the auxiliary quantity

$$
\mathcal{E}^r_{\mathsf{PDE,int}} := \int_{\mathbb{B}_r} \kappa(\mathbf{x})\mathbf{E}_{\mathsf{tot}}(\mathbf{x}) \cdot \mathbf{E}_{\mathsf{tot}}(\mathbf{x})\, d\mathbf{x} - \sum_{j=1}^{N} \int_{\mathbb{B}_r} \kappa(\mathbf{x})\mathbf{E}^{jj}(\mathbf{x}) \cdot \mathbf{E}^{jj}(\mathbf{x})\, d\mathbf{x}
$$
$$
- \int_{\mathbb{B}_r} \kappa_0 \mathbf{E}_{\mathsf{ext}}(\mathbf{x}) \cdot \mathbf{E}_{\mathsf{ext}}(\mathbf{x})\, d\mathbf{x}. \tag{A.2}
$$

We may now use simple algebra and the fact that $\Phi_{\mathsf{tot}} = \Phi + \Phi_{\mathsf{ext}}$ (see Section 2.1) to deduce that

$$
\mathcal{E}^r_{\mathsf{PDE,int}} = \int_{\mathbb{B}_r} \kappa(\mathbf{x})|\nabla\Phi(\mathbf{x})|^2\, d\mathbf{x} + 2\int_{\mathbb{B}_r} \kappa(\mathbf{x})\nabla\Phi(\mathbf{x}) \cdot \nabla\Phi_{\mathsf{ext}}(\mathbf{x})\, d\mathbf{x}
$$
$$
- \sum_{j=1}^{N} \int_{\mathbb{B}_r} \kappa(\mathbf{x})|\nabla\Phi^{jj}(\mathbf{x})|^2\, d\mathbf{x} + \int_{\mathbb{B}_r} (\kappa(\mathbf{x}) - \kappa_0)|\nabla\Phi_{\mathsf{ext}}(\mathbf{x})|^2\, d\mathbf{x}.
$$

Next, we recall from the PDEs (3) and (4) that Φ is harmonic on $\Omega^- \cup \Omega^+$, Φ_{ext} is harmonic on $\mathbb{R}^3$, and Φ^{jj} is harmonic on $\Omega_j \cup (\mathbb{R}^3 \setminus \overline{\Omega_j})$. Therefore we can appeal to Green's first identity to simplify the above integrals.

Recalling the interface conditions from the PDEs (4) and (A.1), we can further simplify several of these integral as

$$
\int_{\partial\Omega} [\![\kappa\nabla\Phi]\!](\mathbf{x})\Phi(\mathbf{x})\, d\mathbf{x} = (\sigma_s + \sigma_p + \sigma_{\mathsf{ext}}, \Phi)_{L^2(\partial\Omega)},
$$
$$
2\int_{\partial\Omega} [\![\kappa\nabla\Phi]\!](\mathbf{x})\Phi_{\mathsf{ext}}(\mathbf{x})\, d\mathbf{x} = 2(\sigma_s + \sigma_p + \sigma_{\mathsf{ext}}, \Phi_{\mathsf{ext}})_{L^2(\partial\Omega)},
$$
$$
\sum_{j=1}^{N} \int_{\partial\Omega_j} (\kappa_j - \kappa_0)\partial_n\Phi^{jj}(\mathbf{x})\Phi^{jj}(\mathbf{x})\, d\mathbf{x} = \sum_{j=1}^{N} (\sigma_{s,j} + \sigma_{p,j}, \Phi^{jj})_{L^2(\partial\Omega_j)},
$$
$$
\int_{\partial\Omega} (\kappa(\mathbf{x}) - \kappa_0)\partial_n\Phi_{\mathsf{ext}}(\mathbf{x})\Phi_{\mathsf{ext}}(\mathbf{x})\, d\mathbf{x} = -(\sigma_{\mathsf{ext}}, \Phi_{\mathsf{ext}})_{L^2(\partial\Omega)},
$$

where we remind the reader that $\sigma_{\mathsf{ext}} = -(\kappa - \kappa_0)\partial_n\Phi_{\mathsf{ext}}$. Using the fact that λ, λ_{ext} and λ^{jj} are the restrictions on the spheres of the potentials Φ, Φ_{ext}, and Φ^{jj} respectively, we can deduce that

$$\mathcal{E}^r_{\text{PDE,int}} = \big(\sigma_s + \sigma_p + \sigma_{\text{ext}},\ \lambda\big)_{L^2(\partial\Omega)} + 2\big(\sigma_s + \sigma_p,\ \lambda_{\text{ext}}\big)_{L^2(\partial\Omega)} +$$

$$\big(\sigma_{\text{ext}},\ \lambda^{\ell_{\max}}_{\text{ext}}\big)_{L^2(\partial\Omega)} - \sum_{j=1}^{N} \big(\sigma_{s,j} + \sigma_{p,j},\ \lambda^{jj}\big)_{L^2(\partial\Omega_j)}$$

$$+ \int_{\partial\mathbb{B}_r} \kappa_0 \left(\partial_n \Phi(\mathbf{x})\Phi(\mathbf{x}) - \sum_{j=1}^{N} \partial_n \Phi^{jj}(\mathbf{x})\Phi^{jj}(\mathbf{x}) \right) d\mathbf{x} +$$

$$2 \int_{\partial\mathbb{B}_r} \kappa_0 \partial_n \Phi(\mathbf{x})\Phi_{\text{ext}}(\mathbf{x})\, d\mathbf{x} = \mathcal{E}_{\text{int}}.$$

Comparing this final expression with Equation (A.2) allows us to deduce the required result (28).

Next, we will prove Theorem 2.1 which shows that Definition (24) of the approximate electrostatic forces is consistent with the usual notion in the chemistry literature of the forces as the negative sphere-centered gradients of the electrostatic interaction energy. In order to present a concise and well-structured proof, we will first prove two lemmas.

Lemma A.2.1 *Let $\lambda_{\ell_{\max}}$ denote the solution to the Galerkin discretisation (18) for a given free charge $\sigma_f = \sigma_s + \sigma_p$ and external electric field $\mathbf{E}_{\text{ext}}$. Additionally, let $\nu_{\ell_{\max}}$ denote the approximate induced surface corresponding to $\lambda_{\ell_{\max}}$ and let $\mathbf{E}^i_{\text{exc}}$, $i \in \{1, \ldots, N\}$ denote the i-excluded electric fields generated by $\nu_{\ell_{\max}}$ as defined through Definition (17). Then for each $i \in \{1, \ldots, N\}$ it holds that*

$$\frac{1}{2}\nabla_{\mathbf{x}_i}\Big(\sigma_s + \sigma_p + \sigma_{\text{ext}}, \lambda_{\ell_{\max}}\Big)_{L^2(\partial\Omega)} = -\kappa_0\big(\nu_{\ell_{\max}}, \mathbf{E}^i_{\text{exc}}\big)_{L^2(\partial\Omega_i)} + \big(\nabla_{\mathbf{x}_i}\sigma_{\text{ext}}, \lambda_{\ell_{\max}}\big)_{L^2(\partial\Omega_i)}.$$

Proof: Let $i \in \{1, \ldots, N\}$ be fixed. A simple application of the product rule yields that

$$\frac{1}{2}\nabla_{\mathbf{x}_i}\Big(\sigma_s + \sigma_p + \sigma_{\text{ext}}, \lambda_{\ell_{\max}}\Big)_{L^2(\partial\Omega)} = \frac{1}{2}\Big(\nabla_{\mathbf{x}_i}\left(\sigma_s + \sigma_p + \sigma_{\text{ext}}\right), \lambda_{\ell_{\max}}\Big)_{L^2(\partial\Omega)}$$

$$+ \frac{1}{2}\Big(\sigma_s + \sigma_p + \sigma_{\text{ext}}, \nabla_{\mathbf{x}_i}\lambda_{\ell_{\max}}\Big)_{L^2(\partial\Omega)}.$$

Using the fact that both σ_s and σ_p are independent of changes in the locations $\{\mathbf{x}_i\}_{i=1}^{N}$ of the sphere centres locations, [180] we further obtain that

$$\frac{1}{2}\nabla_{\mathbf{x}_i}\Big(\sigma_s + \sigma_p + \sigma_{\text{ext}}, \lambda_{\ell_{\max}}\Big)_{L^2(\partial\Omega)} = \frac{1}{2}\Big(\nabla_{\mathbf{x}_i}\sigma_{\text{ext}}, \lambda_{\ell_{\max}}\Big)_{L^2(\partial\Omega)}$$

$$+ \frac{1}{2}\Big(\sigma_s + \sigma_p + \sigma_{\text{ext}}, \nabla_{\mathbf{x}_i}\lambda_{\ell_{\max}}\Big)_{L^2(\partial\Omega)}.$$

Finally, it is straightforward to see that in fact

$$\frac{1}{2}\Big(\nabla_{\mathbf{x}_i}\sigma_{\text{ext}}, \lambda_{\ell_{\max}}\Big)_{L^2(\partial\Omega)} = \frac{1}{2}\Big(\nabla_{\mathbf{x}_i}\sigma_{\text{ext}}, \lambda_{\ell_{\max}}\Big)_{L^2(\partial\Omega_i)}$$

so that we obtain the expression

$$\frac{1}{2}\nabla_{\mathbf{x}_i}\Big(\left(\sigma_s + \sigma_p + \sigma_{\text{ext}}\right), \lambda_{\ell_{\max}}\Big)_{L^2(\partial\Omega)} = \frac{1}{2}\Big(\nabla_{\mathbf{x}_i}\sigma_{\text{ext}}, \lambda_{\ell_{\max}}\Big)_{L^2(\partial\Omega_i)} \qquad (A.3)$$

$$+ \frac{1}{2}\Big(\left(\sigma_s + \sigma_p + \sigma_{\text{ext}}\right), \nabla_{\mathbf{x}_i}\lambda_{\ell_{\max}}\Big)_{L^2(\partial\Omega)}. \qquad (A.4)$$

Consequently, it remains to compute the sphere-centred gradient of $\lambda_{\ell_{\max}}$. This is a slightly technical task so to aid the subsequent exposition, we first introduce some additional notation.

Notation: We define the vectors and matrices $\boldsymbol{\sigma}, \boldsymbol{\sigma}^{\mathbf{ext}}, \boldsymbol{DtN}^{\kappa}$ and $\boldsymbol{V}$ as

$$[\boldsymbol{\sigma}_i]_\ell^m := \left(\sigma_s + \sigma_p, \mathcal{Y}_{\ell m}^i\right)_{L^2(\partial\Omega_i)},$$

$$[\boldsymbol{\sigma}_i^{\mathbf{ext}}]_\ell^m := \left(\sigma_{\mathsf{ext}}, \mathcal{Y}_{\ell m}^i\right)_{L^2(\partial\Omega_i)},$$

$$[\boldsymbol{DtN}_{ij}^{\kappa}]_{\ell\ell'}^{mm'} := \delta_{ij} \left(\frac{\kappa_j - \kappa_0}{\kappa_0} \mathrm{DtN}\mathcal{Y}_{\ell'm'}^j, \mathcal{Y}_{\ell m}^i\right)_{L^2(\partial\Omega_i)},$$

$$[\boldsymbol{V}_{ij}]_{\ell\ell'}^{mm'} := \left(\mathcal{V}\mathcal{Y}_{\ell'm'}^j, \mathcal{Y}_{\ell m}^i\right)_{L^2(\partial\Omega_i)},$$

where $i, j \in \{1, \ldots, N\}$, $\ell, \ell' \in \{0, \ldots, \ell_{\max}\}$ and $|m| \leq \ell$, $|m'| \leq \ell'$. Additionally, we recall that the Galerkin discretisation (18) is equivalent to the linear system of equations

$$\boldsymbol{A}\boldsymbol{\lambda} := (\boldsymbol{I} - \boldsymbol{V}\, \boldsymbol{DtN}^{\kappa})\boldsymbol{\lambda} = \boldsymbol{F}, \tag{A.5}$$

where $\boldsymbol{\lambda}$ and $\boldsymbol{F}$ are defined by (20) and (21) respectively.

Equipped with the notation introduced above, we now take the gradient on both sides of Equation (A.5). Using the product rule together with the fact that the Dirichlet-to-Neumann map is independent of changes in the locations $\{\mathbf{x}_i\}_{i=1}^N$ of the sphere centers, we obtain that

$$\nabla_{\mathbf{x}_i}\boldsymbol{\lambda} + \left(\nabla_{\mathbf{x}_i}\boldsymbol{V}\right)\boldsymbol{DtN}^{\kappa}\boldsymbol{\lambda} + \boldsymbol{V}\boldsymbol{DtN}^{\kappa}\nabla_{\mathbf{x}_i}\boldsymbol{\lambda} = \frac{1}{\kappa_0}\left(\nabla_{\mathbf{x}_i}\boldsymbol{V}\right)\left(\boldsymbol{\sigma} + \boldsymbol{\sigma}^{\mathbf{ext}}\right) + \frac{1}{\kappa_0}\boldsymbol{V}\nabla_{\mathbf{x}_i}\boldsymbol{\sigma}^{\mathbf{ext}},$$

or equivalently, after collecting terms

$$\boldsymbol{A}\nabla_{\mathbf{x}_i}\boldsymbol{\lambda} = \frac{1}{\kappa_0}\left(\nabla_{\mathbf{x}_i}\boldsymbol{V}\right)\left(\boldsymbol{\sigma} + \boldsymbol{\sigma}^{\mathbf{ext}} - \kappa_0\boldsymbol{DtN}^{\kappa}\boldsymbol{\lambda}\right) + \frac{1}{\kappa_0}\boldsymbol{V}\nabla_{\mathbf{x}_i}\boldsymbol{\sigma}^{\mathbf{ext}}. \tag{A.6}$$

Next, recalling that $\nu_{\ell_{\max}}$ satisfies Equation (23), it is easy to deduce that

$$\frac{1}{\kappa_0}\left(\nabla_{\mathbf{x}_i}\boldsymbol{V}\right)\left(\boldsymbol{\sigma} + \boldsymbol{\sigma}^{\mathbf{ext}} - \kappa_0\boldsymbol{DtN}^{\kappa}\boldsymbol{\lambda}\right) = \left(\nabla_{\mathbf{x}_i}\boldsymbol{V}\right)\boldsymbol{\nu},$$

where

$$[\boldsymbol{\nu}_i]_\ell^m := \left(\nu_{\ell_{\max}}, \mathcal{Y}_{\ell m}^i\right)_{L^2(\partial\Omega_i)},$$

with indices $i \in \{1, \ldots, N\}$, $\ell \in \{0, \ldots, \ell_{\max}\}$ and $|m| \leq \ell$. We therefore conclude from Equation (A.6) that

$$\nabla_{\mathbf{x}_i}\boldsymbol{\lambda} = \boldsymbol{A}^{-1}\left(\left(\nabla_{\mathbf{x}_i}\boldsymbol{V}\right)\boldsymbol{\nu}\right) + \frac{1}{\kappa_0}\boldsymbol{A}^{-1}\left(\boldsymbol{V}\nabla_{\mathbf{x}_i}\boldsymbol{\sigma}^{\mathbf{ext}}\right).$$

Recalling now the last term on the right-hand side of Equation (A.3), we deduce

that $\frac{1}{2}\Big(\sigma_s + \sigma_p + \sigma_{\text{ext}}, \nabla_{\mathbf{x}_i}\lambda_{\ell_{\max}}\Big)_{L^2}(\partial\Omega)$ is equal to

$$= \frac{1}{2}\Big(\boldsymbol{\sigma} + \boldsymbol{\sigma}^{\text{ext}}, \boldsymbol{A}^{-1}\big((\nabla_{\mathbf{x}_i}\boldsymbol{V})\boldsymbol{\nu}\big)\Big)_{\ell^2} + \frac{1}{2}\Big(\boldsymbol{\sigma} + \boldsymbol{\sigma}^{\text{ext}}, \frac{1}{\kappa_0}\boldsymbol{A}^{-1}\big(\boldsymbol{V}\nabla_{\mathbf{x}_i}\boldsymbol{\sigma}^{\text{ext}}\big)\Big)_{\ell^2}$$

$$= \frac{1}{2}\Big(\big(\boldsymbol{A^T}\big)^{-1}(\boldsymbol{\sigma} + \boldsymbol{\sigma}^{\text{ext}}), (\nabla_{\mathbf{x}_i}\boldsymbol{V})\boldsymbol{\nu}\Big)_{\ell^2} + \frac{1}{2}\frac{1}{\kappa_0}\Big(\big(\boldsymbol{A^T}\big)^{-1}(\boldsymbol{\sigma} + \boldsymbol{\sigma}^{\text{ext}}), \boldsymbol{V}\nabla_{\mathbf{x}_i}\boldsymbol{\sigma}^{\text{ext}}\Big)_{\ell^2}.$$

Next, a direct calculation and comparison with the Galerkin discretisation (18) reveals that

$$\big(\boldsymbol{A^T}\big)^{-1}(\boldsymbol{\sigma} + \boldsymbol{\sigma}^{\text{ext}}) = \kappa_0\boldsymbol{\nu}.$$

Using the definition of $\nu_{\ell_{\max}}$ as given by Equation (22), we obtain that $\frac{1}{2}\Big(\sigma_s + \sigma_p + \sigma_{\text{ext}}, \nabla_{\mathbf{x}_i}\lambda_{\ell_{\max}}\Big)_{L^2(\partial\Omega)}$ is equal to

$$= \frac{1}{2}\kappa_0\Big(\boldsymbol{\nu}, (\nabla_{\mathbf{x}_i}\boldsymbol{V})\boldsymbol{\nu}\Big)_{\ell^2} + \frac{1}{2}\Big(\boldsymbol{\nu}, \boldsymbol{V}\nabla_{\mathbf{x}_i}\boldsymbol{\sigma}^{\text{ext}}\Big)_{\ell^2}$$

$$= \frac{1}{2}\kappa_0\Big(\boldsymbol{\nu}, (\nabla_{\mathbf{x}_i}\boldsymbol{V})\boldsymbol{\nu}\Big)_{\ell^2} + \frac{1}{2}\Big(\boldsymbol{\lambda}, \nabla_{\mathbf{x}_i}\boldsymbol{\sigma}^{\text{ext}}\Big)_{\ell^2}$$

$$= \frac{1}{2}\kappa_0\Big(\nu_{\ell_{\max}}, (\nabla_{\mathbf{x}_i}\mathcal{V})\nu_{\ell_{\max}}\Big)_{L^2(\partial\Omega)} + \frac{1}{2}\Big(\lambda_{\ell_{\max}}, \nabla_{\mathbf{x}_i}\sigma_{\text{ext}}\Big)_{L^2(\partial\Omega)}$$

$$= \frac{1}{2}\kappa_0\Big(\nu_{\ell_{\max}}, (\nabla_{\mathbf{x}_i}\mathcal{V})\nu_{\ell_{\max}}\Big)_{L^2(\partial\Omega)} + \frac{1}{2}\Big(\lambda_{\ell_{\max}}, \nabla_{\mathbf{x}_i}\sigma_{\text{ext}}\Big)_{L^2(\partial\Omega_i)} \qquad (A.7)$$

Finally, a direct but tedious computation can be used to show that[57, 180]

$$\frac{1}{2}\kappa_0\Big(\nu_{\ell_{\max}}, (\nabla_{\mathbf{x}_i}\mathcal{V})\nu_{\ell_{\max}}\Big)_{L^2(\partial\Omega)} = -\kappa_0\Big(\nu_{\ell_{\max}}, \mathbf{E}^i_{\text{exc}}\Big)_{L^2(\partial\Omega_i)}. \qquad (A.8)$$

Combining therefore the developments (A.7) and (A.8) with Equation (A.3) now completes the proof.

Lemma A.2.2 *For a given external electric field* $\mathbf{E}_{\text{ext}} = -\nabla\Phi_{\text{ext}} \in L^2_{\text{loc}}(\mathbb{R}^3)$, *let* $\sigma_{\text{ext}} = -(\kappa - \kappa_0)\partial_n\Phi_{\text{ext}}$, *and let* $\psi \in H^{\frac{1}{2}}(\partial\Omega)$ *be arbitrary. Then for each* $i \in \{1, \ldots, N\}$ *it holds that*

$$(\nabla_{\mathbf{x}_i}\sigma_{\text{ext}}, \Psi)_{L^2(\partial\Omega_i)} = -(\kappa_i - \kappa_0)(\nabla_{\mathbf{x}_i}\lambda_{\text{ext}}, \text{DtN}\Psi)_{L^2(\partial\Omega_i)}. \qquad (A.9)$$

Proof: Recall the notation $\lambda_{\text{ext}} := \Phi_{\text{ext}}|_{\partial\Omega} \in H^{\frac{1}{2}}(\partial\Omega)$ and let $[\lambda_{\text{ext,i}}]^m_\ell$ and $[\Psi_i]^m_\ell$, $\ell \in \mathbb{N}_0$, $|m| \leq \ell$ denote the local spherical harmonics expansion coefficients of λ_{ext} and Ψ on the sphere $\partial\Omega_i$. Since Φ_{ext} is harmonic in $\mathbb{R}^3$ and therefore in particular on $\overline{\Omega_i}$, it follows that we can write

$$(\nabla_{\mathbf{x}_i}\sigma_{\text{ext}}, \Psi)_{L^2(\partial\Omega_i)} = -(\kappa_i - \kappa_0)(\nabla_{\mathbf{x}_i}\partial_n\Phi_{\text{ext}}, \Psi)_{L^2(\partial\Omega_i)}$$

$$= -(\kappa_i - \kappa_0)(\text{DtN}\lambda_{\text{ext}}, \Psi)_{L^2(\partial\Omega_i)}$$

$$= -(\kappa_i - \kappa_0)r_i^2\sum_{\ell=0}^{\ell=\infty}\sum_{m=-\ell}^{m=+\ell}\Big(\nabla_{\mathbf{x}_i}\frac{\ell}{r_i}[\lambda_{\text{ext,i}}]^m_\ell\Big)[\Psi_i]^m_\ell$$

$$= -(\kappa_i - \kappa_0)r_i^2\sum_{\ell=0}^{\ell=\infty}\sum_{m=-\ell}^{m=+\ell}\big(\nabla_{\mathbf{x}_i}[\lambda_{\text{ext,i}}]^m_\ell\big)\Big(\frac{\ell}{r_i}[\Psi_i]^m_\ell\Big)$$

$$= -(\kappa_i - \kappa_0)(\nabla_{\mathbf{x}_i}\lambda_{\text{ext}}, \text{DtN}\Psi)_{L^2(\partial\Omega_i)}.$$

A.2.2 Proof of Theorem 2.1

We are now ready to state the proof of Theorem 2.1. Before proceeding to the proof, let us simply remark that the relation (26) in Theorem 2.1 remains true if exact quantities are considered, i.e., if the force defined by (24) is built upon the exact induced charge ν being solution to the BIE (7) and where the energy corresponds to $\mathcal{E}_{\text{int}}$ as defined by (27).

Let $i \in \{1, \ldots, N\}$ be fixed. By the definition of the approximate electrostatic interaction energy, we have

$$-\nabla_{\mathbf{x}_i} \mathcal{E}_{\text{int}}^{\ell_{\max}} = \underbrace{-\frac{1}{2} \nabla_{\mathbf{x}_i} \big(\sigma_s + \sigma_p + \sigma_{\text{ext}}, \, \lambda_{\ell_{\max}} \big)_{L^2(\partial\Omega)}}_{:=(\text{I})} \underbrace{-\nabla_{\mathbf{x}_i} \big(\sigma_s + \sigma_p, \, \lambda_{\text{ext}}^{\ell_{\max}} \big)_{L^2(\partial\Omega)}}_{:=(\text{II})}$$

$$\underbrace{-\frac{1}{2} \nabla_{\mathbf{x}_i} \big(\sigma_{\text{ext}}, \, \lambda_{\text{ext}}^{\ell_{\max}} \big)_{L^2(\partial\Omega)}}_{:=(\text{III})} + \underbrace{\frac{1}{2} \nabla_{\mathbf{x}_i} \sum_{j=1}^{N} \big(\sigma_{s,j} + \sigma_{p,j}, \lambda_{\ell_{\max}}^{jj} \big)_{L^2(\partial\Omega_j)}}_{:=(\text{IV})}.$$

We now simplify each of the terms (I), (II), (III), and (IV). First, we observe that the self energy term (IV) is defined entirely through functions that are independent of changes in the location of the center $\mathbf{x}_i$ of the sphere $\partial\Omega_i$, even in the case $j = i$. This can be seen by noticing that $\big(\sigma_{s,i} + \sigma_{p,i}, \lambda_{\ell_{\max}}^{\ddot{u}} \big)_{L^2(\partial\Omega_i)}$ remains constant as one displaces $\mathbf{x}_i$ by any translation. Consequently, we obtain that $(\text{IV}) \equiv 0$.

The term (I) can be simplified using Lemmas A.2.1 and A.2.2 as

$$\begin{aligned}
(\text{I}) &= -\frac{1}{2} \nabla_{\mathbf{x}_i} \big(\sigma_s + \sigma_p + \sigma_{\text{ext}}, \lambda_{\ell_{\max}} \big)_{L^2(\partial\Omega)} \\
&= \kappa_0 \big(\nu_{\ell_{\max}}, \mathbf{E}_{\text{exc}}^i \big)_{L^2(\partial\Omega_i)} - \big(\nabla_{\mathbf{x}_i} \sigma_{\text{ext}}, \lambda_{\ell_{\max}} \big)_{L^2(\partial\Omega_i)} \qquad \text{(Lemma A.2.1)} \\
&= \underbrace{\kappa_0 \big(\nu_{\ell_{\max}}, \mathbf{E}_{\text{exc}}^i \big)_{L^2(\partial\Omega_i)}}_{:=(\text{IA})} + \underbrace{(\kappa_i - \kappa_0) \big(\nabla_{\mathbf{x}_i} \lambda_{\text{ext}}, \text{DtN}\lambda_{\ell_{\max}} \big)_{L^2(\partial\Omega_i)}}_{:=(\text{IB})}. \quad \text{(Lemma A.2.2)}
\end{aligned}$$

$$(\text{A}.10)$$

Next, we simplify the term (IB). Indeed, a direct calculation shows that

$$\begin{aligned}
(\text{IB}) &= (\kappa_i - \kappa_0) \big(\nabla_{\mathbf{x}_i} \lambda_{\text{ext}}, \text{DtN}\lambda_{\ell_{\max}} \big)_{L^2(\partial\Omega_i)} = (\kappa_i - \kappa_0) \int_{\partial\Omega_i} (\nabla_{\mathbf{x}_i} \Phi_{\text{ext}}) \text{DtN}\lambda_{\ell_{\max}} \, d\mathbf{x} \\
&= (\kappa_i - \kappa_0) \int_{\partial\Omega_i} (\nabla_{\mathbf{x}} \Phi_{\text{ext}}) \text{DtN}\lambda_{\ell_{\max}} \, d\mathbf{x} = -(\kappa_i - \kappa_0) \int_{\partial\Omega_i} \mathbf{E}_{\text{ext}} \text{DtN}\lambda_{\ell_{\max}} \, d\mathbf{x} \\
&= -(\kappa_i - \kappa_0) \big(\text{DtN}\lambda_{\ell_{\max}}, \mathbf{E}_{\text{ext}} \big)_{L^2(\partial\Omega_i)}, \qquad\qquad\qquad\qquad\qquad\qquad (\text{A}.11)
\end{aligned}$$

where the second line follows from a similar calculation as done to obtain Equation (A.8).

In order to simplify the term (II), we again recall that the free charges σ_s, σ_p are independent of changes in the location of the centre $\mathbf{x}_i$ of the sphere $\partial\Omega_i$. Consequently, we obtain that II is

$$\begin{aligned}
-\nabla_{\mathbf{x}_i} \big(\sigma_s + \sigma_p, \lambda_{\text{ext}}^{\ell_{\max}} \big)_{L^2(\partial\Omega)} &= -\big(\sigma_s + \sigma_p, \, \nabla_{\mathbf{x}_i} \lambda_{\text{ext}}^{\ell_{\max}} \big)_{L^2(\partial\Omega)} \\
&= -\big(\sigma_s + \sigma_p, \, \nabla_{\mathbf{x}_i} \lambda_{\text{ext}}^{\ell_{\max}} \big)_{L^2(\partial\Omega)_i}. \qquad (\text{A}.12)
\end{aligned}$$

Therefore, using a calculation similar to the one used to obtain Equation (A.11), we deduce that

$$(\text{II}) = -\big(\sigma_s + \sigma_p,\ \nabla_{\mathbf{x}_i}\lambda_{\text{ext}}^{\ell_{\max}}\big)_{L^2(\partial\Omega_i)} = \big(\sigma_s^{\ell_{\max}} + \sigma_p^{\ell_{\max}},\ \mathbf{E}_{\text{ext}}\big)_{L^2(\partial\Omega_i)}, \qquad (\text{A.13})$$

where $\sigma_s^{\ell_{\max}}$ and $\sigma_p^{\ell_{\max}}$ are the best approximations in $W^{\ell_{\max}}$ of σ_s and σ_p respectively.

Next, we attempt to simplify the term (III). A simple application of the product rule together with Lemma A.2.2 yields that

$$
\begin{aligned}
(\text{III}) &= -\frac{1}{2}\nabla_{\mathbf{x}_i}\big(\sigma_{\text{ext}},\ \lambda_{\text{ext}}^{\ell_{\max}}\big)_{L^2(\partial\Omega)} = -\frac{1}{2}\nabla_{\mathbf{x}_i}\big(\sigma_{\text{ext}},\ \lambda_{\text{ext}}^{\ell_{\max}}\big)_{L^2(\partial\Omega_i)} \\
&= -\frac{1}{2}\big(\nabla_{\mathbf{x}_i}\sigma_{\text{ext}},\ \lambda_{\text{ext}}^{\ell_{\max}}\big)_{L^2(\partial\Omega_i)} - \frac{1}{2}\big(\sigma_{\text{ext}},\ \nabla_{\mathbf{x}_i}\lambda_{\text{ext}}^{\ell_{\max}}\big)_{L^2(\partial\Omega_i)} \\
&= (\kappa_i - \kappa_0)\big(\text{DtN}\lambda_{\text{ext}},\ \nabla_{\mathbf{x}_i}\lambda_{\text{ext}}^{\ell_{\max}}\big)_{L^2(\partial\Omega_i)} - \frac{1}{2}\big(\sigma_{\text{ext}},\ \nabla_{\mathbf{x}_i}\lambda_{\text{ext}}^{\ell_{\max}}\big)_{L^2(\partial\Omega_i)} \\
&= -\big(\sigma_{\text{ext}},\ \nabla_{\mathbf{x}_i}\lambda_{\text{ext}}^{\ell_{\max}}\big)_{L^2(\partial\Omega_i)}.
\end{aligned}
$$

Once again, a direct calculation of the form used to obtain Equation (A.11) allows us to conclude that

$$(\text{III}) = -\big(\sigma_{\text{ext}},\ \nabla_{\mathbf{x}_i}\lambda_{\text{ext}}^{\ell_{\max}}\big)_{L^2(\partial\Omega_i)} = \big(\sigma_{\text{ext}}^{\ell_{\max}},\ \mathbf{E}_{\text{ext}}\big)_{L^2(\partial\Omega_i)}. \qquad (\text{A.14})$$

Combining now Equations (A.10), (A.11), (A.13), and (A.14) we obtain that

$$
\begin{aligned}
-\nabla_{\mathbf{x}_i}\mathcal{E}_{\text{int}}^{\ell_{\max}} &= (\text{IA}) + (\text{IB}) + (\text{II}) + (\text{III}) \\
&= \kappa_0\big(\nu_{\ell_{\max}},\mathbf{E}_{\text{exc}}^i\big)_{L^2(\partial\Omega_i)} - (\kappa_i - \kappa_0)\big(\text{DtN}\lambda_{\ell_{\max}},\mathbf{E}_{\text{ext}}\big)_{L^2(\partial\Omega_i)} \\
&\quad + \big(\sigma_s^{\ell_{\max}} + \sigma_p^{\ell_{\max}},\ \mathbf{E}_{\text{ext}}\big)_{L^2(\partial\Omega_i)} + \big(\sigma_{\text{ext}}^{\ell_{\max}},\ \mathbf{E}_{\text{ext}}\big)_{L^2(\partial\Omega_i)} \\
&= \kappa_0\big(\nu_{\ell_{\max}},\mathbf{E}_{\text{exc}}^i\big)_{L^2(\partial\Omega_i)} + \\
&\quad\quad \big(-(\kappa_i - \kappa_0)\text{DtN}\lambda_{\ell_{\max}} + \sigma_s^{\ell_{\max}} + \sigma_p^{\ell_{\max}} + \sigma_{\text{ext}}^{\ell_{\max}},\mathbf{E}_{\text{ext}}\big)_{L^2(\partial\Omega_i)} \\
&= \kappa_0\big(\nu_{\ell_{\max}},\mathbf{E}_{\text{exc}}^i\big)_{L^2(\partial\Omega_i)} + \kappa_0\big(\nu_{\ell_{\max}},\mathbf{E}_{\text{ext}}\big)_{L^2(\partial\Omega_i)}.
\end{aligned}
$$

where the last equality follows from Equation (23). This completes the proof.

Appendix B

Aggregation Data

Table B.1: Energetic considerations and the percentage of aggregation for FeO - ice collisions at T = 150 K and $k_r = 0.9$ (the surface point charge model). FeO particle has the fixed radius and charge ($r_2 = 0.2$ nm, $q_2 = $ -1e), and the size and charge of ice particle is varied. The collision geometry is shown in Figure 3a.

ice particle	Coulomb barrier, E_{Coul}, meV	$v_{\text{rel}}^{\min}$, ms^{-1}	$v_{\text{rel}}^{\max}$, ms^{-1}	aggregation, %
$r_1 = 30$ nm; $q_1 = 0$	0	0	1007	100
$r_1 = 30$ nm; $q_1 = $ -1e	23.7	199	987	34.7
$r_1 = 30$ nm; $q_1 = $ -2e	55.3	303	1012	5.2
$r_1 = 20$ nm; $q_1 = 0$	0	0	1094	100
$r_1 = 20$ nm; $q_1 = $ -1e	35.7	244	1059	17.4
$r_1 = 20$ nm; $q_1 = $ -2e	82.9	372	1092	0.91
$r_1 = 10$ nm; $q_1 = 0$	0	0	1267	100
$r_1 = 10$ nm; $q_1 = $ -1e	71.3	345	1165	1.91
$r_1 = 10$ nm; $q_1 = $ -2e	165.9	526	1225	0

Table B.2: Energetic considerations and the percentage of aggregation for MgO - ice collisions at T = 150 K and $k_r = 0.9$ (the surface point charge model). MgO particle has the fixed radius and charge ($r_2 = 0.2$ nm, $q_2 = $ -1e), and the size and charge of ice particle is varied. The collision geometry is shown in Figure 3a.

ice particle	Coulomb barrier, E_{Coul}, meV	$v_{\text{rel}}^{\min}$, ms^{-1}	$v_{\text{rel}}^{\max}$, ms^{-1}	aggregation, %
$r_1 = 30$ nm; $q_1 = 0$	0	0	1341	100
$r_1 = 30$ nm; $q_1 = $ -1e	23.7	252	1311	29.9
$r_1 = 30$ nm; $q_1 = $ -2e	55.3	384	1340	3.57
$r_1 = 20$ nm; $q_1 = 0$	0	0	1481	100
$r_1 = 20$ nm; $q_1 = $ -1e	35.7	309	1425	13.7
$r_1 = 20$ nm; $q_1 = $ -2e	82.9	470	1465	0.50
$r_1 = 10$ nm; $q_1 = 0$	0	0	1776	100
$r_1 = 10$ nm; $q_1 = $ -1e	71.3	436	1607	1.15
$r_1 = 10$ nm; $q_1 = $ -2e	165.9	665	1676	0